![University of Glasgow logo]

Yambangyang, Pracha (2020) *Nonlinear ultrasonic wave mixing for the non-destructive evaluation of materials' properties.* PhD thesis.

http://theses.gla.ac.uk/81510/

Nonlinear Ultrasonic Wave Mixing for the Non-destructive Evaluation of Materials' Properties

Pracha Yambangyang

**Submitted in fulfilment of the requirement for
The Degree of Doctor of Philosophy**

**School of Engineering
College of Science and Engineering
University of Glasgow
2020**

Abstract

Nonlinear ultrasonic wave mixing has been shown to be a powerful method to detect and characterise damage or defects in materials. This technique has been used in a wide range of applications such as the non-destructive evaluation of material properties due to its higher sensitivity when compared to conventional, linear, ultrasonic techniques. This technique is based on an investigation of nonlinear behaviours in a material by using harmonic generation or nonlinear resonance, which are able to detect small scale defects or structural degradation, such as cracks, micro cracks, and material characterisation in the wider sense. Within the context of medicine, the detection of deep tissue injury, such as a pressure ulcer, could benefit from the capabilities of nonlinear ultrasonic wave mixing methods. These wounds are currently detected late, leading to difficult treatments. Earlier detection over smaller areas based on difference, in properties relative to neighboring tissue, means nonlinear ultrasound techniques could have a significant impact on patient recovery.

The purpose of this thesis is to develop a platform which can detect nonlinearities of materials using nonlinear ultrasonic wave mixing techniques. In this study, two kinds of non-linear wave mixing techniques are introduced for the detection of small particles distributed in a hydrogel phantom, a proxy for an injury area in the early stages of the development of a wound. Wave mixing was also applied to measure an accumulated change to material properties also known as physical aging. The results demonstrated an improved ability of non-linear wave mixing method over linear techniques to distinguish minuscule particles and to be able to monitor a slow rate of change in material properties, which would be used to monitor deep wounds under the skin such as pressure ulcers.

The results clearly show that the summed frequency of a nonlinear wave signal can detect a range of microparticle sizes ($70\mu m$, $100\mu m$ and $150\mu m$) with higher sensitivity and resolution as compared to the linear echo ultrasound. This is a factor of more than 10 increase in the resolution of defect detection as compared to linear methods, allowing for earlier wound identification.

In addition, the response of the nonlinear summed frequency interaction was captured with a 30 s sampling rate at 6.25 MHz. This system showed that the nonlinear ultrasonic technique was suitable to detect the physical aging of amorphous polymers at the annealing temperature. When the polymer structure underwent structural relaxation, the nonlinear wave mixing energy gradually increased due to the non-equilibrium state and then continually developed due to physical aging. The system is not only designed to detect the nonlinearities of soft material properties using nonlinear ultrasonic techniques, but also to enable its application to evaluate the accumulated change of material properties.

These experimental results suggest that nonlinear ultrasonic wave mixing technique may be useful for detecting small scale (early onset of) pressure ulcers developing deep in the skin. The ability to observe physical aging in polymers, and the analogous behaviour of polymer physical aging and ulcer development, suggest it may be possible to monitor pressure ulcer development with nonlinear techniques.

Table of Contents

List of Tables

List of Figures

List of Accompanying Material

Conference

International Conference on Nonlinear Elasticity in Materials June 24-28, 2019 Krakow, Poland; Oral presentation.

Acknowledgement

True success is not in the learning but in its application

to the benefit of mankind

His Royal Highness Prince Mahidol of Songkla

Author's Declaration

I declare that, except where explicit reference is made to the contribution of others, that this dissertation is the result of my own work and has not been submitted for any other degree at the University of Glasgow or any other institution.

Abbreviations

AAc	Acrylic acid
APS	Ammonium persulfate
ASTM	American society for testing and materials
GPIB	General purpose interface bus
MBAm	N,N'methylenebisacrylamide
NDE	Non-destructive evaluation
NIPAM	N-isopropylacrylamide
PAG	Polyacrylamide hydrogel
PUs	Pressure ulcers
P-wave	Longitudinal wave
PVA	Polyvinylacetate
PVCP	Polyvinyl chloride plastisol
PVC	Polyvinyl chloride
PMMA	Polymethylmethacrylate
S-wave	Transverse wave

Chapter 1   Introduction

1.1 Pressure Ulcers

Pressure ulcers (PUs) are an injury frequently occurring in the elderly. Elderly people who have a spinal cord injury or limited ability to move are at risk of developing PUs. PUs occur on a patient's skin when it is compressed between bone and soft tissue. The areas where PUs are generally found are the sacrum, the greater trochanter, the ischium, the heel and the lateral malleolus (Mak, Zhang and Tam, 2010). PUs are chronic wounds, affecting about 412,000 people developing a new pressure ulcer in the UK each year. In addition, the UK spends approximately £1.4bn - £2.1bn per year for PU treatment (Bennett, Dealey and Posnett, 2004). Thus, many researchers have been developing an approach to prevent and detect them early (Goldman and Salcido, 2002; Schelkanova *et al.*, 2015; Zhang, Osborn and Kalra, 2016; Kmiecik, Skotny and Detyna, 2017). Many of the techniques are commonly used in hospitals with limited staffing, under the control of a physician or a nurse. The evaluation and prevention of PUs are highly dependent on the expertise of health-care personnel (Ophir *et al.*, 1991; Tsuji *et al.*, 2005; Lienhard, 2010; Madsen *et al.*, 2018). The classical prevention of PUs is that patients have to be manually turned nearly every hour in order to reduce pressure and high-risk areas (Swisher *et al.*, 2015). While a variety of devices are used for monitoring PUs in the early stages, it would be better if a device with high sensitivity could alert nursing staff when a threshold of tissue stiffness is exceeded (Gefen *et al.*, 2005).

1.1.1 Conventional devices of PUs evaluation

Numerous medical electronic devices have been used for the evaluation of PUs. The parameters that have been considered for evaluating PUs are blood perfusion, tissue impedance, surface interface pressure, and tissue stiffness.

Blood perfusion: The skin blood flow is a basic function to sustain the normal structure and function of the skin. The shift of blood flow is associated with decreased blood perfusion which can be directly measured by laser Doppler flowmetry and laser Doppler perfusion. These devices are based on the Doppler effect where a light pulse is sent to detect the movement of blood. The reflected signal from stationary tissue is the same as the incident signal while for moving blood, there are small differences in the frequency of the reflected signal. The scattered signal also depends on tissue properties such as density of tissue, skin

pigment and oxygenation such that the reflected signals are related to these properties as well. This technique is commonly used because it is a non-invasive and simple method. The measurement does not require injection, only transmitting and receiving transducers. Oscillations in blood flow in soft tissue can be used to monitor the risk of pressure ulcers (Jan *et al.*, 2011; Liao Burns and Jan, 2013). The technique of measuring skin blood perfusion has several advantages, including providing a non-invasive method to diagnose stages in the development of PUs based on microvascular function. However, one can see disadvantages in the fact that the altered blood flow will affect the evaluation and that the depth and volume of measurement is limited (Manorama *et al.*, 2010; Fredriksson, Larsson and Strömberg, 2009).

Bioimpedance: Cells and tissues are complex structures contraining intracellular and extracellular fluids with specific frequency response to electrical stimulation. The fluid in cells and cell membranes can be represented by resistance and capacitance. These resistances and capacitances of the cell combine to give the electrical impedance of the tissue. Therefore, the frequency response of the electrical impedance of the tissue is strongly correlated to changing physiological properties and chemical status. Electrical impedance devices have been developed based on the fact that impedance is strongly associated with tissue health. The main advantage is that it uses a non-invasive technique providing a flexible electrode device (two or four electrodes) to detect tissue damage or PUs in real time and is an uncomplicated measurement on the skin surface area: two measuring electrodes and injecting current electrodes are placed over the wound with a coupling hydrogel layer on electrodes. Ulcer detection is improved when the detected impedance is compared to the normal value of a patient's skin (Swisher *et al.*, 2015).

Interface pressure: Surface pressure promoting PUs on the skin is developed inward into the bone. The force is generally the result of friction between the skin and clothing or bed sheet, leading to damage on the skin. Moreover, the result can lead to a deep tissue injury under sustained loading conditions (Chan *et al.*, 2015). In order to measure the distributed surface pressure, various kinds of pressure sensors (capacitive, piezoresistive, electro-pneumatic) are used in an array on a seat or a mattress for detecting pressure, called a pressure-mapping system (Swain and Bader, 2002). They have the ability to localise the loading point and identify loading conditions in various postures. Another advantage of measuring interface pressure is the imaging of pressure distribution on the surface or cushion. However, this measurement has some limitations because it cannot access multi-axial forces which could mean that the pressure sensor array can only detect those forces occurring between loading and surfaces. These forces can only present contact stresses

without other shear stresses. The shear forces on the skin are known to develop and have been found to be clinically significant (Ferguson-Pell, 2005).

Tissue stiffness: According to recent research, sustained pressure between tissue and bone can develop either on the stresses on skin surface or within deep tissues. These stresses, especially within the tissue, have been reported to have values three to five times higher internally near a bony prominence than the pressure applied on the skin (Deprez *et al.*, 2011). This pressure could deepen pressure ulcers in the tissue (Orsted, Ohura and Harding, 2010). Therefore, deep ulcers are very difficult to identify. However, Gefen *et al.,* 2005 have shown that those kinds of ulcers can be characterised by stiffness and as a result, ultrasound elastography is used for detection. Their potential could be targeted to an ulcer area and used for diagnosis of the growth process. Because of that capability, various kinds of ultrasound-based elastography techniques, such as static-elastography (Kallel *et al.*, 1998; Konofagou and Ophir, 1998), sono-elastography (Lerner, Huang and Parker, 1990a; Parker, Doyley and Rubens, 2010), shear wave-induced resonance elastography (Hadj Henni *et al.*, 2012) vibro-acoustography (Fatemi and Greenleaf, 1998; Urban *et al.*, 2011), and harmonic motion imaging (Konofagou and Vappou, 2012), have been applied for the characterisation of soft tissue pressure ulcers. Ultrasound-based elastography devices are noninvasive, safe and portable.

1.1.2 Pathophysiology of PUs

The skin is an organ that protects the human body and controls body temperature. It can be separated into two layers, the epidermis and the dermis. The epidermis is the top layer of the skin with a thickness about 60 µm to 100 µm (Liao, Burns and Jan, 2013). The other layer is called the dermis, the thickest layer, which can be subdivided into two layers: the papillary layer and the reticular layer. The dermis is about 1 mm to 4 mm thicker than the epidermis. The dermis layer has a rich blood vessel supply, while the epidermis layer lacks blood supply. The vessels which are in the dermis layer provide nutrition, oxygenation and thermoregulation and consist of three parts: superficial vascular plexus, deep vascular plexus, and subcutaneous vascular plexus (Liao, Burns and Jan, 2013). PUs are classified by National PU Advisory Panel (NPUAP) as standard stages shown in Figure 1-1. There are four stages, which are skin redness, partial loss, full thickness skin loss and full thickness tissue loss (Schelkanova et al., 2015). However, the degree of severity of PU development depends on many factors, such as pressure, shear force, time, temperature, humidity, and other facors affecting interactions between the skin and the surface (Swain, 2005).

1.1.3 Shear and friction contribute to PUs development

Shear and friction play an important role in PU development. In combination with pressure (due to an external force) they can lead to damage in the underlying soft tissues, especially over a bony prominence (Orsted, Ohura and Harding, 2010). Shear stress is generated when a force is applied in a parallel direction to the surface of an object while the top of the object stays stationary. Shear stress causes object deformation, quantified by shear stain. In addition, friction is a force which resists the movement of two objects that are touching. The friction contributes to shear stresses on the surface to hold the skin in place against the support surface while the rest of the patient's body moves (Reger *et al.*, 2010). These forces contribute to act on the body's surface with forces to generate the damage and ischemia of the skin and deeper tissues, leading to the development of pressure ulcers.

The mechanisms of PU development depend on important factors including of prolonged pressure, shear stress, and blood circulation. Schelkanova *el. al.,* (2015) summarizes that there are three mechanisms of PU improvement. The first mechanism is tissue damage, caused by extended pressure in areas which impair capillary perfusion and which then develop hypoxic tissue. The degree of tissue damage is dependent upon how much the pressure becomes nonuniform, and the pressure gradient developed in the nearby layers of the tissue. The second mechanism of PU development results from shear stress on the skin. Shear stress is an important factor that accelerates the development of pressure ulcers that result from the greater mechanical force on the areas.
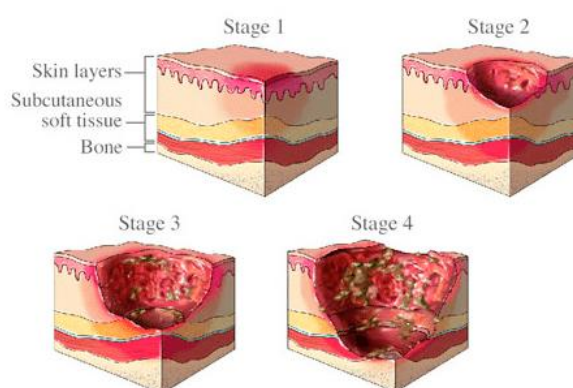
Figure 1-1: First stage of PUs appears red with lighter skin color. The site may be tender painful and warm. Then the outer layer of skin is damaged or lost. The damage may extend beyond to a deep wound in stages three and four. Source: http://www.discovermymobility.com

The shear forces on soft tissue occur when forces are applied in different direction to the same tissue area. The frictional force which is on the skin interface resists the movement of the body and the shear force at the rest of the tissue area distorts blood vessels which run

through the skin and the skeleton. The third mechanism involves blood circulation between the extracellular interstitium and terminal capillaries. An external force applied to the tissue results in changing interstitial pressure, interstitial fluid flow and concentration of molecules as well as damage to the transport of nutrients and waste product systems. This mechanism results in metabolic nonequilibrium in tissue that leads to tissue necrosis.

According to the mechanism of PU development, friction and shear stresses can lead to superficial and deep Pus of skin. Superficial PUs are common on the skin surface and are caused by friction and shear stresses, whereas deep pressure ulcers (deep tissue injuries), which occur near bony prominences, are generated by tissue compression near bone. These compressions result in local occlusion in blood circulation supply which later develops into ischemic conditions that may result in cell death. Such PUs cannot be identified or observed by the evaluation of the skin, which may lead to more serious damage before detection. Deep muscle injury was studied in an animal model in which the force was applied to skin, resulting in cell death in muscle tissue. The study has revealed that loading 64 kPa on a pig's skin for 4 hours caused muscle cell death and if it reached 107 kPa, skin injury may develop in 8 hours. Moreover, the highly curved bone surfaces caused concentrated loads and mechanical stresses on muscle tissues which lead to pathologic changes related with ischemia (Gefen *et al.*, 2005). The consequence of ischemia and deformation in deep muscle injury was also studied in rats using a 6.3 Tesla magnetic resonance image (MRI) with T2 weighted technique – T2 is transverse relaxation time used for tissue characterisation in MRI imaging. An external pressure of 150 kPa was applied to a rat tibialis, resulting in necrosis to simulate PUs on the rat's skin. These results clearly showed an increase in the tissue stiffness of the skin and an increase in maximum shear strain (Mak, Zhang and Tam, 2010). Moreover, tissue death caused by the ischemic condition can induce surrounding tissue properties to change from their normal values. Young's modulus and Poisson's ratio are evaluated to determine the behavior of tissue under compression stress. Results have shown that the PU region has high stiffness, with a ratio of about 1.8 to normal tissue (Deprez *et al.*, 2011).

Although conventional ultrasound used for medical imaging can investigate PUs at local area, their capacity to do so is at a relatively high-pressure point. Gefen *et al.*, 2005 has demonstrated that the ischemia where tissue connects with interface pressure from the skin is a main reason for tissue breakdown. This breakdown point was detected at a pressure of 35 kPa (about 260 mmHg) and maintained about 60 minutes, resulting in a two-fold stiffening
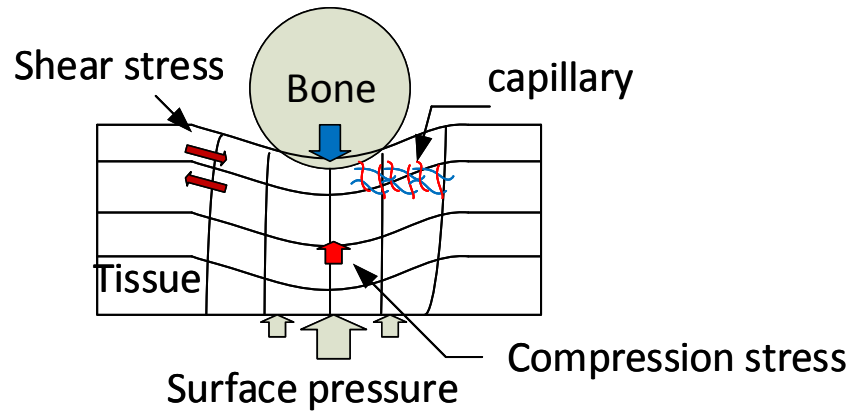
Figure 1-2: When a gravity generates a force pulling a patient on to the surface, the opposing force produced by the surface can be divided into two components: a perpendicular component which results in pressure and a tangential component which results in shear stress. The shear stress and pressure which act on bony prominence produce the damage and ischemia of tissue.

of tissue with cell death. An *in vivo* study applied 35 kPa of pressure on the thigh of an animal. A commercial ultrasound 35 MHz probe measured the tissue stiffness to detect deformations of the tissue. Significant differences in tissue stiffness were observed near the area where bone is cover by muscle layers (Deprez *et al.*, 2011). However, Deprez *et al.,* (2011) suggested that the value of 4.3 kPa is the pressure threshold making capillary collapse. If those pressures are maintained, interface pressures higher than the mentioned value are supposed to lead to tissue damage.

Therefore, it would lower the risk for tissue death if a sensory device can clearly highlight when the threshold pressure has been exceeded for 15 minutes, the time to possibly prevent PUs in tissue and prevent compression leading to high tissue stiffness of greater than 1.8 times the normal tissue value (Gefen *et al.*, 2005). So the devices with capability to measure the changes in mechanical properties of tissue for the evaluation of pressure ulcers based on those time and pressue threshold could be beneficial for early detection in terms of their high sensitivity.

1.2 Nonlinear ultrasonic methods

Nonlinear ultrasonic techniques are powerful ultrasound detection methods with ability to detect and characterise damage or defects in materials. These techniques have been used in industry for nondestructive evaluation (NDE), such as crack and micro-crack (Jingpin Jiao *et al.*, 2014, Li *et al.*, 2016) and fatigue (Jiao *et al.*, 2017). An advantage of the nonlinear ultrasonic technique is high sensitivity for evaluation of the smaller cracks or structural degradation than the conventional ultrasound technique (Li *et al.*, 2016). This

technique is based on an investigation of nonlinear behavior in the material using a harmonic generation or nonlinear resonance which can possibly detect micro-defects (Jiao *et al.*, 2017).

1.2.1 Nonlinear wave mixing

The nonlinear wave mixing method is an ultrasonic detection technique based on two incident waves interacting at a specific angle. Figure 1-3 is a schematic diagram of nonlinear wave mixing. It consists of two transducers generating two different frequencies sent to a specimen where their interaction occurs. At the interaction point, the resonant wave is produced if the resonance conditions are satisfied. This resonant wave which can be measured by a receiving transducer is related to nonlinearity the material's. The advantage of nonlinear wave mixing is that it has not only high sensitivity for detection but also more flexibility for choosing the wave mode combination, operating frequencies and propagating directions (Zaitsev *et al.*, 2006, Korneev and Demčenko, 2014). However, in order to implement this approach, the practical implementation of nonlinear wave mixing requires transmitting and receiving transducers which have a precise arrangement in the laboratory.
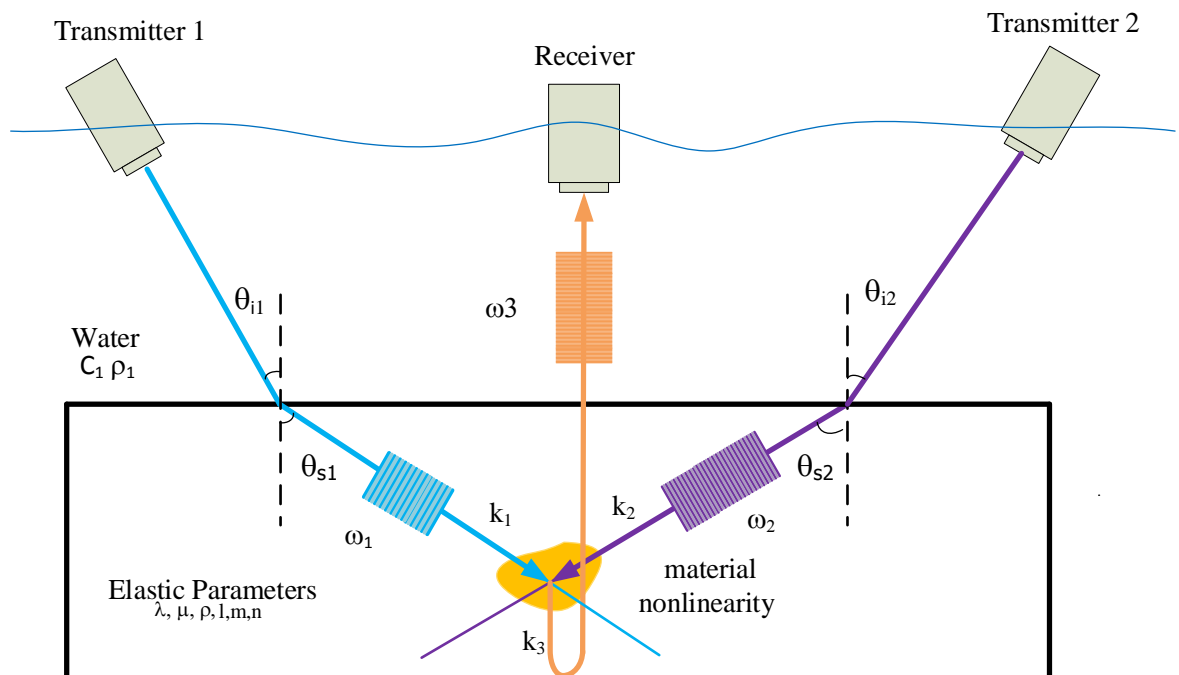
Figure 1-3 shows schematic of nonlinear ultrasonic wave mixing system. A typical system consists of two transmitted ultrasonic transducers and a receiving ultrasonic transducer all of which are installed on accurate rotation states (360° coarse, 5° fine). Experiments are undertaken with a piece of specimen immersed in water chamber without a bubble. Inclination angles θ_1 and θ_2 and distance from specimen to transducers are the geometrical parameters calculated by using Snell's law. ω_1, ω_2 are the frequencies of the excited waves generated by transducer 1 and 2 and k_1 and k_2 are the initial wave vectors, k_3 is the resonance wave vector where $ki = \omega_i / C_i$. C_i is the phase velocity of the related wave, and i = 1, 2, 3.

1.2.2 Nonlinear modulation technique

The nonlinear modulation method is based on nonlinear wave theory in which an input signal combines with two different frequencies. The basic principle is illustrated in Figure 1-4. The two sinusoidal signals with a fundamental frequency are applied to the same transmitter (Courtney *et al.*, 2008). Then two frequencies passing through a transducer must generate harmonic waves (2rd, 3th or 4th harmonic frequency) which result from the sum and difference of those two fundamental frequencies. When these incident waves have interacted with nonlinearities of a sample (described in term of B/A), the response of nonlinear signal appears in terms of the sum and difference of the excited frequency (Donskoy, Sutin and Ekimov, 2001). The vibro-acoustic modulation method is a nonlinear modulation technique first introduced in the 1990s, and its principle is usually based on an association between the degradation and nonlinear ultrasonic parameters (Li *et al.*, 2016). A sidelobe amplitude method (Donskoy *et al.,* 2001), modulation index method (Courtney *et al.*, 2008), damage index method and bispectrum analysis (Courtney *et al.*, 2010) are examples of those techniques using a modulation method for acquiring quantitative characterization of micro-damage. Courtney *et al.* has illustrated the factors affecting the ultrasonic intermodulation crack detection technique. These results indicate that the defect of fatigue cracks causes increased nonlinearity, which can be obtained and analysed by bispectral signal processing techniques. Typically, the data are analysed by power spectral analysis based on magnitude of spectral signal, however, sometimes, some cases not only need magnitude spectral analysis buy also require the content of phase spectrum. The bispectral analysis provides information on relationships between magnitude of frequencies and phase components of signals. Straka *et al.* have shown signal magnitude of intermodulation resulting from the number of the fatigue cycles and suggested that the intermodulation technique may possibly be used for the evaluation of fatigue damage. Duffour *et al.* have developed a detection technique probing an amplitude modulation of an ultrasonic vibration field called vibro-acoustic modulation. When a mechanical vibrated signal propagates through a cracked specimen, the low-frequency structural vibration is added to that propagation as result to generate the sum and different of excited signals. These are used to evaluate the level of damage. Donskoy *et al.* have also proposed vibro-modulation and impact-modulation methods for NDE and detection of a fatigued specimen. Their measurement system combined between a pair of 20 kHz driving transducer and other impact vibration (5-30 Hz) generated by a hammer. Their results showed a high sensitivity to detect a crack in steel pipes.

In the medical diagnostics of ultrasound, the nonlinear phenomena of tissue provides the possibility to improve accuracy with more precise information on the state of the tissue. Their advantages have been proposed in medical imaging (Ichida *et al.,* 1987, Kim *et al* 1990). Law *et at.,* have determined the nonlinearity parameter (B/A) of various biological solutions and soft tissues using the thermodynamic and finite amplitude methods. The B/A parameter of tissue is correlated to the second harmonic response from tissue determined by a receiving transducer. The nonlinearity factor B/A is also depended on thermodynamic variation thus the B/A values are determined the change of sound velocity with temperature and pressure as expressed in next Chapter. Those values may be beneficial for differentiating normal and abnormal biological tissue such as fat, liver, muscle brain and heart muscle, which have advantage for the disease diagnosis and therapeutic application. In order to estimate the variation of nonlinear values of tissue, which may relate to pathologic changes of tissue, the nonlinear characteristics of tissue should be studied.
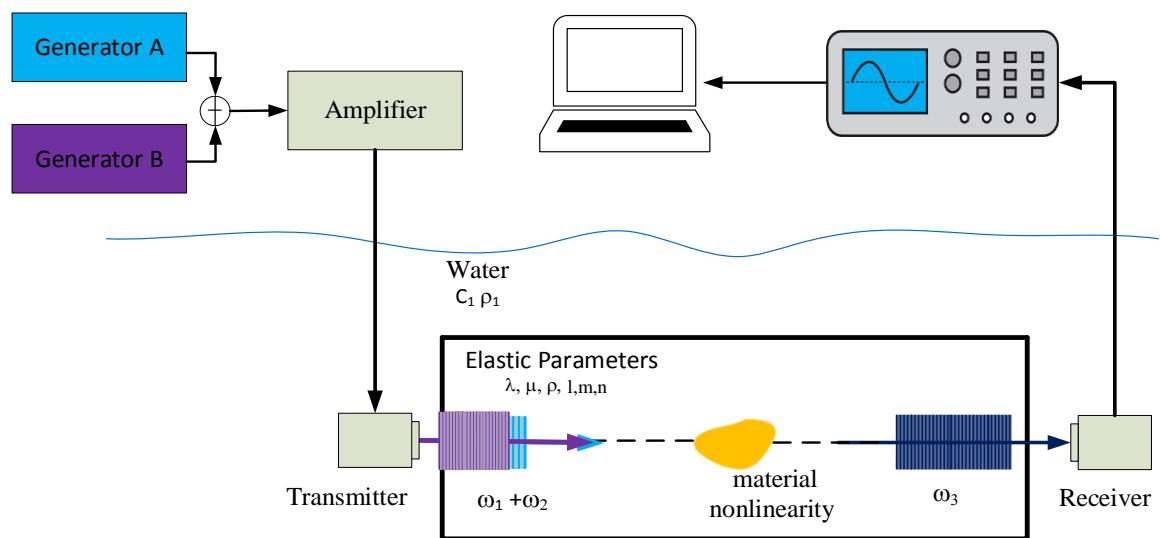
Figure 1-4 shows a schematic diagram of a nonlinear modulation technique. The system consists of two signal generators producing two sinusoidal signals. Their signals are summed and amplified before passing to a transmitter immersed immerging in water. ω_1, ω_2 are the frequencies of the excited waves generated by generator A and B. A resonant wave might be generated by two incident waves , ω_3, which are passed to a receiver, then recorded and processed by an oscilloscope and PC, respectively

1.3 Aims and objectives

A variety of linear methods have been proposed for PU detection but the techniques for evaluation and prevention of PUs is still restricted. These techniques mainly focus on the measurement of changing tissue properties of the skin. The breakdown of skin tissue is avoided by detecting tissue stiffness and loading time to identify where the tissue is at risk to PU development as described in section (1.1.3). In addition, a sustained compression load

can lead to deep tissue damage, subsequent tissue breakdown and eventually PUs. This area of high stress fields is investigated for PU localization at regions of interest in (Mak, Zhang and Tam, 2010; Luboz *et al.*, 2014; Schäfer *et al.*, 2015). If these high stress fields can be detected early in a very small area, it would allow for the detection and prevention of PUs in early stages of formation and could provide a method to monitor PU development as well.

The purpose of this study is to develop a platform which can detect nonlinearities of materials using nonlinear ultrasonic techniques. The system is not only designed to detect the nonlinearities of soft material properties using nonlinear ultrasonic techniques, but also to enable the application to evaluate PUs for a small area at the early stages and the accumulation of changing material properties with time. The purposes of the study are to:

1.3.1   Study the nonlinearity parameters using nonlinear ultrasonic techniques.

1.3.2   Evaluate the energy of nonlinear wave from solid materials using nonlinear ultrasonic wave-mixing methods.

1.3.3   Evaluate the energy of nonlinear wave on tissue-mimicking phantoms using nonlinear ultrasonic modulation methods.

1.3.4   To utilise the nonlinear ultrasonic measurement for study a particle deflect simulating the PUs area.

1.3.5   To utilise the nonlinear ultrasonic method for evaluating mechanical material properties.

Chapter 2   Background Theory

2.1 Introduction

In this chapter, the theoretical concepts of nonlinear ultrasonic wave mixing techniques are described. The chapter is divided into three sections; the first section briefly describes the elastic wave with wave equation propagating in media and Snell's law which is used for evaluation of reflecting wave coefficients. The second section covers the basics of nonlinear ultrasonic techniques divided into the nonlinear ultrasonic wave mixing technique and the nonlinear ultrasonic wave modulation technique, different platforms with specific applications and measurements implemented in this thesis. The final section includes how to prepare tissue mimics or tissue phantoms which represent tissue with properties of the skin or organ. This chapter introduces background information on nonlinear ultrasonic techniques and their use in detecting and characterising damage in phantoms.

2.2 Elasticity

2.2.1 The principle of linear elasticity

Elasticity is an important physical property of a material which can be described as an ability for restoring its shape and volume when an external force is applied. The concept of the constitutive equation is normally derived from the linear theory of elasticity (Hooke's Law). This relationship describes the response of a uniaxial material to an applied force in one direction. The response is characterised by the corresponding strain (ε) and stress (σ)

$$\varepsilon = \frac{\delta}{L} \tag{2.1}$$

$$\sigma = E \times \varepsilon \tag{2.2}$$

where E is Young's Modulus (a material constant) δ is the deformation and L is the original length. When hydrostatic pressure is applied to a material body, it produces an equal stress in every direction, leading to the deformation of its body or the change in the volume, characterised by the material's bulk modulus (K), which describes the ability of a material or substance to resist compression. A shear modulus (G) can be used to describe the relationship between shear strain and shear stress. It can be expressed in term of Young's modulus and Poisson's ratio (v) as well as the bulk modulus,

$$K = \frac{E}{3(1 - 2v)} \tag{2.3}$$

$$G = \frac{E}{2(1 + v)} \tag{2.4}$$

Young's modulus and Poisson's ratio are also correlated to two parameters which are described by Gabriel Lamè, λ and μ are the first and the second Lamè parameters providing an equivalent description of the elastic modulus and shear modulus respectively (Glozman and Azhari, 2010),

$$\lambda = \frac{Ev}{(1 + v)(1 - 2v)} \tag{2.5}$$

$$\mu = \frac{E}{2(1 + v)} \tag{2.6}$$

2.2.2 Elasticity of soft tissue

The elasticity of tissue is a relationship between stress and strain when external forces are applied to a body. The restoring forces in the tissue are responsible for deformation (shape change). Their response can be used to characterize the tissue and identify a pathophysiological disease of tissues such as coronary vessels, breast, kidney, liver, muscle and skin (Glozman and Azhari, 2010). The elasticity of tissue is important in imaging. Developments in elasticity imaging have improved the quality of the images by applying external low frequency (100 - 300Hz) stimulus to induce oscillation within soft tissue. The motion is subsequently measured by the Doppler instrument at 7.5MHz (Lerner, Huang and Parker, 1990). The motion and strain inside the tissue are evaluated to differentiate the tissue elasticity, and can also be applied to tissue imaging (Yamashita and Kubota, 1995, 1996). Based on the externally applied vibration method, a vibrator is combined with a detecting transducer in one probe in order to improve and construct an image of Young's modulus (Sandrin *et al.*, 2002). Recently, elasticity of tissue has been used to characterise biological tissue because many diseases contribute to the change in the local elasticity (Glozman and Azhari, 2010). The estimation of tissue elasticity is used in clinical research for the evaluation of hepatic diseases, the stiffness of tissue surrounding arterial vessels, and properties of breast tissue (Umemoto *et al.*, 2014). Numerous techniques have been developed to evaluate tissue stiffness. These techniques basically estimate static or harmonic motion by applying an external or internal mechanical stimulus whereby their measurements deal with the estimation of the small displacement and strain in tissue resulting from an external excitation (Konofagou and Hynynen, 2003). A variety of methods using different

stimuli such as static load, external vibrators and acoustic radiation force are used to deform soft tissue. In general, linear elastic methods have limited applicability. For example they are unable to differentiate between normal and tumor tissue in the breast because of their similar elastic moduli (Wellman *et al.*, 1999). To solve this, an alternative approach of interest is the use of nonlinear methods to estimate material properties directly (Mihai and Goriely, 2017).

2.2.3 Nonlinear elastic tissue

Normally, elastic tissue is linear if the stimulated force is proportional to the resulting displacement. The deformation of a homogeneous isotropic linear elastic material is characterized by Young's modulus and the Poisson ratio. However, under large stimuli, their properties and responses are fundamentally nonlinear so that these mechanical responses cannot be represented by the usual two constants. In general, the nonlinear elastic response of tissue is defined by parameters representing the function of the deformation of tissue. These expressions describe the wave propagation of a finite-amplitude plane wave (Zheng, Maev and Solodov, 2000)

$$V = c_0(1 + \beta_2 M) \tag{2.7}$$

where c_0 is the velocity of sound, $M = u/c_0$ is the acoustic Mach number, u is the particle velocity, and β_2 is the coefficient of the second-order acoustic nonlinearity. The equation shows that propagation speed, V, distorts during travel by a rate β_2. Additionally, the expression for β_2 depends on the pressure and density temperature (Bjørnø, 2010). Beyer, (1960) has also explained nonlinearity as the relation between pressure and density, expanded via Taylor's theorem. His expansion shows two derivative terms, one with respect to acoustic pressure and a second with respect to temperature defined by constants A and B. The relationship is given in Equation (2.8).

$$\frac{B}{A} = 2\rho_0 c_0 \left(\frac{\partial c}{\partial P}\right)_T + \frac{2c_0 T\mu}{C_P} \left(\frac{\partial c}{\partial T}\right)_P \tag{2.8}$$

The ratio of B/A is the wave-form distortion which can be used as an alternative to the β_2 nonlinear parameter. Here ρ_0 is density, C_P is the specific heat at constant pressure, T is the absolute temperature, amd μ is the volume coefficient of thermal expansion. The B/A value has been suggested for the characterisation of biological tissue because of their structural

variation resulting from pathological condition (Law, Frizzell and Dunn, 1985). Moreover, values of B/A for biological materials have been published by various researchers, as summarized in (Bjørnø, 1986).

2.3 Propagation of Elastic Wave in Media

Elasticity characterises a material's ability to restore its shape and volume when an external force is applied. The internal deformations involve the relationship between stress and strain in a given medium. Therefore the medium is called an elastic medium and the mechanical disturbances in an elastic medium are referred to as elastic waves. The elastic vibration and acoustic wave are used widely in ultrasonic applications such as ultrasonic imaging, ultrasonic non-destructive testing and especially in ultrasonic properties characterisation. Elastic vibrations and waves, therefore, are very important for evaluation processes of propagation in the medium. The media in this study is the tissue which can be assumed to be solid.

2.3.1 Wave Equation for a solid media

The wave propagating in a solid can be derived from Newton's second law of motion. By considering a solid as a finite cubic volume, an element volume *dx dy dz*, the difference of force applied to its opposite face is equal to the product of mass and acceleration which can be expressed in terms of stress σ and displacement *u*, whereas ρ is the density of the media.

$$\rho \frac{\partial^2 u_x}{\partial t^2} = \frac{\partial \sigma_{xx}}{\partial x} + \frac{\partial \sigma_{xy}}{\partial y} + \frac{\partial \sigma_{xz}}{\partial z} \tag{2.9}$$

By analogy, Equation (2.9) can be written for axes *y* and *z*. The stresses in the above equation can be calculated by using the Lame′ constant for stress-strain. Then the equation of wave propagation in an elastic medium can be written as follows

$$\rho \frac{\partial^2 u_x}{\partial t^2} - (\lambda + \mu) \frac{\partial \Delta}{\partial x} + \mu \nabla^2 u_x = 0 \tag{2.10}$$

Where $\nabla^2 = \frac{\partial^2}{\partial x^2} + \frac{\partial^2}{\partial y^2} + \frac{\partial^2}{\partial z^2}$ is the Laplace operator, the dilatation Δ is defined as $\Delta = \frac{\partial u_x}{\partial x} + \frac{\partial u_y}{\partial y} + \frac{\partial u_z}{\partial z}$ and determines their changed volume as the wave propagates. However, for tissue the value of Δ is typically small because they are found to be approximately incompressible.

2.3.2 Refraction, Reflection and Transmission

When an ultrasonic wave strikes a boundary of media, a possible interaction of refraction and transmission of the incident wave at the interface occurs. Generally, that interaction depends on the combinations of solid, fluid and vacuum of the two media. In this thesis, we consider the combination of water and solid as shown in Figure 2-1. Then an incident wave can generate longitudinal wave (P_wave) and transverse wave (S_wave), so we need to consider the phenomena of refraction and reflection. Here we calculate the geometry configuration of wave mixing where an ultrasonic wave interacts with water and solid material boundaries such as PVC, aluminum and tissue phantom. An incident longitudinal wave at the water-solid boundary (Figure 2-1) results in a reflected and transmitted longitudinal wave (P-wave) and a reflected and transmitted shear wave (S-wave). Thus, there is a mode conversion between P- and S-waves for angles different from zero degree incidences. Their reflected angles are related by Snell's law as follows:

$$\frac{\sin \theta_{pi}}{c_{p1}} = \frac{\sin \theta_{pr}}{c_{p1}} = \frac{\sin \theta_{pt}}{c_{p2}} = \frac{\sin \theta_{sr}}{c_{s1}} = \frac{\sin \theta_{st}}{c_{s2}} \qquad (2.11)$$

where the first index represents the mode conversion and the second index of the wave velocities indicates medium 1 or medium 2. θ is the angle of wave interaction where the first subscript p stand for longitudinal wave, s stand for shear wave and second subscript i, r and t indicate the incident, reflected and transmited angle, respectively. $c_{p1}, c_{p2}, c_{s1}, c_{s2}$ are the velocities of longitudinal and shear wave in its respective medium. Based on Snell's law, we consider the interaction of our experiment which consists of two mediums, water and solid as shown in Figure 2-1. When an ultrasonic wave propagates to the water and then interacts with a solid medium, the interaction response can be calculated by applying Snell's law. When θ_i, θ_r are the incidence and reflected angle of the longitudinal wave in the water, θ_p, θ_s are the angle of refracted longitudinal and shear wave in solid respectively, and I_p, R_p, T_{pp}, T_{ps} are the intensity coefficients of the incident, reflected, transmitted longitudinal wave and transmitted shear wave. Those coefficients can be calculated by using equation (2.12).
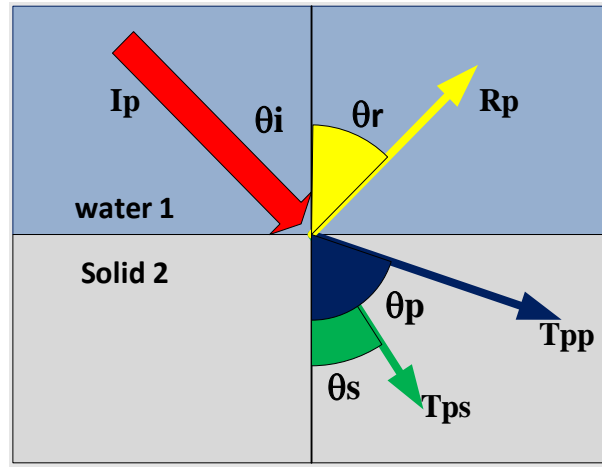
Figure 2-1: a combination of water and solid can generate longitudinal and shear wave.

$$
\begin{bmatrix}
a_{11} & a_{12} & a_{13} & a_{14} \\
a_{21} & a_{22} & a_{23} & a_{24} \\
a_{31} & a_{32} & a_{33} & a_{34} \\
a_{41} & a_{42} & a_{43} & a_{44}
\end{bmatrix}
\begin{bmatrix}
Rp \\ Tp \\ Rs \\ Ts
\end{bmatrix}
=
\begin{bmatrix}
b_1 \\ b_2 \\ b_3 \\ b_4
\end{bmatrix}
or
\begin{bmatrix}
c_1 \\ c_2 \\ c_3 \\ c_4
\end{bmatrix}
\tag{2.12}
$$

Equation (2.12) can be rewritten depending on whether longitudinal or shear wave incidence is considered. The components of the matrix a_{ij}, b_i, c_i have been shown by Ediguer *et al.* 2006 expressed by equation (2.13, 2.14).

$$
\begin{bmatrix}
-\cos\theta_{p1} & -\cos\theta_{p2} & \sin\theta_{s1} & \sin\theta_{s2} \\
-\sin\theta_{p1} & \sin\theta_{p2} & -\cos\theta_{s1} & \cos\theta_{s2} \\
-Z_{p1}\cos2\theta_{s1} & Z_{p2}\cos2\theta_{s2} & Z_{s1}\sin2\theta_{s1} & Z_{s1}\sin2\theta_{s2} \\
-Z_{s1}\dfrac{C_{s1}}{C_{p1}}\sin2\theta_{p1} & -Z_{s2}\dfrac{Cs2}{Cp2}\sin2\theta_{p2} & -Z_{s1}\cos2\theta_{s1} & -Z_{s1}\cos2\theta_{s2}
\end{bmatrix}
= a_{ij}
\tag{2.13}
$$

Then reflection and transmission coefficients of longitudinal and shear incidence wave can be evaluated by applying the Cramer's rule depending on whether longitudinal or shear incidence is used (Franco *et al.*, 2006).

$$
b_i =
\begin{bmatrix}
-\cos\theta_{di} \\
\sin\theta_{di} \\
Z_{d1}\cos2\theta_{si} \\
-Z_{s1}\dfrac{C_{s1}}{C_{d1}}\sin2\theta_{di}
\end{bmatrix}
\text{ and } c_i =
\begin{bmatrix}
\sin\theta_{si} \\
\cos\theta_{si} \\
Z_{s1}\cos2\theta_{si} \\
-Z_{s1}\sin2\theta_{si}
\end{bmatrix}
\tag{2.14}
$$

By using matrix *a* with *b* and *c,* and applying Cramer's rule, we can summarise the equations by the evaluation of reflection and transmission coefficient as follows:

$$R_d = \frac{\det\left[a^{(1)}\right]}{\det[a]}, T_d = \frac{\det\left[a^{(2)}\right]}{\det[a]}, R_s = \frac{\det\left[a^{(3)}\right]}{\det[a]}, T_s = \frac{\det\left[a^{(4)}\right]}{\det[a]} \tag{2.15}$$

where $a^{(i)}$ is the matrix in which substitute by the *i*th column of matrix *a* by either *b* or *c* matrix and det[ ] is the determinant value of a matrix *a*.

2.3.3 Ultrasonic dispersion

Dispersion and attenuation of ultrasound are important material properties in non-destructive test and ultrasonic material characterization (Weaver and Pao, 1981). Ultrasonic wave dispersion is a phenomenon in which the ultrasonic wave propagates through a medium containing randomly scattered particles. Their properties cause multiple scattering of the ultrasonic wave resulting in the phase velocity varying as a function of frequency (Ye, 1997). Attenuation of an ultrasonic wave occurs when the ultrasonic wave propagates through materials, and the amplitude of the ultrasonic wave diminishes with distance. Such materials cause absorption and scattering of the traveling wave. Ultrasonic attenuation decreases the energy of the wave as it propagates through the material. Acoustic dispersion and attenuation techniques are generally based on broadband ultrasonic transmission have been applied in many applications introduced by (Sachse and Pao,1978). Through transmission and echo pulse mode measurements are examples of methods which have been used to evaluate ultrasonic dispersion and attenuation in the material (He, 1998). Those methods can be used for determining the phase velocity of a specimen. This velocity can be expressed by (Ping He, 2000) the following:

$$\frac{1}{V_p(f)} = \frac{\theta_s(f) - \theta_w(f)}{2\pi f L} + \frac{1}{c_w} \tag{2.16}$$

where $V_p(f)$ is the phase velocity in the specimen, c_w is the sound velocity in water, $\theta_s(f)$ and $\theta_w(f)$ are the phase spectrum calculated form the transmitted pulses with specimen $P_s(t)$ and without specimen $P_w(t)$ when the immersion experiment is performed for measuring attenuation and dispersion, and *L* is the thickness of the specimen.

The ultrasonic attenuation coefficient of a specimen (*A*) is acquired from the magnitude of an ultrasonic wave traveling before and after through the specimen. The combination of absorption and scattering in the specimen causes a decay rate of a wave when

propagating through the specimen. This attenuation coefficient is given by He and Zheng, (2001).

$$A = \frac{ln(T)}{2L} + \frac{1}{2L}\ln\left(\frac{M_1}{M_2}\right)$$

(2.17)

In this study, if we know the density of specimen, the value of T can be calculated by equation (2.18) for substitution the term $ln\ (T)$ in equation (2.17),

$$T = 4(\rho V_p)(\rho_w c_w)/(\rho V_p + \rho_w c_w)^2$$

(2.18)

where ρ and ρ_w are the density of the specimen and water. M_1 and M_2 are amplitudes of the Fourier transform of a pulse reflected back from the front and back surfaces of a specimen.

Transducer diffraction effects can occur when the size of receiving and transmitting is a finite size. When a plane wave of an ultrasonic beam travels from the transmitting to receiving transducers, beam scattering causes a change of the phase and signal amplitude spectra of the received signals. The correction of diffraction effects can be investigated and compensated by (He and Zheng, 2001)

$$D_L = 1 - e^{-j(\frac{2\pi}{s})}\left[J_0(\frac{2\pi}{s}) + jJ_1(\frac{2\pi}{s})\right]$$

(2.19)

where D_L is the diffraction correction value by applying Lommel function expressed in (Rogers and Van Buren, 1974). This value varies on the single composite variable $s = zc/(fa^2)$ where z is the distance between transmitting and receiving transducer c is the speed of sound in material, f is ultrasonic frequency and a is the radius of transducer. In this study, the through transmission mode was implemented for evaluating attenuation coefficient then the parameter s can be given as following.

$$s_w = \frac{zC_w}{fa^2}\ , \qquad s_s = \frac{(z-L)C_w}{fa^2} + \frac{LV_p(f)}{fa^2}$$

(2.20)

2.4 Nonlinear Ultrasound

Nonlinear ultrasound is an ultrasonic non-destructive testing which can investigate or characterise a defect in materials. The characteristic of the system is the evaluation of additional frequency components occurring when an ultrasonic wave propagates and then interacts with a material's defect. Their interaction is a cause of the frequency component

generation called harmonic frequencies, used for a deflection identification. These harmonics are not shown in an excited signal which consists of the difference and sum frequencies; in contrary to conventional linear method which measures the amplitude and phase of the signal at the same excited frequency for measurement of transmission and reflection. This section provides a theoretical background to the nonlinear ultrasonic techniques as they relate to detecting and characterising material properties.

2.4.1 Noncollinear ultrasonic wave mixing

Noncollinear wave mixing is based on the interaction between two plane elastic waves that results in a third wave. When two elastic waves, ω_1 and ω_2, propagate in a solid and interact with each other, they produce a secondary wave called wave-mixing. The response of interaction is the sum and the different frequency ω_g.
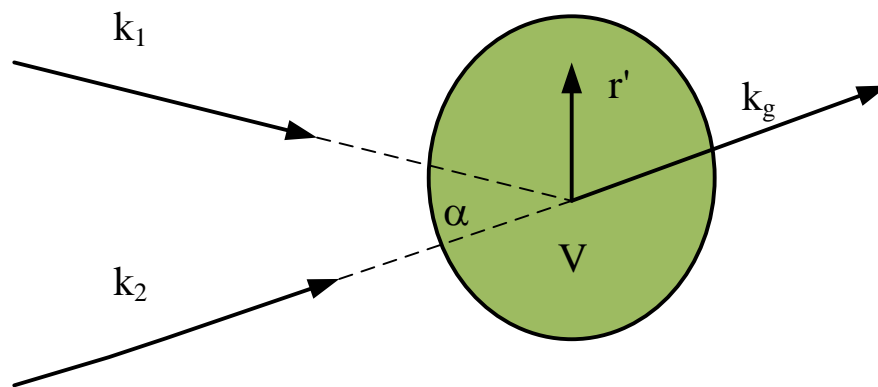
Figure 2-2: Interaction of two plane waves in volume V of a nonlinear elastic material when k_1 and k_2 are wave vectors of the angular frequency ω_1 and ω_2 respectively. The k_g is a resulting wave vector from the interaction with the sum or difference frequencies $(\omega_g = \omega_1 \pm \omega_2)$ (taken from Korneev and Demčenko, 2014)

The resonance interaction conditions have been studied in several combinations of ultrasonic waves (Korneev 1998, Korneev and Demčenko 2014). However, most combinations used for detection in solid material involve an incident shear wave interacting with a longitudinal wave to generate a longitudinal wave (Demčenko, Koissin and Korneev, 2014). The solutions of these interactions can be found in the literature (Korneev VA 2014,Wu 2017). Their interaction parameters consist of an interaction angle (α), scattering angle (ψ) and an amplitude coefficient (w). Korneev and Demčenko, 2014 has shown and summerised all types of nonlinear scattering coefficient of two plane elastic wave resonant interactions which can be divided in to sum and difference frequencies of the two scattered waves as shown in (Table2-1). All ten types of elastic wave resonant interactions are possible and suitable to various applications of research (Croxford *et al.*, 2009; Novak *et al.*, 2012; Demčenko *et al.*, 2012; Demčenko, Koissin and Korneev, 2014b; Ju *et al.*, 2017). In order

to analyse nonlinear wave interactions, those parameters are computed with specific constants.The tangent of the scattering angle between k_1 and k_2 can be expressed as:

$$tan(\psi) = \frac{\pm \frac{c_1}{c_2} d \, sin\alpha}{\pm \frac{c_1}{c_2} d \, cos\alpha} \, , \tag{2.21}$$

where d is the frequency ratio, and c_1 and c_2 are longitudinal and shear wave velocities propagating in material of density ρ ,given by Equation 2.22

$$c_1 = c_L = \sqrt{\frac{\lambda + 2\mu}{\rho}} \quad and \quad c_2 = c_S = \sqrt{\frac{\mu}{\rho}} \, . \tag{2.22}$$

The frequency reatio d can be expressed as Equation (2.23)

$$d = \frac{\omega_1}{\omega_2} \quad and \quad \gamma = \sqrt{\frac{\mu}{\lambda + 2\mu}} \, . \tag{2.23}$$

In addition, the relationships between the parameters depend on the type of interaction (Table 2-1: column 4 and 5). The interaction angle (α) is the angle between k_1 and k_2. For instance in the case of the interaction of two shear waves (interation 8), the sum of k_1 and k_2 can only generated a longitudinal wave if they satisfy a resonance condition (Korneev and Demčenko, 2014).The angle α of interaction is given by:

$$cos(\alpha) = \gamma^2 + \frac{1}{2}\left[\frac{1}{d} + d\right][\gamma^2 - 1] \, . \tag{2.24}$$

However, the expressions for the calculation interaction angle depend on the case of interaction as described in (Table 2-1: column 3). In addition the calcuation of the interaction angle and scattering angle also depend on range of values of the frequency ratio (d), expressed in terms *dmin*, *dmax*. Most interaction cases (Table 2-1) exist in a finite range between *dmin* and *dmax*, except for interaction cases 1 and 2, which grow as the frequency ratio d increases.

Table 2-1: Nonlinear scattering coefficients of two planes elastic wave interaction (Korneev and Demčenko, 2014)

	Interaction	$\cos\alpha$	d_{min}	d_{max}	Scattering coefficient (w)
1	$L(\omega_1)+L(\omega_2)$ $\to L(\omega_1+\omega_2)$	1	0	∞	$D_L\dfrac{1+d}{2}(4C_1+2C_2+2C_{3+}C_4+C_5)$ $\approx D_L(1+d)(2m+l)$
2	$L(\omega_1)+L(\omega_2)$ $\to L(\omega_1-\omega_2)$	1	0	1	$-D_L\dfrac{1+d}{2}(4C_1+2C_2+2C_{3+}C_4+C_5)$ $\approx -D_L(1+d)(2m+l)$
3	$L(\omega_1)+L(\omega_2)$ $\to SV(\omega_1-\omega_2)$	$\dfrac{1}{\gamma^2}-\dfrac{1}{2}\left(d+\dfrac{1}{d}\right)\times$ $\left(\dfrac{1}{\gamma^2}-1\right)$	$\dfrac{1-\gamma}{1+\gamma}$	1	$-D_S\dfrac{1+d}{4}\gamma^2\sin 2\alpha\,(2C_1+C_2+C_3)$ $\approx -D_s(1+d)\gamma^2\sin 2\alpha/2$
4	$L(\omega_1)+SV(\omega_2)$ $\to L(\omega_1+\omega_2)$	$\gamma-\dfrac{d}{2}\left(\dfrac{1}{\gamma}-\gamma\right)$	0	$\dfrac{2\gamma}{1-\gamma}$	$-\dfrac{D_L}{\gamma^3}\dfrac{\sin\alpha}{1+d}(C_1(3d\gamma+2q)+C_2q\ldots)$ $+C_3(d\gamma+q)+d\gamma C_5)$ $\approx -\dfrac{D_L}{\gamma^3}\dfrac{\sin\alpha}{1+d}(d\gamma+q)m$ $q=\cos\alpha\,(2d\gamma\cos\alpha+d^2+2\gamma^2)$
5	$L(\omega_1)+SV(\omega_2)$ $\to L(\omega_1-\omega_2)$	$\gamma-\dfrac{d}{2}\left(\dfrac{1}{\gamma}-\gamma\right)$	0	$\dfrac{2\gamma}{1+\gamma}$	$-\dfrac{D_L}{2\gamma^3}\dfrac{\sin\alpha}{1+d}(C_1(3d\gamma+2q)+C_2q\ldots.)$ $+C_3(d\gamma+q)+d\gamma C_5)$ $\approx -\dfrac{D_L}{\gamma^3}\dfrac{\sin\alpha}{1-d}(d\gamma+q)m$ $q=-\cos\alpha\,(2+2d+d^2)$
6	$L(\omega_1)+SV(\omega_2)$ $\to L(\omega_1-\omega_2)$	$\dfrac{1}{\gamma}-\dfrac{1}{2d}\left(\dfrac{1}{\gamma}-\gamma\right)$	$\dfrac{1-\gamma}{2}$	$\dfrac{1+\gamma}{2}$	$\dfrac{D_s}{2\gamma^3(1-d)}\left(C_1(2qd-\gamma^2\cos 2\alpha+\gamma d\cos\alpha)\right)\ldots$ $-C_2q\gamma\cos\alpha\ +C_3\,\gamma^2\sin^2\alpha+C_5dq)$ $\approx -\dfrac{D_s}{2\gamma^3}\dfrac{m}{1-d}(2d\gamma\cos\alpha-d^2-\gamma^2\cos 2\alpha)$ $q=\gamma\cos\alpha-d$
7	$SV(\omega_1)+L(\omega_2)$ $\to L(\omega_1+\omega_2)$	$\gamma-\dfrac{1}{2d}\left(\dfrac{1}{\gamma}-\gamma\right)$	$\dfrac{1-\gamma}{2\gamma}$	∞	$\dfrac{D_L}{2\gamma^3}\dfrac{\sin\alpha}{1+d}(C_1(3d\gamma+2q)+C_2q\ldots)$ $+C_3(d\gamma+q)+d\gamma C_5)$ $\approx \dfrac{D_L}{\gamma^3}\dfrac{\sin\alpha}{1-d}(d\gamma+q)m$ $q=\cos\alpha\,(2+2d+d^2)$
8	$SV(\omega_1)+SV(\omega_2)$ $\to L(\omega_1+\omega_2)$	$\gamma^2-\dfrac{1}{2}\left(d+\dfrac{1}{d}\right)\times$ (γ^2-1)	$\dfrac{1-\gamma}{1+\gamma}$	$\dfrac{1+\gamma}{1-\gamma}$	$D_L\dfrac{1+d}{2\gamma^2}(C_1\cos 2\alpha+C_2\cos^2\alpha-C_3\sin^2\alpha)$ $\approx D_L\dfrac{1+d}{2\gamma^2}m\cos 2\alpha$
9	$SH(\omega_1)+SH(\omega_2)$ $\to L(\omega_1+\omega_2)$	$\gamma^2-\dfrac{1}{2}\left(d+\dfrac{1}{d}\right)\times$ (γ^2-1)	$\dfrac{1-\gamma}{1+\gamma}$	$\dfrac{1+\gamma}{1-\gamma}$	$\dfrac{D_L}{2\gamma^4(1+d)}(C_1(2d+\cos\alpha(1+d^2))\ldots$ $+C_2\gamma^2\cos\alpha(1+d^2)$ $\approx \dfrac{D_L}{2\gamma^4(1+d)}[m\gamma^2\cos\alpha(1+d)^2\ldots$ $+n(2d+\cos\alpha(1+d^2\ \ \ -\gamma^2(1+d)^2))]$
10	$L(\omega_1)+SH(\omega_2)$ $\to SH(\omega_1-\omega_2)$	$\dfrac{1}{\gamma}-\dfrac{1}{2d}\left(\dfrac{1}{\gamma}-\gamma\right)$	$\dfrac{1-\gamma}{2}$	$\dfrac{1+\gamma}{2}$	$\dfrac{D_s}{2\gamma}[C_1\cos 2\alpha(2d\cos\alpha-\gamma)-C_2\gamma\cos\alpha+C_5d]$ $\approx D_s[2m(d-\gamma\cos\alpha)-n d\sin^2\alpha]/4\gamma$

Table 2-2: Mechanical properties of specimen used in the nonlinear wave interaction analysis.(taken from Catheline, Gennisson and Fink, 2003; Demčenko, Koissin and Korneev, 2014)

Material	$\rho(\text{kg/m}^3)$	$\lambda(\text{GPa})$	$\mu(\text{GPa})$	$l(\text{GPa})$	$m(\text{GPa})$	$n(\text{GPa})$
PVC	1350	3.64	1.83	-33.45	20.88	-15.86
Agar	1086	2.25	0.9	23.936	-12.032	-6.4

Another important parameter of the nonlinear interaction is the scattering amplitude coefficient (w) also a function of the frequency ratio (d). The resonant scattering amplitude coefficient can be calcuated using the expression (Table2-1: column 6).

$$w = D_L \frac{1+d}{2\gamma^2} m \cos 2\alpha \tag{2.25}$$

In addition, the following equation is used for the computation of the scattering coefficient.

$$D_L = \frac{d}{4\pi(\lambda + 2\mu)} \left(\frac{\omega_1}{v_l}\right)^3 \tag{2.26}$$

The Equations in Table 2-1 permit us to detemine the resonance conditions of the nonlinear interaction of two waves. Here, these expressions are used for an analysis of nonlinear wave interactions which can be applied in various interaction cases with the material properties. In order to calculate (w), (α) and (ψ), the material properties need to be specified to implement the Equations in Table 2-1. An example of solid material properties is shown in Table 2-2. Those value are elastic constants represent the relationship of stress and strain, which can be used to define a two-dimensional (6×6 matrix) state of stress called constitutive relationship. Normally, the elastic constant elements of the constitutive matrix are expanded by Talor series. For the nonlinear interactions in this study, we use Lamè constants λ, μ as second order elastic constants and l, m, n are third order elastic constants. Those constants have been widely used for acousto-elastic measurement methods (Egle and Bray, 1976; Kostek, Sinha and Norris, 1993). In this study, these properties are an example of analytical estimation of the nonlinear wave interaction in PVC and Agar materials. The estimation results not only show the relationship between ratio of two interacting waves and the angle of interaction but also the scattering amplitude coefficient.

2.4.2 Collinear ultrasonic wave mixing

2.4.2.1 Bispectral analysis

Bispectral analysis is a method which is powerful for identifying the weak nonlinearities in non-destructive testing such as micro-cracks and fatigue damage. This technique has been demonstrated by Donskoy *et al*, 2001 using the modulation of a high frequency ultrasonic wave and low frequency vibration to probe the response of the sum and difference frequencies. This method has also been used in the analysis of nonlinear acoustic characterization (Worden *et al.*, 2008). Generally, the bispectrum is the Fourier transform of the second-order spectrum signal that results in a frequency 1-frequency 2-amplitude correlation (Courtney *et al.*, 2010). In order to understand the bispectrum method used for the analysis of nonlinear wave modulation, a one dimensional nonlinear elastic wave is considered first. The equation can be expressed as shown in Equation (2.27).

$$\frac{\partial^2 y(x,t)}{\partial t^2} = c^2 \frac{\partial^2 y(x,t)}{\partial x^2} + c^2 \beta \frac{\partial^2 y(x,t)}{\partial x^2} \frac{\partial^2 y(x,t)}{\partial x^2} \tag{2.27}$$

$$y(x,t) = \eta y^0(x,t) + \beta y^1(x,t) \tag{2.28}$$

where y is the particle displacement, x is the distance wave travels in time t, and c is wave speed. $y(x,t)$ combines the linear and nonlinear particle displacement, y^0 and y^1, respectively with linear components, (η) and (β). The displacement y in Equation (2.27) can be rewritten in Equation (2.28), and the propagation of y^1 over distance x is assumed to be.

$$y^1(x,t) = xf(\tau) \tag{2.29}$$

τ is a propagation time in which a particle moves along a distance x, $\tau = t - x/c$. Then the input system consists of two sinusoidal frequencies,

$$y(x,t) = A_1 \cos(f_1 t - k_1 x) + A_2 \cos(f_2 t - k_2 x) \tag{2.30}$$

where A_1, A_2 are amplitudes of the harmonic wave, f_1, f_2 are central harmonic frequenies, and k_i are the wavenumbers $k_1 = f_1/c$, $k_2 = f_2/c$. The function $f(\tau)$ can be caculated by substituting Equations (2.30, 2.29 and 2.28) into (2.27) (Li *et al.*, 2016). After substituting, $f(\tau)$ can be expressed as

$$f(\tau) = -\frac{A_1^2 k_1^2}{8} \cos(2f_1\tau) - \frac{A_2^2 k_2^2}{8} \cos(2f_2\tau)$$

$$+\frac{A_1 A_2 k_1 k_2}{4} [\cos((f_1 - f_2)\tau - \cos(f_1 + f_2)]$$

(2.31)

Then, $y(x,t)$ can be derived as Equation (2.32)

$$y(x,t) = y^0(x,t) + y^1(x,t)$$

$$= A_1 \cos(f_1 \tau) + A_2 \cos(f_2\tau)$$

(2.32)

$$+x\beta \left\{ -\frac{A_1^2 k_1^2}{8} \cos(2f_1\tau) - \frac{A_2^2 k_2^2}{8} \cos(2f_2\tau) \right.$$

$$\left. +\frac{A_1 A_2 k_1 k_2}{4} [\cos((f_1 - f_2)\tau - \cos(f_1 + f_2)] \right\}.$$

According to Equation (2.28), the response consists of η and β representing linear and nonlinear acoustic coefficients. The nonlinear coefficient β multiplies the second harmonic $(2f_1)$ frequency component. The β value can therefore be calculated from the second harmonic component. $A_1, A_2, f_1, f_2, \emptyset_1$ and $\emptyset_2$ are defined respectively as the amplitudes, frequencies and initial phases of the sinusoids. The powers pectrum of $y(x,t)$, Equation (2.32), can be expressed in the frequency domain by using the Fourier transform.

$$Y(x,f) = -i\frac{\alpha A_1}{2}\delta(f_1 - f)e^{j\emptyset_1} - i\frac{\alpha A_2}{2}\delta(f_2 - f)e^{j\emptyset_2}$$

$$-i\frac{\beta A_1^2}{4}\delta(2f_1 - f)e^{j\emptyset_1} - i\frac{\beta A_2^2}{4}\delta(2f_2 - f)e^{j\emptyset_2}$$

(2.33)

$$+i\frac{\beta A_1 A_2}{2}\delta(f_2 - f_1 - f)e^{j(\emptyset_2 - \emptyset_1)}$$

$$-i\frac{\beta A_1 A_2}{2}\delta(f_2 + f_1 - f)e^{j(\emptyset_2 + \emptyset_1)}$$

According to the interaction of ultrasonic waves, the nonlinearity of material causes harmonic waves at $2f_1, 2f_2$ and sidebands at the sum and difference frequency $f_1 + f_2$ and $f_1 - f_2$. Note that the signals resulting from the nonlinearity are related in phase to those that generated them by relationships $f_3 = f_1 + f_2$. These spectral components result from the constant phase differences associated with $0 = \emptyset_1 + \emptyset_2 - \emptyset_3$, called quadratic phase coupling. This can be considered an indication of second-order nonlinearities in the system and offers an approach for differentiating signals at a specific frequency.

The general linear power spectrum will provide the Fourier transform of the second-order cumulant without phase information. For higher-order spectral density, the bispectrum is the result of Fourier transform of the third-order cumulant-generating function wih the quadratic phase. This phase has been used effectively by Courtney *et al.*, (2008) for evaluating the quadratic phase coupling types of nonlinear effects in mechanical systems.

For a random input signal $y(t)$, the bispectrum is expressed by

$$B(f_1, f_2) = E[Y(f_1) \, Y(f_2) \, Y^*(f_1 + f_2)] \,.$$

(2.34)

To make clearly describes the validity of the bispectrum for the identification of quadratic phase coupling, The $\emptyset_3$ term is substituted to $\emptyset_1 + \emptyset_2$ in Equation (2.25), thus

$$\begin{aligned}
y(x,t) = \; & \alpha \, A_1 \, sin(2\pi \, f_1 \, t \; + \emptyset_1) + \alpha \, A_2 \, sin(2\pi f_2 \, t \; + \; \emptyset_2) \\
& - \beta \frac{A_1^2}{4} \cos[2\pi(2f_1)t \; + \; 2\emptyset_1] \\
& - \beta \frac{A_2^2}{2} \cos[2\pi(2f_2)t \; + \; 2\emptyset_2] \\
& + \beta \, A_1 \, A_2 \cos[2\pi \, (f_2 - f_1)t + \; (\emptyset_2 - \emptyset_1 \,)] \\
& - \beta \, A_1 \, A_2 \cos[2\pi \, (f_2 + f_1)t + \; \emptyset_3] \,.
\end{aligned}$$

(2.35)

Chapter 3   Material and Method

3.1 Introduction

This chapter provides detailed information on the experimental setup used to perform the nonlinear ultrasonic measurement in this thesis. This section is focused on how the hardware setup and experimental procedures were implemented as well as the parameters affecting the ability of experimental measurement system. The chapter is organised as follows:

Section (3.2) describes the experimental non-collinear wave mixing setup and the required apparatus are shown for implementations.

Section (3.3) describes the instrumentation used for the collinear wave mixing experiment, including details of the setup parameters.

Section (3.4) contains details of the processes for preparing the tissue phantom.

Section (3.5) presents the technical data of ultrasonic traducers used for this study.

3.2 Non-collinear wave mixing experimental setup

The non-collinear wave mixing measurement was conducted for the detection of the scattered wave amplitude based on two ultrasonic wave interactions. The interaction condition, as shown in Table 2.1, was selected for measurement, depending on the condition described by Demčenko et al. 2014. To reach a suitable condition point, an analysis of the nonlinear wave interaction was performed for acquiring interaction parameters. Also, an arrangement of ultrasonic transducers with a specific geometry was implemented. This section not only describes the method to calculate important parameters which are used for evaluation of the non-collinear wave interaction point but also includes the method for transducer arrangement.

3.2.1 The nonlinear wave interaction analysis

For nonlinear wave interaction analysis, there are minimally three parameters we need to calculate: the interaction angle (α), scattering angle (ψ) and the amplitude coefficient (W). We must evaluate these parameters for a specific material. For this analysis, we chose polyvinyl chloride (PVC) because it is a common material, the properties of which (such as density, elastic constants and acoustic velocity) have been studied in detail. According to Table 2.1, the combination $SV(\omega_1) + L(\omega_2) \rightarrow L(\omega_1+\omega_2)$ (case #7) was selected for interaction analysis because the combination of the diffeent wave modes can be

easily distinguished, and applied to the third-order elastic constants of PVC, with their values as shown in Table 2.2. Those constants were taken to calculate the interaction parameter in the following steps:

1) Finding the interaction angle using Equation (2.24) with the substitution from Equation (2.23). The angle α of interaction relates to the frequency ratio and the γ parameter.

2) Calculation of scattering angle using Equation (2.21).

3) Evaluation of scattering coefficients as a function of frequency ratio by implementation of Equation (2.25, 2.26).
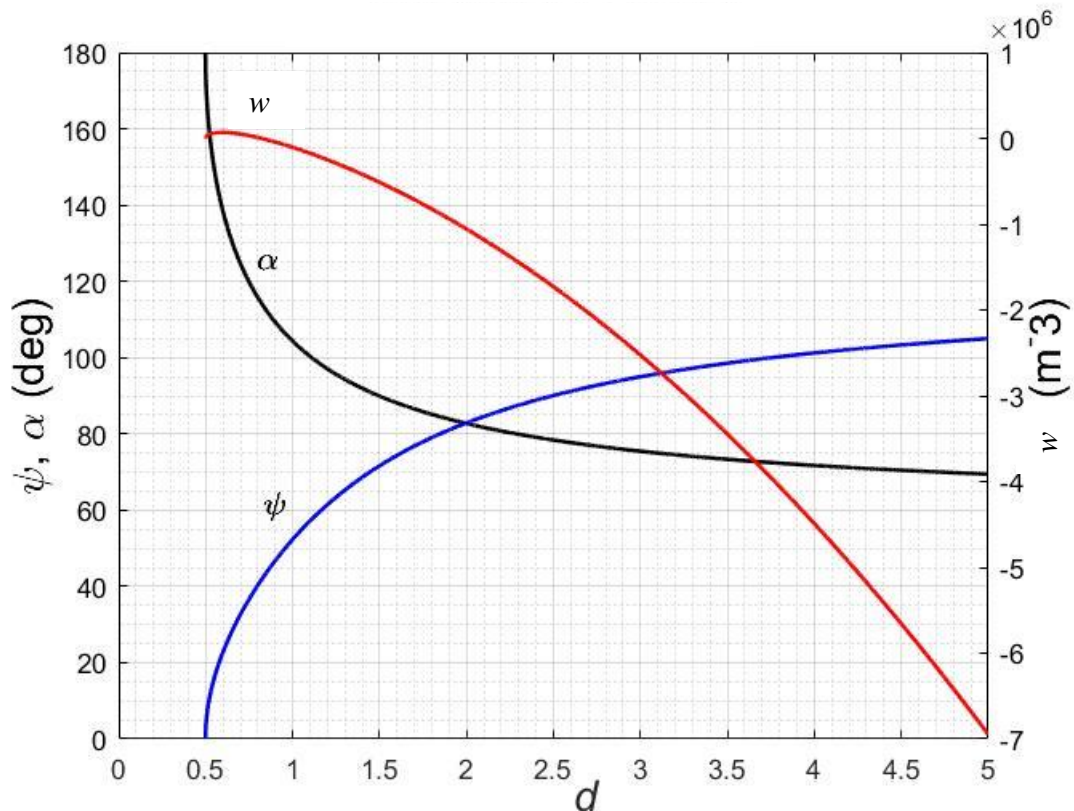
Figure 3-1: The nonlinear interaction of case $SV(\omega_1) + L(\omega_2) \rightarrow L(\omega_1 + \omega_2)$ was shown after implementation via Equations 2.25 and 2.26. When shear wave and longitudinal wave propagated and interacted in a material, the interacted angle and scattered angle of those wave were shown by black graph (α) and blue graph (ψ) and the colelation with the apmlitude coefficient (red graph). The interation of wave can be defined by a frequency ratio (d) with having the relationship an interaction angle, a scattering angle and an amplitude coefficient for example at 1.5 frequency ratio, the interaction point would be coccured at $\alpha = 90°$, $\psi = 70°$ and the coefficient of signal amplitude equals $- 0.6 \times 10^6$ (m^{-3}).

The result of the implementation of Equation (2.25 and 20.26) are shown in Figure 3-1 which includes the interaction angle (α), scattering angle (ψ) and amplitude coefficient (w) as a function of frequency ratio (d). The interaction graph is used for predicting where an intersected zone exists, for example, for $f_1 = 2.5$ MHz, if the frequency ratio (d) is 1.5 times of f_1, then the frequency (f_2) equal 3.75 MHz, with interaction angle and scattering

coefficient determined on the graph. When the resonance condition (d = 1.5, α = 90°, ψ = 70° and w = -0.6 m^{-3}) mentioned above is satisfied, the two incident waves   (the shear and longitudinal waves) interact at an area in which the material displays nonlinear mechanical properties; and a mixing wave can be produced with a combined frequency and its propagation related to those of the interaction angle and scattering coefficient. The third wave, therefore, results from a sum-frequency shear and longitudinal wave and can be taken as a sensing signal used for detecting nonlinearities of a material or physical aging. The third wave intensity can be used to indicate how much nonlinearity contributes to the material properties. The third wave frequency equals f_1 + f_2, which result from the combination of shear and longitudinal waves. In order to get the wave mixing energy, the fundamental signal recorded by a receiving transducer needs to filtered and calculated as shown next in the section.

3.2.2 Geometry for wave mixing configuration

In order to reach resonant condition for wave mixing, all of the ultrasonic transducers (transmitter and receiver transducers) were arranged with specific angles to the specimens. A particular geometry configuration is shown in Figure 3-2 which consists of angles and distances of transducers. Those angles of the geometry can be calculated by Snell's Law which describes the relationship between incident angles and reflected angles on a specimen. Snell's Law relates the ratio of the sines of the incident angle and refracted angle, as shown in Equation (3.1). Other parameters are the distance the waves travel along their paths, which was evaluated base on trigonometric ratios. An example of Equation (3.2), distance J_1 equals distance ΔD_1 divided by $cos\theta_1$. Thus, the angles and distances using for transducer arrangement were calculated as shown in Figure 3-2.

The three ultrasonic transducers are arranged per Equations (3.1, 3.2). According to the combination of shear and longitudinal wave mixing, we can compute the incident angles (θ_{1S} and θ_{2L}) of the specimen because the angles depend on wave velocities in the specimen as described in (Demčenko, Koissin and Korneev, 2014). Then the distance between transducers and specimen (ΔZ_1 and ΔZ_2) are determined. ΔZ_1 and ΔZ_2 are related to the incident angles θ_{1S} and θ_{2L}, respectively. We must also calculate the distance ΔTr between the pump wave sources and the distance ΔR between receiver Rx and the specimen surface. The parameters defining the geometry utilized are listed in Table 3-1 for both PVC and PMMA specimens. The geometry for PVC is shown in Figure 3-3 for a specimen thickness of 9 mm.
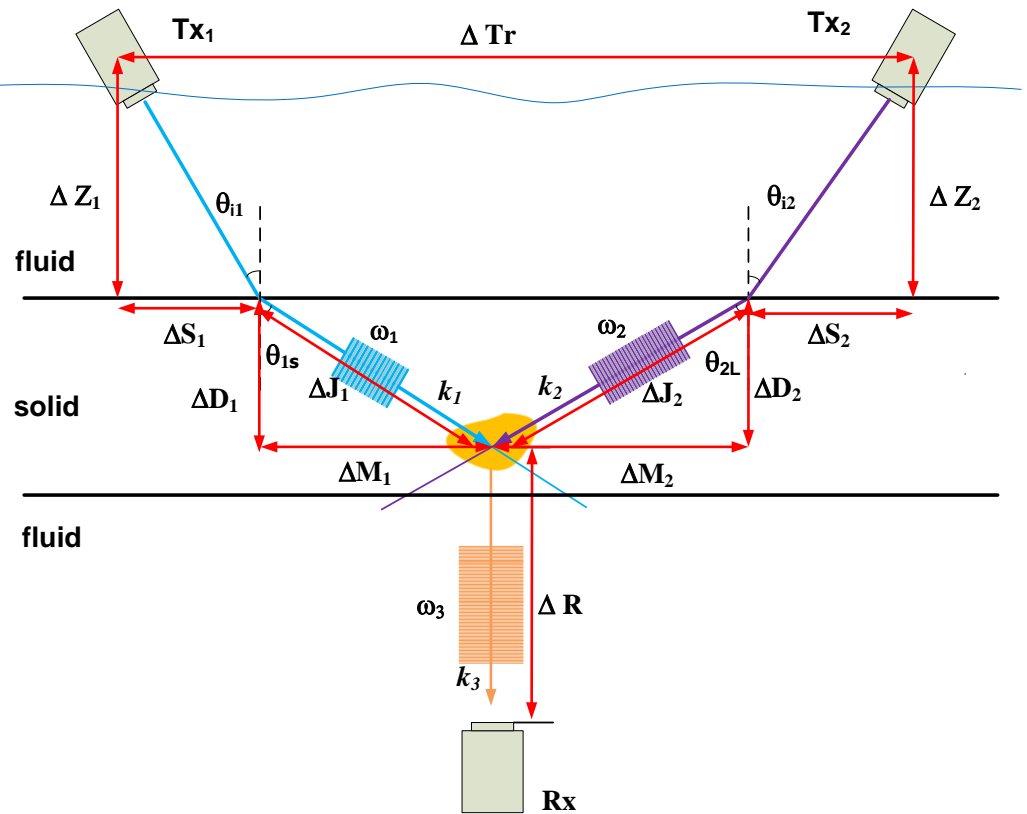
Figure 3-2 Through-transmission measurement mode set up. The image shows the arrangement of the nonlinear ultrasonic wave mixing for through-transmission measurement mode. Blue and purple lines mark the ultrasonic path signals from transmitters, and dashed lines denote the secularly reflected wave. The wave mixing signal is transmitted to the receiver sensor as shown by a red line.

$$\frac{sin\theta_1}{C_{l1}} = \frac{sin\theta_2}{C_{l2}} \tag{3.1}$$

$$\Delta J_1 = \frac{\Delta D_1}{cos\theta_1} \tag{3.2}$$

Table 3-1: Geometrical parameters used for setup the nonlinear ultrasonic wave mixing measurement.

Material	f_1 MHz	f_2 MHz	f_r MHz	θi_1 deg	θi_2 deg	ΔZ_1 mm	ΔZ_2 mm
PVC	2.5	3.75	6.25	52	31	25	40
PMMA	4	6	10	36	25	15	20.5
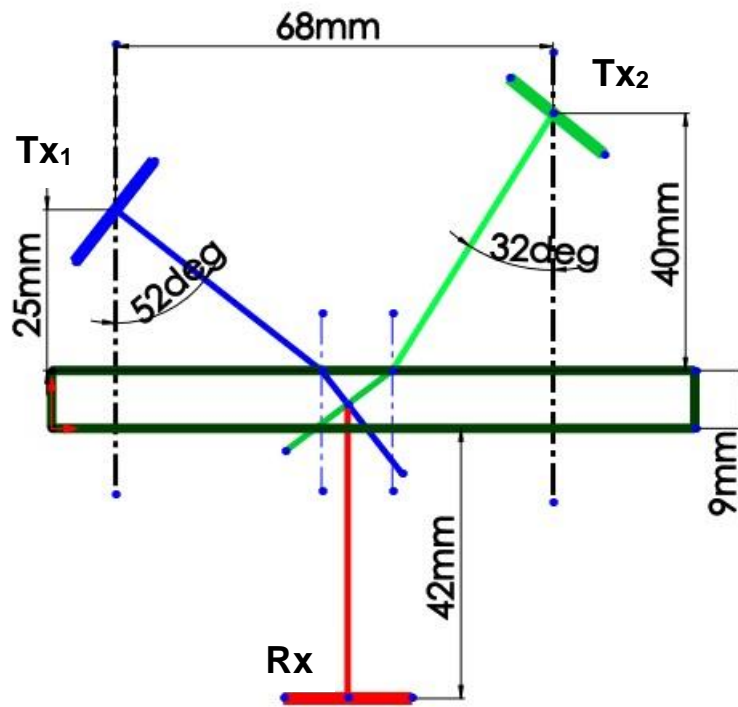
Figure 3-3: The three transducers are arranged on 9mm PVC with specific angles and distances (as shown in Table 3-6). The interaction occurs between two transmitted waves which refract from 32° (θ_{1s}) and 53° (θ_{2L}) angles. This point where different frequencies are mixed generates the third frequency, and their scattered wave can be probed by a receiver transducer.

3.2.3 Measurement setup

A non-collinear wave mixing system consists of three parts, namely: ultrasonic transducers, signal generators, and recording devices. A schematic diagram of a system of nonlinear ultrasonic wave mixing measurement is shown in Figure 3-4. The system operation started with two function generators (Aim TTi, TG5011) producing an RF burst, sent to RF power amplifier (TOMCO, BTM205-AlphaSA) to drive two ultrasonic transducers. Both transducers had a broadband frequency with a central frequency of 5 MHz used for excitation. A receiver transducer was a broadband transducer also with a central frequency 10 MHz. According to the interaction of ultrasonic wave mixing analysis and the resonance condition of shear wave, transducer 1 has a central frequency (f_1) of 2.5 MHz and the longitudinal wave of transducer 2 has a central frequency (f_2) of 3.75 MHz.

A refracted angle of the shear wave was 52° in PVC and driven by a burst of 20 cycles of rectangular pulse and a nominal refraction angle of the longitudinal wave was 31° with a driving burst of 20 cycles. The inclined transducers were adjusted manually by a rotary stage (Newport, M-481-A). A longitudinal receiver with a resonance frequency of 6.25 MHz was used with operation at the pulse-echo mode.
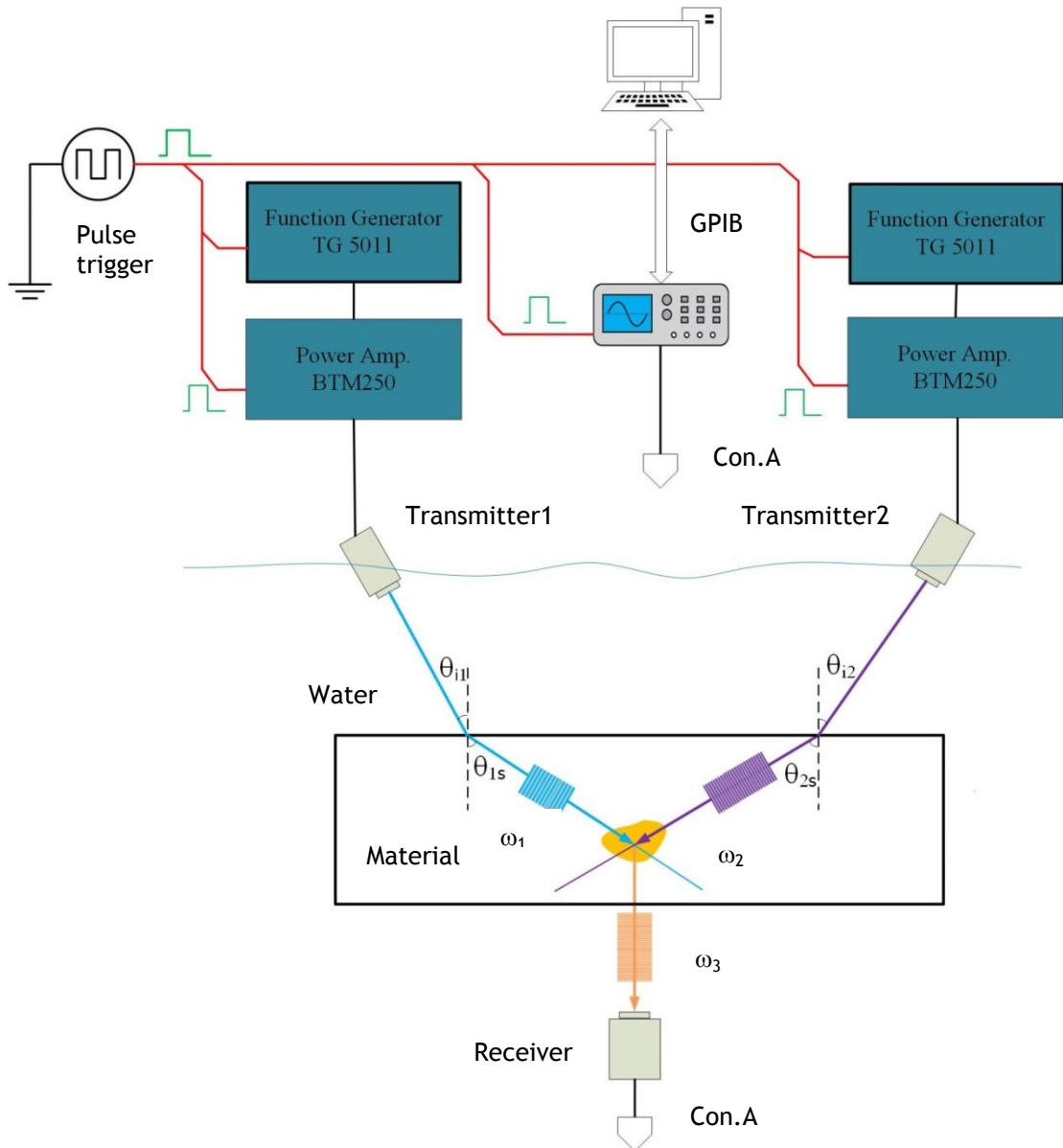
Figure 3-4 shows the arrangement of the nonlinear ultrasonic wave mixing for echo mode measurement. Blue and purple line mark the ultrasonic path signals from transmitters, and dashed lines note the secularly reflected wave. The wave mixing signal is reflected to the receiver sensor as shown by an orange line. A 400μS width pulse was excited by the function generator, sent through the power amplifier and oscilloscope for pumping (Transmitter 1,2) and acquiring (Receiver) by the ultrasonic transducers. A high-performance oscilloscope acquired the echo signal for the receiver programmed for recording the signal.

Synchronised operation between driving and acquiring signal was controlled by a triggering pulse generator with a frequency 20 Hz and 400 μs width. In that time, the two RF power amplifiers can drive generating shear and longitudinal waves propagated in the material. After mixing, a third longitudinal wave occurred and was measured by an oscilloscope (Agilent technologies, Infiniium 548330 MSO). Those signals were acquired with 62500 point resolution based on MATLAB programming through GPIB communication. Finally, signal information was further processed on the PC.

3.3 Collinear wave mixing

A wave mixing method interacted with the incident direction of two ultrasonic waves can be classified as non-collinear wave mixing (described in Section 3.2) and collinear wave mixing. In this section, the collinear wave mixing method applied to detect the nonlinearity of material is described with a detail of the experimental apparatus.

3.3.1 Measurement setup

The collinear wave mixing measurement system is based on two ultrasonic transducers used for excitation and receiver. The transmitter is used to drive two different sinusoidal frequencies (f_1, f_2) sent to a specimen, then nonlinearities in the specimen generate a third wave (f_3) detected by receiver transducers. The major components (Figure 3-5) consist of; 1) a function generator (Aim TTi, TG5011) for generating signals, and (2) RF power amplifier (TOMCO, BTM205-AlphaSA) for driving RF signals, and (3) an oscilloscope (Agilent technologies, Infiniium 548330 MSO) for collecting the signal data. The operation of the system started when the driving frequency f_1 (4.5MHz, 10cycle) and driving frequency f_2 (6.75MHz) was generated by a function generator of 500mVp-p amplitude. Before signals were sent to an exciting transducer, their signal was amplified by a 50dBm RF power amplifier. Two-component longitudinal waves propagated through the material, and interaction between the two excited waves with the nonlinearities of material generates a nonlinear ultrasonic wave. This third longitudinal wave was detected by the receiver and passed through a recorded oscilloscope. The functional oscilloscope was controlled by MATLAB programming. The MATLAB toolbox can communicate with the oscilloscope via GPIB communication. The instrument control toolbox has provided a function to configure, control, and acquire data from oscilloscope by writing code. In order to approach this, the Agilent oscilloscope needs a driver for GPIB communication and open MATLAB toolbox by type "tmtool" at the MATLAB command line.

20 Hz,400 μS width

Pulse Trigger

GPIB

Function Generator
TG 5011

RF Power Amplifier
BTM250-AlphaSA

Water

$\omega_1+\omega_2$ ω_3

Transmitte   Material   Receiver
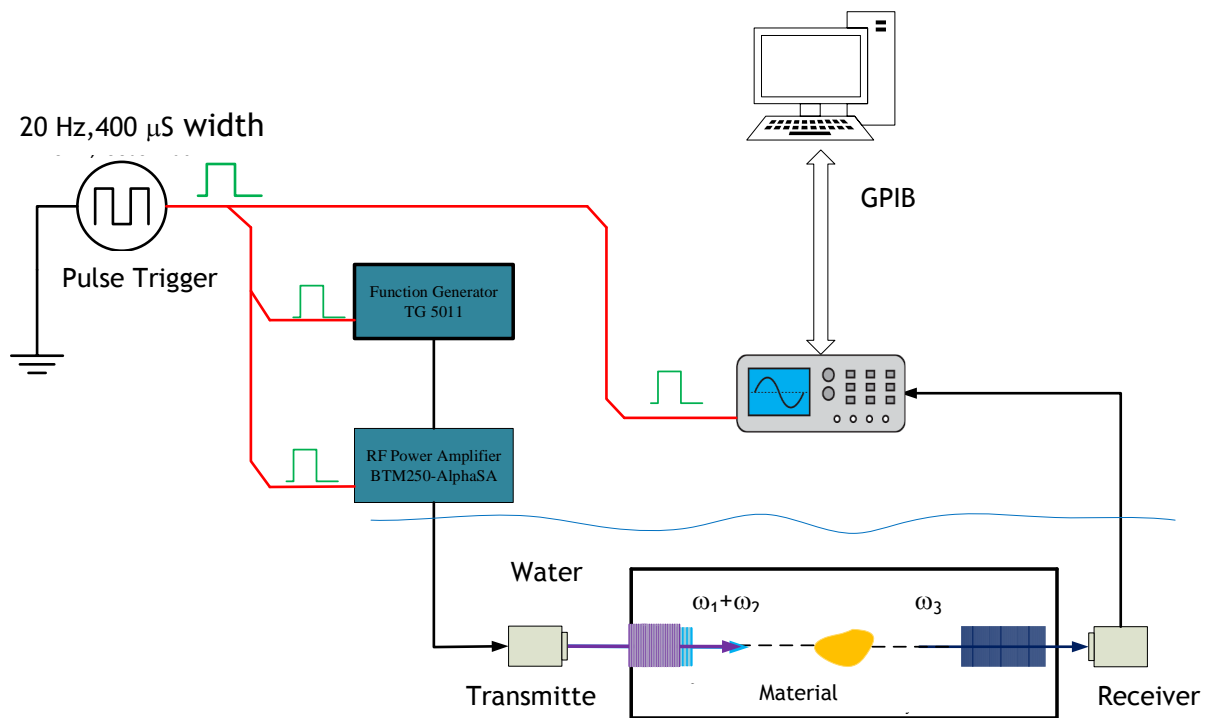
Figure 3-5: The collinear wave mixing system was performed in the water tank in order to avoid the physical contact problem. The impedance between transmitter, receiver, and the material has the lowest physical contact impedance because of the water impedance.
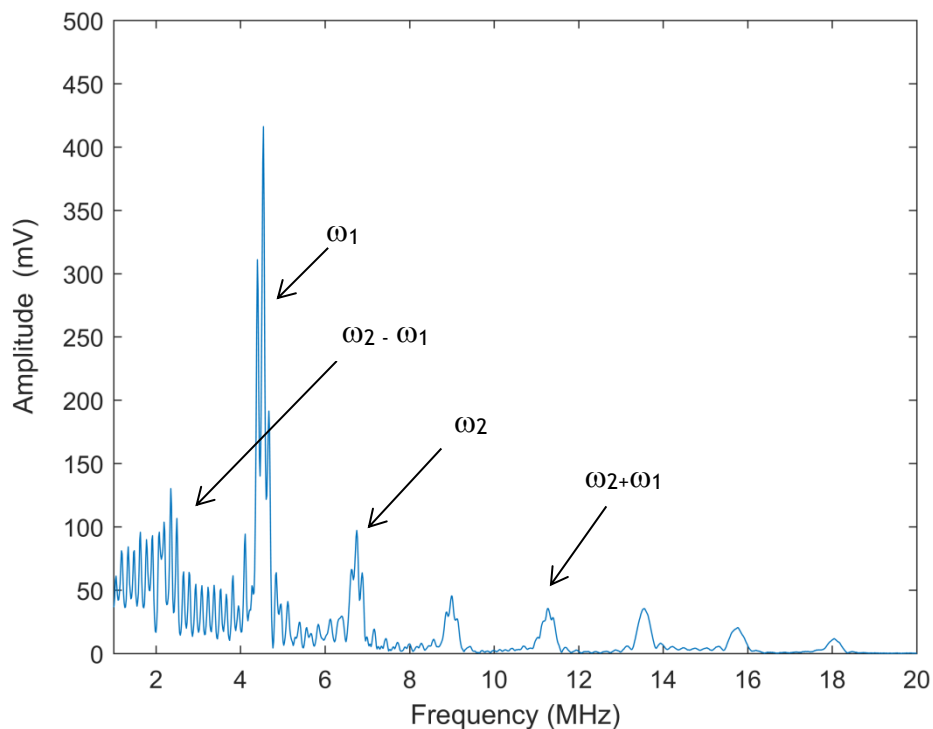
Figure 3-6: The signal which was picked up form receiver transducers   consists of the fundamental frequency (ω_1 and ω_2) difference and summing frequency ($\omega_{2\text{ - }\omega_1}$,$\omega_{2\text{ +}\omega_1}$) and the 2nd harmonic of fundamental frequencies.

3.4 Tissue mimicking phantom

Tissue phantom is an essential tool for studying the behaviour of a soft tissue for response to physical energy such as ultrasonic wave, microwave, laser and light. Their properties should provide the same physical properties as the tissue which include some specific acoustical, thermal and optical properties. The tissue mimicking phantom is an emulated biological tissue material with important properties for general purposes (Cao *et al.*, 2017) namely: 1) evaluating the performance of the devices for response of the soft tissue; 2) certifying the efficiency of the development of new devices or methods; 3) training physicians to understand the behaviour of those devices.

3.4.1 Acoustical phantom properties

Medical ultrasound imaging has been wieldy used for various applications which are essential to verify the performance of acoustic phantoms. The relevant acoustic properties of mimicking phantoms parameters are the speed of sound (c), the acoustic impedance (z), and the acoustic attenuation (α) which should have values similar to soft tissues. For instance, the phantom in this study has a speed of sound about 1560 m/s, the same as the average speed of sound in soft tissue (Culjat *et al.*, 2010).The phantom in this study was not only used for evaluating the deflection of ultrasonic waves when they strike a small particle but also used for mimicking the pressure ulcer as a lesion. An important example of acoustic properties of some typical soft tissues is shown in Table 3-2.

Table 3-2: Acoustic properties of some tissues (taken from Culjat *et al.*, 2010).

Material	Velocity(m/s)	Density(kg/m^3)	Attenuation (dB/cm MHz)	Acoustic Impedance(MRayl)
Air	330	1.2	0.00040	-
Blood	1584	1060	1.68	0.2
Brain	1560	1040	1.62	0.6
Breast	1510	1020	1.54	0.75
Cornea	1587	1076	1.71	-
Fat	1478	950	1.40	0.48
Kidney	1560	1051	1.64	1.0
Liver	1595	1060	1.69	0.5
Muscle	1574	1050	1.62	1.09
Tendon	1670	1100	1.84	4.7
Soft tissue	1561	1043	1.63	0.54
Water	1480	1000	1.48	0.0022

The phantoms are basically made of a composite material consisting of the matrix, solvent, scatterers and other materials. Much research has shown that various chemical materials can be efficiently used for phantom such as agar (Rajagopal, Sadhoo and Zeqiri, 2015), PVA (Fromageau *et al.*, 2007), PVCP (Cortela *et al.*, 2015), PAG or hydrogels (Choi *et al.*, 2013; Sun *et al.*, 2015). The advantages and disadvantages of those materials for phantom design have been reviewed by Fonseca *et al.*, 2016. In this thesis, a hydrogel was used to design the phantom because of ease of preparation and optical transparency. Details can be found in (Shieh *et al.*, 2014; Guntur and Choi, 2014; Sun *et al.*, 2015)

3.4.2 Hydrogel tissue phantom

The N-isopropylacrymide (NIPAM) is a polymer gel with a controlled "cloud point". The cloud point shows the ability for changing a structure from a hydrophilic structure when the temperature is below the cloud point, and to a hydrophobic structure when the temperature is above the cloud pint. The NIPAM-based hydrogel phantom is a reusable phantom made of crosslinking copolymerization of N-isopropylacrylamide (NIPAM) and N,N'methylenebisacrylamid (MBAm). The fabrication of the gel consists of chemicals shown in Table 3-3. Gel preparation was started with acrylic acid (AAc) an amount of 0.44 mL, dissolved with 150mL of degassed water. In order to adjust the cloud point to 52 °C, AAc was added. After the AAc completely solidifies in water then 9 g of NIPAM was added into the solution and then stirred at room temperature until complete dissolution of NIPAM. The 0.375 g of MBAm and 0.195 g of ammonium persulfate (APS) were added to their solution for acting as the initiator for crosslinking. Then the solution was slightly stirred at room temperature until uniform. Finally 0.4 ml of N,N,N,N'tetramethyLethy-lenediamidiamine (TEMED) for polymerization agent was added to the mixture solution.

Table 3-3: Combination of NIPAM-based hydrogel phantom (taken form Shieh *et al.*, 2014).

Components	Quantity
Degassed water	150ml
AAc	0.44ml
NIPAM	9g
MIBAm	0.375g
APS	0.195g
TEMED	0.4ml

Before the solutions began the polymerization processes, they were poured in molding containers of dimensions 50×40×30 mm to allow the polymerization processes

completely at room temperature. The container case was made of 3D printing materials (the blue) with a port for pouring the solution in the mold. Two sides of their mold were covered with a small sheet of plastic (0.17mm) and then they were compressed by two acrylic frames and mounted by hex bolts and nuts as shown Figure 3-7.
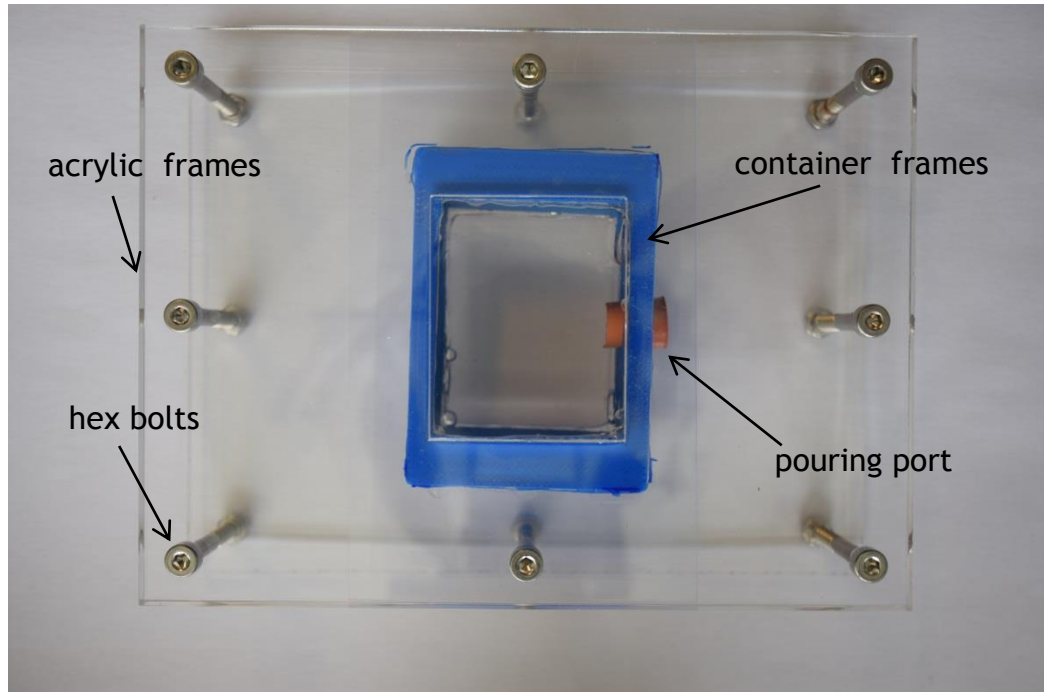
Figure 3-7: The mimicking tissue phantom has two transparent sides for propagating of the ultrasonic beam. The NIPAM solution was poured at the pouring port and then closed it after completed polymerization.

3.4.3 Thermal tissue phantom

A phantom having specific thermal properties was needed in some special medical applications, for example high intensity focused ultrasound (HIFU) and laser and microwave ablations. Their properties should be able to exhibit the ablation process during the thermal lesion formation. The thermal properties of these kinds of phantoms are specific heat, thermal conductivity, thermal resistivity, and diffusivity. However those thermal properties may be allowed in some parameters included with acoustic properties. Holt and Roy, (2001) reported using the phantoms having thermal properties for studying bubble boosted heating using focused ultrasound. The PVA and agar were proposed to make thermal tissue phantom with some added chemicals to adjust the specific heat and thermal conductivity. In addition, hydrogel phantoms with thermal properties have been proposed to be an effective thermal phantom for demonstration of thermal lesion formation in ultrasonic ablation as described in section 3.4.2 NIPAM-42 and NIPAM-52 are hydrogel materials that are optically

transparent at room temperature, become opaque when heated to 42 °C and 52 °C respectively, then become transparent again when cooled to room temperature.
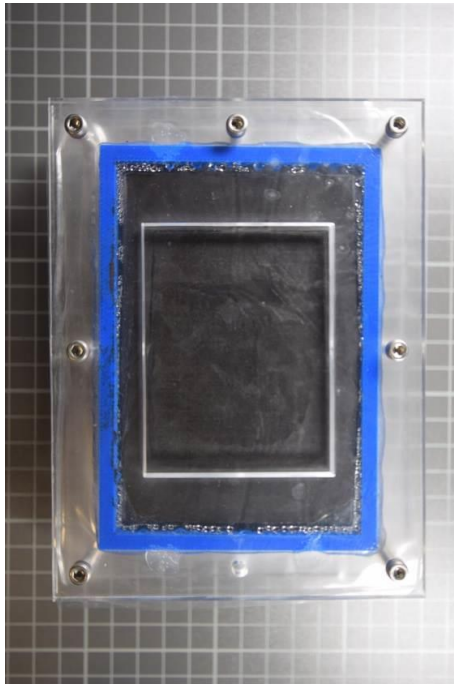
Table 3-4: the ingredients of PVA and agar used for thermal phantom (Holt and Roy, 2001).

Combination	PVA	agar
agar powder	-	18g
polyvinyl alcohol	20 g	-
water	600 ml	600ml
methyl paraben	750mg	750mg
graphite powder	65g	65g
1-propanol	18ml	48ml

Figure 3-8: The low cost phantom having thermal properties is shown on above image. The combination of agar and graphite powder including chemicals as show in Table 3-4 can provide specific thermal properties of phantoms.

Table 3-5: Thermal properties of biological tissue compared with NIPAM thermal phantom (Shieh *et al.*, 2014).

	Thermal conductivity (W/m K)	Specific heat (J/g K)
Human liver	0.572 ±0.009	3.628±0.078
Brain	-	3.86
Water	0.547	4.18
NIPAM-42	0.6 ±0.02	3.365±0.160
NIPAM-52	0.6 ±0.03	3.431±0.233
Egg white	0.59± 0.06	4.27±0.365
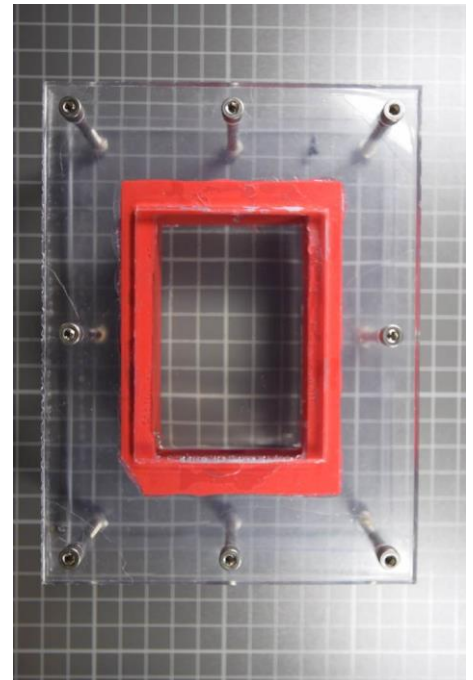
Figure 3-9 shows the transparent thermal phantom (NIPAM-52) with thermal conductivity and specific heat compared with biological tissue. Those specific properties provide the ability to change optical transparency when the temperature reaches the cloud point.

3.5 Transducer

The immersion ultrasonic transducers chosen in this experiment were a single element longitudinal wave transducer. Both the transmitter and the receiver transducers were a broad-band Piezoelectric Transducer. The transmitter transducer was used at a frequency of 10 MHz with unfocused transducer (flat type) and 50Ω interfacing impedance. For the receiver transducer, a focused transducer at 10 MHz (spot type) was chosen for probing the reflected signal because it can focus on a specific area with improved sensitivity. Both transducers were taken from Olympus Company and more detail is shown Table 3-6.

Table 3-6: The summarised transducer parameters for use in this experiment

Frequency (MHz)	Element size (mm)	Focus range (mm)	Near field (mm)	Type	Model
1	12.7	15.24 -20.32	26.44	flat	V303
5	8.2804	15.24 -59.69	75.31	flat	V326-SU
10	9.525	15.24 - 120.65	150.72	flat	V327-SU
10	9.525	25.4	150.72	focus	V327-SU-F1.00

3.6 Conclusion

This chapter reviewed two non-linear ultrasonic wave mixing techniques which were used for this study with some essential materials such as phantoms and transducers. There are basically two techniques for wave mixing: non-collinear and collinear wave mixing. Those techniques have specific arrangements with different abilities for practical measurement. The non-collinear ultrasonic wave mixing is based on two wave interactions with a opposite direction. The two inclined transducers were fixed with specific angles in order to reach resonance condition of wave interaction, thereby generating a third wave. The third wave was used for the evaluation material of properties. In the collinear wave mixing technique, the wave interaction occurs in the same transducer and then generates the sum and difference wave harmonics with unique properties. Additionally, the construction of a hydrogel phantom was described for tissue mimicking phantom used to simulate the deflected signal. The phantom was made of transparent hydrogel with the similar acoustic properties of the tissue. Finally, the ultrasonic transducer models were summarised, including important information for the experimental setup.

Chapter 4   Analysis of second-order nonlinear wave interactions

4.1 Introduction

The elasticity of tissue describes the tissue's ability to deforms and recover its original shape when external forces are applied. The responses of tissue are deformation (shape change) or the propagation of shear wave in it. This response can be used to characterize the tissue and identify a pathophysiological disease of tissues such as coronary, breast, kidney, liver, muscle, and skin (Glozman and Azhari, 2010). However, some studies have indicated the drawback of linear elasticity and suggested that using nonlinear elastic properties detection may be a promising solution. For example, Wellman *et al.*, (1999) reported that the linear elasticity might not differentiate a fibroadenoma (a starting state of tumour) from a normal invasive ductal carcinoma even though their moduli differ by about 2.5 times with a large strain excitation. They also reported that it might not be possible to distinguish between abnormal and normal tissues. Therefore, they proposed that nonlinear elastic properties might be more suitable for this problem.

Nonlinear material properties are defined as anharmonicity caused by intrinsic imperfections in the properties of the material. This behavior occurs when the microstructure of the material interacts with a propagating wave, leading to nonlinear vibration and distortion of elastic wave propagation. Here the nonlinearity of the material is an intrinsic property of the elastic material. Nonlinear soft tissue properties have been studied for medical diagnostic purposes (Jiang *et al.*, 2015; Koo, Cohen, and Zheng, 2011; Oberai *et al.*, 2009). However, there have been few works on the nonlinear elastic properties of tissue. Law, Frizzell, and Dunn, (1985) evaluated nonlinear elastic parameters (B/A) of tissue using thermodynamic and finite-amplitude methods. Erkamp *et al.* (2004) determined the nonlinear elastic properties of phantom materials using force-displacement data assuming incompressible materials. Destrade, Gilchrist and Saccomandi, (2010) reviewed the third and fourth-order constants which are useful for acousto elasticity studies in incompressible soft solids.

The nonlinear behavior of tissue results from various factors and is characterized by acousto elastic and stress-stain relationships (Van Den Abeele, Johnson and Sutin, 2000; Van Den Abeele *et al.*, 2000). The acousto elastic effect occurs when the elastic wave changes its speed while traveling in the material as a result of nonlinearities. The nonlinearity parameters of materials have been widely used for the investigation of third-order elastic

constants of tissue (Liu *et al.*, 2007; Dunn, 1986; Law, Frizzell and Dunn, 1985). The classical theory behind the nonlinear wave equation and the third-order elastic constants has been described by (Murnaghan, 1937), which described basic nonlinear phenomena based on stress-strain relations at equilibrium with virtual deformation of the elastic material. The useful summary of all possible nonlinear interactions of plane waves with an elastic solid is given in (Korneev VA, 2014; Korneev, 1998). Specifically, they reviewed ten combinations of second-order nonlinear interactions as described by nonlinear elastic constants. These interactions are used for nonlinear wave mixing evaluation. However, using nonlinear wave mixing for evaluation requires specific interaction conditions between the two incident waves. They must satisfy certain conditions to generate a mixing wave with an amplitude that is related to the properties of the damaged region. In addition, the combination signal generated from the mixing of the two waves is a fairly complex wave which requires interpretation. Therefore, to apply nonlinear wave mixing effectively in practical applications, the combination of the two nonlinear waves must be analysed with variation conditions.

In this section, we first study the sufficient conditions of two wave interactions to generate a third wave by applying the third order material constants to specific cases. Next, to predict the various interactions, Monte Carlo is used to estimate the material constants. The simulation would be benefit for the further set up nonlinear wave mixing study.

4.1.1 The five constants of elastic nonlinearity

When an acoustic wave propagates through an elastic material, the wave motion can be described by the displacement of a small cube. Their propagation in the medium is the result of a disturbing force from a compression wave. The equation of motion can be expressed in the following:

$$\rho \frac{\partial^2 u_i}{\partial t^2} = \frac{\partial \sigma_{ik}}{\partial x_k} \tag{4.1}$$

$$\rho \frac{\partial^2 u_i}{\partial t^2} - \frac{\partial u_i}{\partial x_k^2} - (\lambda + \mu) \frac{\partial^2 u_k}{\partial x_k \partial x_i} = F_i \ , \tag{4.2}$$

where u is a displacement vector, λ and μ are Lamè parameters and σ_{ik} is stress tensor. After the stress tensor is substituted in (4.1), the equation of motion is second order (4.2). Korneev and Demčenko, (2014) described the stress tensor (F_i) using Equation (4.3).

$$F_i = C_1 \left[\frac{\partial^2 u_s}{\partial x_k^2} \frac{\partial u_s}{\partial x_i} + \frac{\partial^2 u_s}{\partial x_k^2} \frac{\partial u_i}{\partial x_s} + 2 \frac{\partial^2 u_i}{\partial x_s \partial x_k} \frac{\partial u_s}{\partial x_k} \right]$$

$$+ C_2 \left[\frac{\partial^2 u_s}{\partial x_i \partial x_k} \frac{\partial u_s}{\partial x_k} + \frac{\partial^2 u_k}{\partial x_s \partial x_k} \frac{\partial u_i}{\partial x_s} \right] + C_3 \frac{\partial^2 u_i}{\partial x_k^2} \frac{\partial u_s}{\partial x_s} \qquad (4.3)$$

$$+ C_4 \left[\frac{\partial^2 u_k}{\partial x_s \partial x_k} \frac{\partial u_s}{\partial x_i} + \frac{\partial^2 u_k}{\partial x_i \partial x_k} \frac{\partial u_i}{\partial x_s} \right] + C_5 \frac{\partial^2 u_k}{\partial x_i \partial x_k} \frac{\partial u_s}{\partial x_s}$$

Constants A, B and C, introduced by Landau and Lifshitz, are related to the parameters above by:

$$\mathbf{C_1 = \mu + \frac{A}{4}, \; C_2 = \lambda + \mu + \frac{A}{4} + B, C_3 = \frac{A}{4} + B, C_4 = B + 2C,} \qquad (4.4)$$

$$\mathbf{C_5 = \lambda + B}$$

The constants of Murnagham and those of Landau are related by the following;

$$\mathbf{l = B + A, \qquad A = n} \qquad (4.5)$$

$$\mathbf{m = \frac{A}{2} + B, \qquad B = m - \frac{n}{2}}$$

$$\mathbf{n = A, \qquad C = l - m + \frac{n}{2}}$$

where l, m, n are nonlinear elastic constants of the third order proposed by Murnagham.

4.1.2 Nonlinear interaction of elastic waves

When two elastic waves, with frequencies ω_1 and ω_2, propagate in a solid and interact with each other producing a third wave, this is called wave-mixing. The interaction produces a third wave with frequency ω_3 given by the sum or difference of frequencies. The conditions for such a resonant interaction are:

$$\omega_3 = \omega_1 \pm \omega_2 \qquad (4.6)$$

$$k_3 = k_1 \pm k_2 \qquad (4.7)$$

$$\mathbf{k = \frac{\omega}{c}} \qquad (4.8)$$

Equations (4.6) and (4.7) show the combination of frequencies and wave directions. The + sign relates to the case of the summed resonant frequency and the − sign relates to the case of the difference resonant frequency. Therefore, Equation (4.6) describes the frequencies of the scattered wave and Equation (4.7) describes its direction of propagation. When considering the wave propagation in a solid medium, a variety of different resonance interactions are possible because of the existence of two velocities. In order to have the resonance conditions, the interaction angle (α), scattering angle (ψ) and amplitude coefficient (w) need for calculation and implementation the equation drescribed in section 2.4.1 .

4.2 Materials and Method

In this section we discuss how the ten cases for two wave interactions were implemented using Equations (2.21, 2.22, 2.23 and 2.24), as summarised in Table 2-1. The interactions between the shear and longitudinal waves produced a resultant wave whose frequency depended on the frequencies of the interacting waves, for example $L(\omega_1) + L(\omega_2) \rightarrow L(\omega_1 - \omega_2)$, where the interaction produced a resultant wave with frequency given by the difference of the two interacting wave frequencies. The MATLAB program was used to implement the equations with the material constants. The first step in the programming process was to define the material parameters λ, μ, l, m, n, ρ. In order to define the *dmin* and *dmax* values, the value of γ was calculated using Equation (2.23). The values of the frequency ratios *dmin* and *dmax* set the range within which a resonant interaction occurs between the two waves. Their values for each interaction case depend on the value of γ used in the equations in column 3 and 4 of Table 2-1. Next, the longitudinal and shear velocities (c_1 and c_2) were calculated by Equation (2.22). Then the interaction angle (α) was calculated by substitution of γ, *dmin*, and *dmax* in Equation (2.24). The interaction angle then allows us to find the scattering angle (ψ) by inserting the values for c_1, c_2, α, *dmin* and *dmax* in Equation (2.21). To determine the amplitude coefficient (*w*), the parameter D_L needs to be calculated from Equation (2.26). After that, the values of the parameters D_L, γ, α, *dmin*, *dmax* and *m* were substiuted in Equation (2.25) to find the amplitude coefficient. Finally, the interaction angle (α), scattering angle (ψ) and amplitude coefficient (*w*) were calculated with an expression as described in Table 2-1. In this study, the general wave interaction was considered, and then applied to PVC by substituting the material constants specific to PVC as given in Table 2-2.

The implemented equations vary depending on the details of the interaction, as shown in Table 2-1. For example, in interaction case#5, the *dmin* value is zero and *dmax* is equal $2\gamma/(1+\gamma)$. The interaction angle (α) was calculated based on $\gamma - d/2 \times ((1/\gamma) - \gamma)$ and a material constant of Murnagham (*m*) was used to calculate the amplitude coefficient (*w*). Finlly the interaction angle (α), scattering angle (ψ) and amplitude coefficient (*w*) were plotted versus the frequency ratio (*d*) for values between *dmin* and *dmax*.

In order to calculate the uncertainty associated with the wave interaction in a material, the Monte Carlo method was applied to the simulation where the material properties were assumed to follow the normal distribution. The Monte Carlo method is a mathematical tool that propagates uncertainty associated with the input. The input uncertainty is modelled according to a specific distribution such as normal, log, uniform etc. Of order 1000 random

draws from the input distributions produce an output distribution from which we extract the uncertainties.

4.3 Numerical results

4.3.1 Interaction of wave in an elastic material

From Section 2.4 in Chapter 2, the ten cases of nonlinear interactions are implemented to calculate the interaction angle, scattering angle, and scattering coefficient for polyvinyl chloride (PVC) with having a set of analysis parameters as follows: $\lambda=3.64$ GPa, $\mu = 1.83$ GPa, $l = 33.43$ GPa, $m = 20.88$ GPa, $n = -15.86$ GPa, and $\rho = 1350 \text{ kg}/m^3$. Those are the third-order elastic constants which have been found in (Mohabuth *et al.*, 2019), Demčenko, Koissin and Korneev, 2014a, Taylor and Rollins, 1964). Amplitude coefficients w (red), interaction angle α (black) and scattering angle ψ (blue) for all possible ten interactions cases from Table 2-1 are shown in Figure 4-1-10 as functions of the frequency ratio (d).
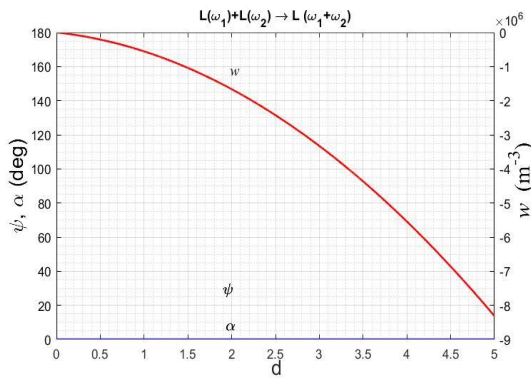
Figure 4-1: Interaction case #1

$$L(\omega_1) + L(\omega_2) \rightarrow L(\omega_1 + \omega_2)$$
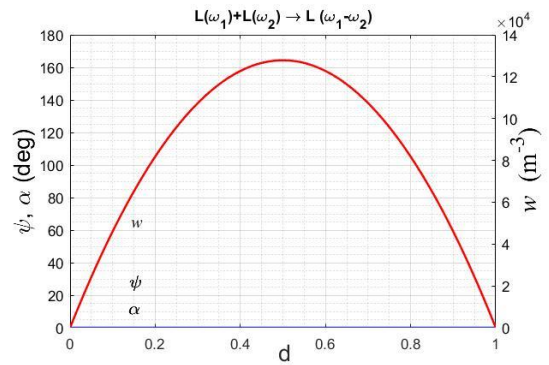
Figure 4-2: Interaction case #2

$$L(\omega_1) + L(\omega_2) \rightarrow L(\omega_1 - \omega_2)$$
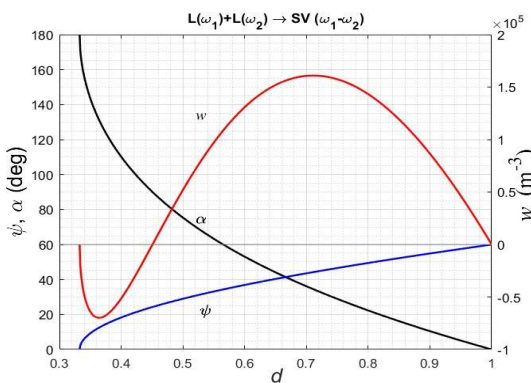
Figure 4-3: Interaction case #3
$$L(\omega_1) + L(\omega_2) \rightarrow SV(\omega_1 - \omega_2)$$
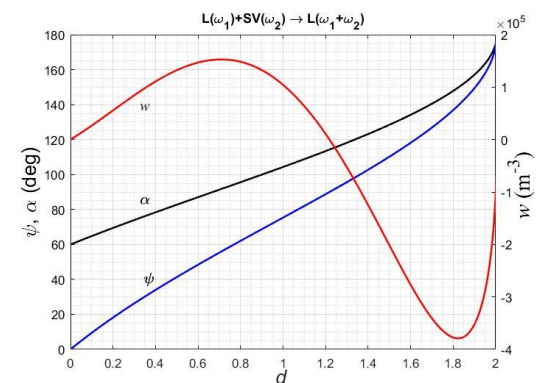
Figure 4-4: Interaction case #4
$$L(\omega_1) + SV(\omega_2) \rightarrow L(\omega_1 + \omega_2)$$
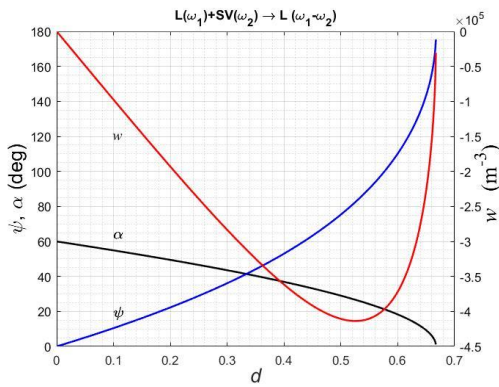
Figure 4-5: Interaction case #5

$$L(\omega_1) + SV(\omega_2) \to L(\omega_1 - \omega_2)$$
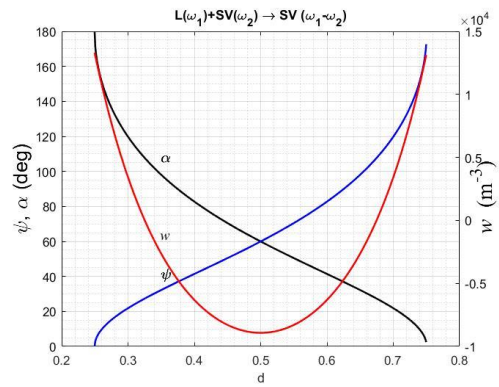
Figure 4-6: Interaction case #6

$$L(\omega_1) + SV(\omega_2) \to SV(\omega_1 - \omega_2)$$
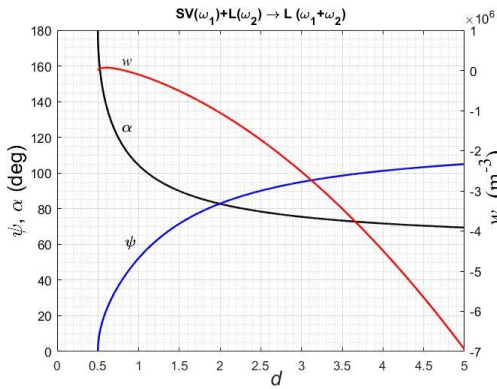
Figure 4-7: Interaction case #7

$$SV(\omega_1) + L(\omega_2) \to L(\omega_1 + \omega_2)$$
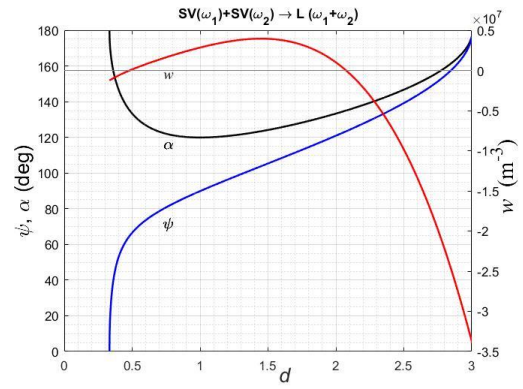
Figure 4-8: Interaction case #8

$$SV(\omega_1) + SV(\omega_2) \to L(\omega_1 + \omega_2)$$
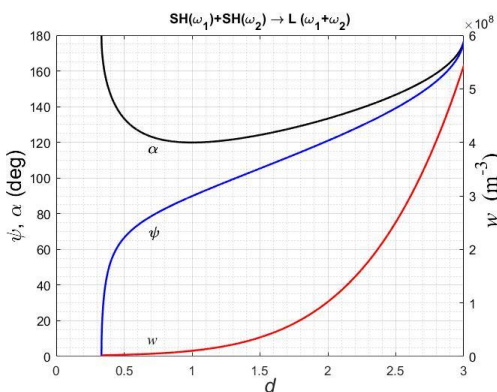
Figure 4-9: Interaction case #9

$$SH(\omega_1) + SH(\omega_2) \to L(\omega_1 + \omega_2)$$
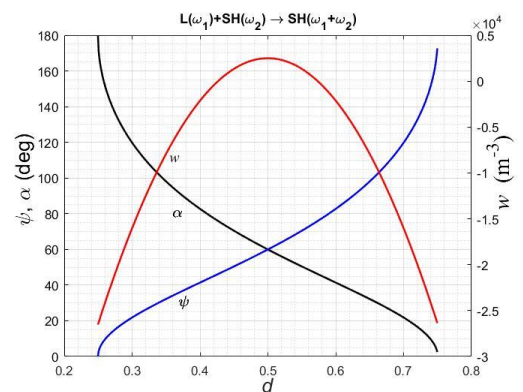
Figure 4-10: Interaction case #10

$$L(\omega_1) + SH(\omega_2) \to SH(\omega_1 + \omega_2)$$

All the simulation results are shown above. The results for each case are similar to those found in the previous study (Korneev and Demčenko, 2014; Korneev, 1998). The results of case#1 and case#2 (Figure 4-1,2) show that the interaction and scattering angles are zero. Only the amplitude of the mixed wave resulting from the two collinear waves $L(\omega_1)$ and $L(\omega_2)$ is visible in these plots. Figure 4-1 shows that the resonance range of amplitude coefficients is in the range 0 to 5 and the amplitude coefficients are negative. The result of this interaction is a summing frequency $(\omega_1 + \omega_2)$. The amplitude coefficients for the simulation of two collinear waves are related to $2m + l$, the constants of Murnagham. While case#2 (Figure 4-2) has a positive amplitude coefficient value with a frequency ratio in the range 0 to 1, the combination of interaction is a difference frequency $(\omega_1 - \omega_2)$ of original frequencies. This interaction case is also related to the third order elastic constants $2m + l$. Figure 4-3 (case#3) shows the shear wave with difference frequency from two longitudinal waves where the resonance condition varies in a range between 0.3 to 1 of the frequency ratio. The scattering angle takes on values from 0 to 60° while the interaction angle ranges from 0 to 180°. When the interaction angle is equal to the scattering angle, the amplitude coefficient is near a maximum peak. In this case the scattering angles are related to the λ and μ constants. Figure 4-4 shows the result of longitudinal wave interact with shear wave $L(\omega_1) + SV(\omega_2) \rightarrow L(\omega_1 + \omega_2)$ allowed at frequency ratio 0 to 2. Their condition starts with interaction and scattering angles equal to 60° and 0° respectively. A frequency-ratio value of 1.2 causes the interaction coefficient to be zero. This interaction case is reciprocal to interaction case#7 $SV(\omega_1) + L(\omega_2) \rightarrow L(\omega_1 + \omega_2)$ as shown in Figure 4-7 with the same interaction result. Interaction coefficients of both cases are related to m, λ and μ material constants but in case#7 the coefficient value is negative while in case#4 it can be positive or negative. Figure 4-5 and Figure 4-6 show the interaction result obtained from the same input combination wave ($L(\omega_1) + SV(\omega_2)$) but give the longitudinal wave for interaction case#5 and shear wave for case#6. For case#5, the interaction coefficient varied in narrow frequency-ratio range of 0 to 0.7 with negative value of coefficients. However, the frequency-ratio values cause two zero points for the interaction coefficients for case#6. Case# 8 and 9 interactions involved shear horizontal and shear vertical waves and have more complicated dependence on constants m and n. Finally, the remaining interaction (Figure 4-10), is one in which a longitudinal wave mixes with a shear horizontal wave. The variation of interaction and scattering angles of case#10 were the same pattern as the interaction case#6, but the interaction coefficient is a mirror image.

4.3.2 Interaction of wave in aging polymer and hydrogel

Regarding the previous ten wave interaction cases, we can predict the combination of two wave interactions which is beneficial to various applications. For example, in this study, the two wave interactions in polymer and hydrogel material are considered for observing physical aging behavior and microparticle deflection in the hydrogel. The important factors to be considered are the range of interaction angle, the ratio of frequencies, and the amplitude of the interaction coefficient. For instance, in the case of physical aging in polymer, the shear and longitudinal wave interaction are chosen, because the different wave modes are easy to differentiate during setup and their interaction angle is about 90°. Then the interaction case should be case#7 $SV(\omega_1) + L(\omega_2) \rightarrow L(\omega_1 + \omega_2)$. Whereas, we should use the collinear interaction for hydrogel material, as it has low ultrasonic wave velocities and the interaction result is sum frequencies. The case#1 interaction is possible $L(\omega_1) + L(\omega_2) \rightarrow L(\omega_1 + \omega_2)$. The nonlinear wave amplitude coefficient of both cases is shown in following:

$$w(case\#1) = D_L \frac{1+d}{2} (4C_1 + 2C_2 + 2C_{3+}C_4 + C_5) \tag{4.9}$$

$$\approx D_L(1+d)(2m+l)$$

$$w(case\#7) = \frac{D_L}{2\gamma^3} \frac{\sin\alpha}{1+d} (C_1(3d\gamma + 2q) + C_2q + C_3(d\gamma + q) + d\gamma C_5) \tag{4.10}$$

$$\approx \frac{D_L}{\gamma^3} \frac{\sin\alpha}{1-d} (d\gamma + q)m$$

$$q = \cos\alpha (2d\gamma \cos\alpha + 1 + 2\gamma^2 d^2) \tag{4.11}$$

$$D_L = \frac{d}{4\pi(\lambda + 2\mu)} \left(\frac{\omega_1}{v_l}\right)^3 \tag{4.12}$$

$$d = \frac{\omega_1}{\omega_2} \quad \text{and } \gamma = \sqrt{\frac{\mu}{\lambda + 2\mu}} \tag{4.13}$$
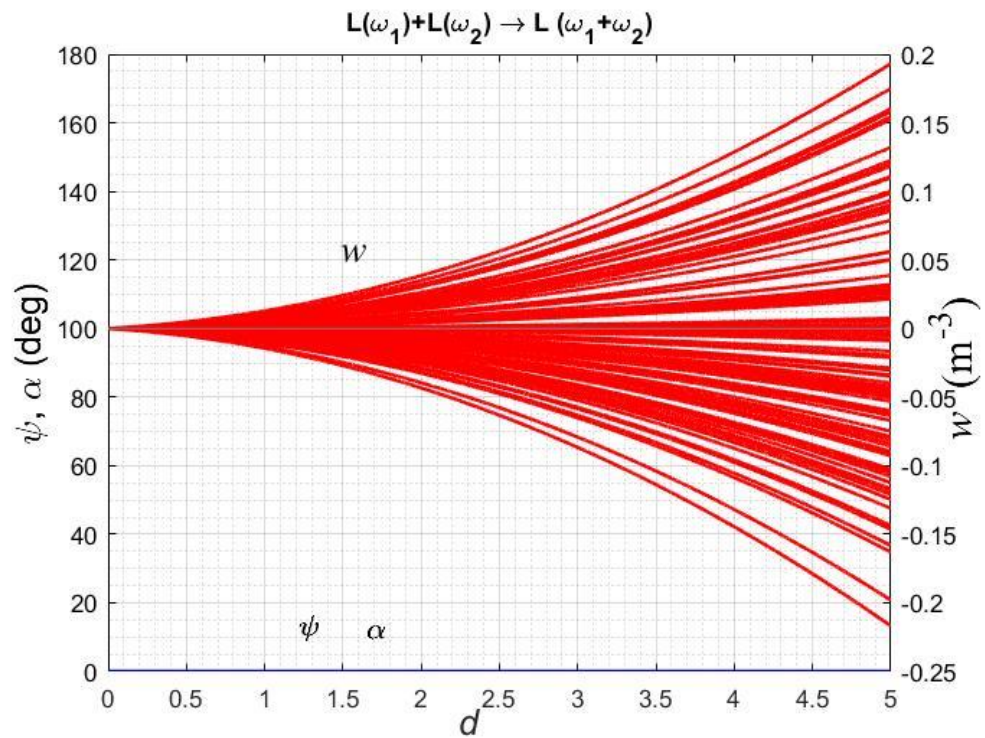
Figure 4-11: The amplitude of the collinear wave resulting from the interaction in soft solid. When two longitudinal waves are applied to hydrogel material, their propagation is combined then travels through the specimen.
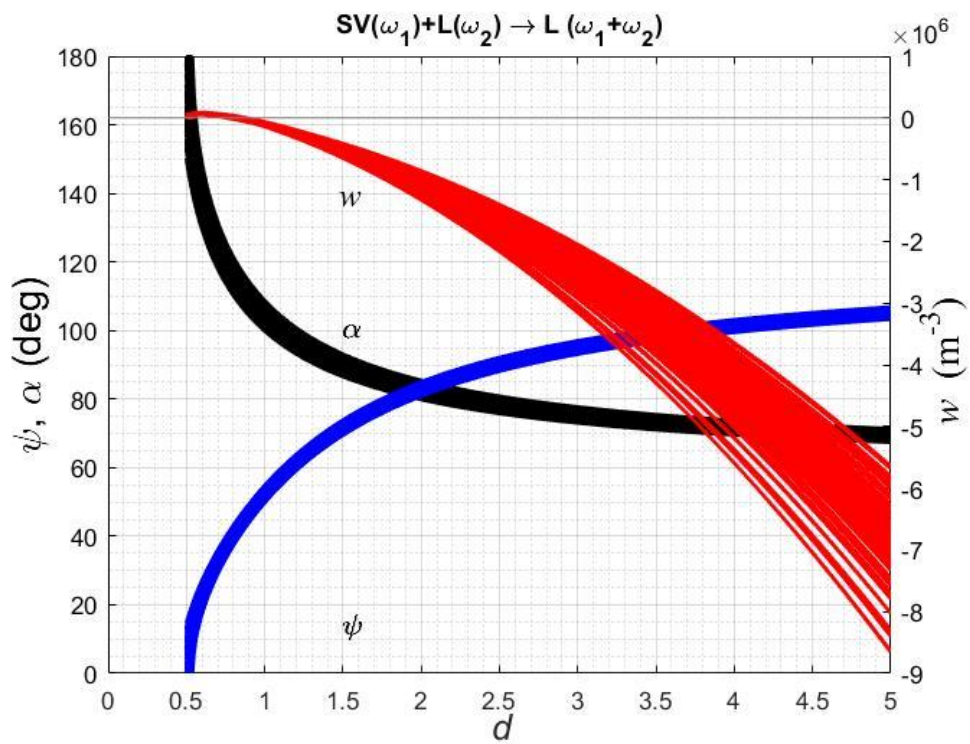
Figure 4-12: Noncollinear wave interaction between shear and longitudinal waves. The calculation used the third-order material constant (m) as estimated by Monte Carlo.

Figure 4-11 shows numerical results for case#1 ultrasonic wave interaction, as implemented via MATLAB. The amplitude coefficient of two collinear waves interacting to produce a third wave that propagates in a soft material, indicating that the amplitude varies with frequency ratio. It can be seen that both interaction angle (α), scattering angle (ψ) are zero, indicating the collinear nature of the wave interaction. The results show an exponential correlation between the frequency ratio and the amplitude coefficient. The calculations of the wave combination in case#1 are shown for the agar material properties listed in Table 2-2. This calculation is based on the configuration arrangement (see Chapter 3) which uses the immersion ultrasonic measurement method. These calculations use the Monte Carlo method to randomly sample the constants, such as m and l, with defined errors 5%, over 1000 iterations. The nonlinear amplitude coefficient varies from 0.2 to - 0.2 with units of m^{-3}, for the frequency ratio in the range $0 - 5$. The results show how the variation of material constants affected the amplitude coefficients. Greater variation is seen with an increased frequency ratio.

Figure 4-12 shows the numerical result for wave interaction case#7 implemented for PVC material with Monte Carlo random estimation of the material constants. The effect of variation of the material properties causes the change of interaction and scattering angles when two waves interacted together in PVC. The distributions of the interaction and scattering angles are equivalent and were quite narrow over the full range of d as can seen in black and blue graphs in Figure 4-12. Whereas the distribution for the amplitude coefficient w (red graph) is wider for large values of the frequency ratio d. That mean that uncertainty in the material properties leads to greater deviation of the amplitude coefficient, which varies between -5.5 to -9 in units of m^{-3}. Clearly, the variation of material properties would affect the amplitude coefficient ins both case of experiments at high values of frequency ratio. We assumed a uniform distribution for the random sampling of the third order constants μ , λ , m with defined errors of 10%, 10% and 5% respectively.

The variation of amplitude coefficient, interaction angle and scattering angle were affected by the uncertainty of material properties. This propagation of uncertainties is simulated using Monte Carlo method as shown by Figure 4-11 and Figure 4-12. Clearly, the findings indicate that when the material properties have a variation, the resulting amplitude of two wave interactions exhibit larger fluctuations at the large value of frequency ratio.

4.4 Discussion and conclusions

This study implemented the nonlinear wave interaction in solid materials. Ten wave interaction cases proposed by a previous study were applied for the calculation of amplitude coefficients, interaction and scattering angles. The calculation results agree with the study of V.A. Korneev which listed the ten possible interaction cases. Interaction case# 1-2 show collinear interactions while the remaining eight cases are all non-collinear wave interactions. Most of interaction cases are proportional to the third order material constant. However, some cases depend on different combinations. For example, the interaction of $L(\omega_1) + L(\omega_2) \rightarrow L(\omega_1 + \omega_2)$ is proportional to $2m + l$. Other case combinations relate to the third order constants μ, λ, m such that $SV(\omega_1) + L(\omega_2) \rightarrow L(\omega_1 + \omega_2)$, as shown in section 2.3.

Application using these nonlinear waves interaction cases have been discussed in various studies, for instance Jiao *et al.*, (2017) used $SV(\omega_1) + SV(\omega_2) \rightarrow L(\omega_1 + \omega_2)$ for fatigue crack detection which was an effective method for the quantitative measurement of fatigue cracks. Thanseer, Metya and Sagar, (2017); Escobar-Ruiz *et al.*, (2014) also used a combination of two shear waves for the evaluation material properties. In addition, the mixing $SV(\omega_1) + L(\omega_2) \rightarrow L(\omega_1 + \omega_2)$ case was used by Demčthe, Koissin and Korneev, (2014b), for the measurement of physical aging in polymers and also monitoring the epoxy cure processes. Moreover, collinear wave combinations are widely used for application in crack detection, degradation and deflection in material (Li *et al.*, 2016; Jingpin *et al.*, 2015; Jingpin Jiao *et al.*, 2014; Liu *et al.*, 2012). Those findings suggest that there are a few nonlinear wave interaction cases widely used for material characterisation such as interaction case#1, case#7 and case#8. For the case of collinear $L(\omega_1)$ *and* $L(\omega_2)$ interactions we do not need to arrange a specific angle for the incident wave interaction. In practice, the two different frequencies are applied to the same transmitter. With the shear $SV(\omega_1)$ and longitudinal $L(\omega_2)$ wave combination, we need to compute the incident angles: they need a large angle and a small angle for the interacting wave. However, its interaction only relates to one constant (*m*). For the two shear wave interaction case, $SV(\omega_1) + SV(\omega_2) \rightarrow L(\omega_1 + \omega_2)$, the different wave modes of the incident and interaction waves makes them easy to distinguish.

As discussed in previous sections, two combinations of incident wave are chosen to study the physical aging in polymer and hydrogel: interaction case#1, and case#7. Figure 4-11 shows analysis of longitudinal and longitudinal collinear wave interaction in a hydrogel material. These results can be explained by the fact that the amplitude coefficient of wave interaction varied widely for large values of the frequency ratio due to variations in the values of the third-order material constants, *m,* and *l*.

Their variation was in the range 0.2 to -0.2 (in dimension length 10^{-3}). These results implied that the $L(\omega_1)$ and $L(\omega_2)$ interaction mode would be able to detect the varied material constant at the upper frequency ratio. In addition, when comparison with practical experiment reported by Courtney *et al.*, (2008) are made the simulation results agree with the experiment of those studies when the variation amplitude of ultrasonic interaction signals was performed by using changing the excitation frequency in the region of 468-475 kHz with a fixed frequency with material. Their results were highly responsive in the upper frequency regions.

Figure 4-12 shows the calculation of the two wave interactions in a case $SV(\omega_1) +$ $L(\omega_2)$ with material constants for polyvinyl chloride (PVC). The effect of varying the material constants was simulated by Mote Carlo with a variation of 5 %. The results are shown for the interaction angle, scattering angle and amplitude of the scattering coefficient. The trend is similar to that of Section 6.3.1(case#7). In this case, the combination was proportional only to the material constant *m*. The trend shows the interaction angle (α) and scattering angle (ψ) varied in a narrow range over the whole range of simulation, similar to the result in case#7. While the variation of constant *m* affected the whole range of interaction and scattering angle, the amplitude coefficient (*w*) of wave interaction has a tendency to increase in variation. This deviation varied wildly with the upper frequency ratio. These findings imply that the amplitude coefficient of wave interaction would have a high sensitivity to change in material properties at the high frequency range.

Chapter 5   Nonlinear ultrasonic wave mixing to evaluate detection of particles

In this chapter, the advantages of the nonlinear wave mixing technique are applied to the measurement of small deflecting particles distributed in a hydrogel phantom. The collinear wave mixing is implemented using broadband ultrasonic transducers. The measurement system was setup using two ultrasonic transducers arranged in the through transmission mode. In order to avoid the acoustic impedance effect, this system was implemented in a water tank with a moving stage for supporting the phantom mold. The C-scan image was made using MATLAB programing for controlling and calculating nonlinear wave mixing energy. Different sizes of particles were used to generate a deflected signal from a phantom. The measurement results indicated that nonlinear wave mixing has a high resolution for detecting small particles as compared to the classical ultrasonic method. Last but not least, the position of the deflecting particles was determined from the collinear wave mixing, which can clearly locate the particles in the phantom.

5.1 Introduction

5.1.1 Tissue elasticity

Generally, a material elasticity explains its ability to return its original size and shape after excitation from an external force or stress. For tissue, elasticity is also the ability to deform and to recover its original shape when exposed to pressure. The characterisation of tissue elasticity has been studied for medical diagnosis (Huang *et al.*, 2019; Ben Amar, 2018; Washburn, Onishi and Wang, 2018;Wells and Liang, 2011). The elasticity modulus has a significant correlation with various diseases when the local tissue elasticity has been categorized and detected (Jorba *et al.*, 2019; Umemoto *et al.*, 2014). The basic principle of elastography involves observing the tissue response, in the form of deformation or shape change, to external forces. This deformation is also useful for ultrasonic imaging, which can provide the density distribution in the tissue, showing tissue nonhomogeneities. Through this method, the variation depends on compression force to drive the non-linearity in tissue elasticity. Much research has focused on this approach for tissue characterization of diseases rather than for the linear method. For instance, Krouskop *et al.,* (1998) evaluated the non-linearity of breast tissue elasticity in response to different values strain and investigated the strain distribution in their tissue. When abnormal tissue is diseased, it tends to be stiffer than in neighbouring areas. Linear methods are not as efficient at distinguishing stiffness between

normal and diseased tissue in some tumor cases. Sinkus *et al.* (2006) evaluated nonlinear parameters of tissue using ultrasound. Their evaluation was implemented on tissue mimicking phantom to determine the nonlinear parameters of the tissue by detecting the second harmonics present when nonlinearity occurs. However, this method relied on small applied strain values for the various tissue types, making it difficult to distinguish normal and diseased tissue.

5.1.2 Acoustic incident on a spherical object

To investigate the acoustic radiation force on a particle, we study the principle of acoustic scattering off of a spherical object. This interaction is modelled by a plane wave as evaluated by (Marston, 2007). Basically, the transducer generates the acoustic wave in the form of an acoustic beam which can applied in medical imaging, material characterization and particle manipulation. For example, the acoustic tweezer is based on an acoustic beam trapping a particle using a standing wave. Such a surface acoustic wave device is utilized as an acoustic actuator. The acoustic beam is coupled into a microchannel chip to generate an acoustic standing wave at a resonance frequency of the piezoelectric substrate. The standing wave intensity depends on the acoustic energy density for different driving voltage signals. This acoustic beam which appears in the inner microchannel promotes the streaming velocity of small beads and can manipulate them (Witte *et al.*, 2013). The properties of the beam are important to predict what happens when the acoustic wave is incident upon a sphere. The excitation of resonance will depend on the beam parameter such as radius of spherical particle (a), sound speed (c), wave vector (k), axial distance (z) and pressure amplitude (P_0). This scattering has been described in detail by (Marston, 2006). He derived the acoustic beam which excites a particle in an ideal fluid by using the Bessel beam principle. The acoustic beam pressure, based on the Bessel function, is given by $P_B(R,z) = P_0 \exp(iKz) J_0(\mu R)$ and $\mu = k \sin(\beta)$, when P_0 is the axial amplitude, z is the axial coordinate, $R = \sqrt{x^2 + y^2}$ is the transverse coordinate, J_0 is a Bessel function, $K = \sqrt{k^2 - \mu^2}$. Then, the acoustic pressure is calculated by the real part of $P_B(R,z)\exp(-i\omega t)$. The pressure ulcer can be modelled as a small sphere. Deep PUs, which occur under the skin are generated by a peak pressure of a local area and lead to deep tissue injury described in Section (1.1.3). The value of 4.3 kPa of tissue compression pressure is reported as the main reason for tissue injury and induces a tissue stiffness increase of 3.3 fold from normal values when compared to the surrounding tissue (Gefen *et al.*, 2005; Deprez *et al.*, 2011). In addition, the study also showed that the peak pressure area was located approximately 4 mm in the tissue layer under

the ischial tuberosites during wheelchair use (Mak, Zhang and Tam, 2010). Then a threshold pressure and peak pressure area would be a key factor for the early detection of pressure ulcers. Considering the peak pressure area, if it is assumed to be a small area less than 4 mm, it would be useful for early detection. The small object that occurrs in deep tissue causes a change of local tissue stiffness and results in different non-linearity of tissue properties, which would be characterised by nonlinear wave mixing. Collinear wave mixing is widely used to characterize damage in materials and structures. Here, we apply this to detect small defects based on the principle of acoustic scattering on a spherical object taking advantage of the properties of collinear wave mixing, including high sensitivity. This has been used to detect micro-cracks or degradation and small defects (Jingpin Jiao *et al.*, 2014). According to basic principles, collinear wave mixing techniques are based on the detection of the non-linearity of the material using the harmonic generation, which is correlated to the non-linearity of the material (Novak *et al.*, 2012; Liu *et al.*, 2012; Jingpin Jiao *et al.*, 2014; Li *et al.*, 2016). Therefore, the use of collinear wave mixing is promising to evaluate non-linearity in material and might also be applied for evaluating deep tissue injury in a small area. In the study described below, we are interested in the use of collinear wave mixing to detect the small spherical object in soft media which represents damaged tissue. Throughout this experiment, the collinear wave mixing system was used.

5.2 Material and Methods

5.2.1 Collinear ultrasonic wave mixing setup

In this experiment, non-linear collinear ultrasonic wave mixing, was used in ultrasonic through-transmission mode. Collinear ultrasonic wave mixing is based on two fundamental frequencies transmitted through the same transducer. The nonlinearity of the transducer results in the combination of the signals and the generation of a harmonic wave including the sum and difference frequencies to excite a sample (Figure 5-1). When these incident waves have interacted with nonlinearities of a sample, the response of the nonlinear signal appears in a term of the sum and difference of the exciting frequencies. The system of collinear ultrasonic wave mixing was described in Section 3.3. The measurement system is integrated with a moving stage, as shown in Figure 5-2 having X and Y-axis controllers. Their motion is programmed using MATLAB command passing through the motorized linear actuator (ZABER, T-LSR300B) with a high resolution of 0.496 μm/ step.

The measurement system consists of "sending" and "receiving" transducers. Both transducers are broadband piezoelectric transducers having a central frequency of 5 MHz

and 10 MHz for excitation (Tx) and receiver (Rx) (see Section 3.5). The driving frequencies have two fixed fundamental frequencies of 4.5 and 6.75MHz sent to the same transducer. The pumping frequencies were applied in 20 cycle tone bursts for producing a non-linear wave mixing frequency of 11.25 MHz. A function generator (Aim TTi, TG5011) was used to generate both frequencies using a special function to create and adjust the frequency (Waveform Manager Plus v4.0). For example, the expression to create a waveform is "sin $(((omg \times 1.5) - omg)/100) \times t^2 + (omg \times t)$", where omg $= 2\pi f$. This program containing this expression was uploaded via USB connection to the function generator.

The combination of frequencies (ω_1, ω_2) was produced at the transmitter and sent to the specimen. When two waves interacted at the lesion area, a nonlinear medium, the result was the production of a group of new frequency components. The frequency spectrum is shown in Figure 5-1(b) when two original frequencies ω_1 and ω_2 interacted with the material. Because of material nonlinearity, the wave can generate a to second harmonic or mix in sum and difference frequencies which can then be used for the evaluation and characterisation of material properties.

(a)

(b)
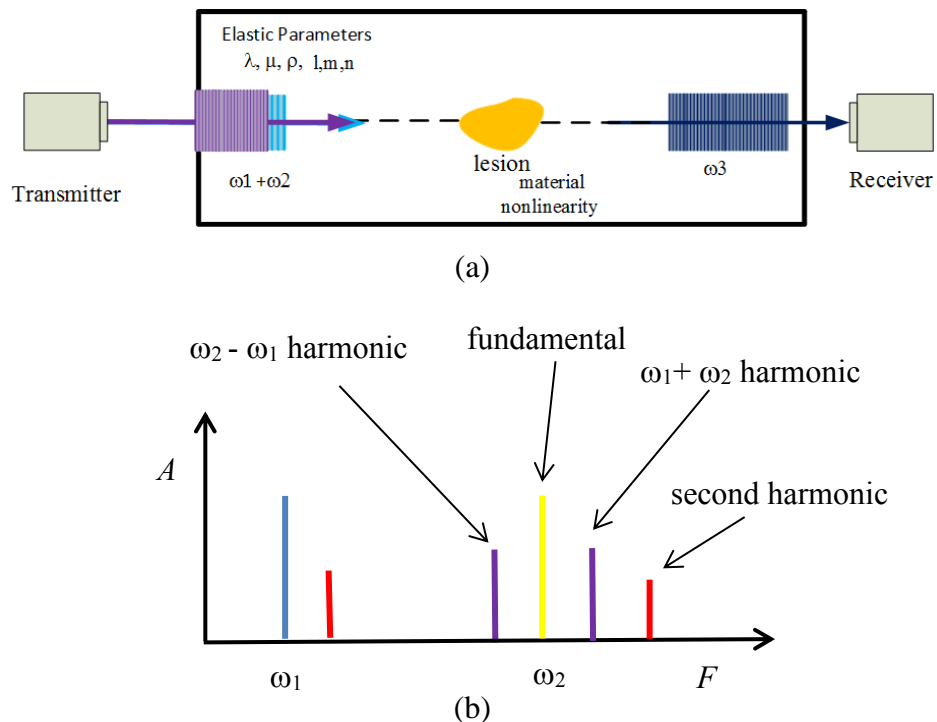
Figure 5-1: (a) A schematic diagram of the collinear measurement system. The wave mixing is generated when two different frequencies are sent to the same transmitter and the interaction between the nonlinearities of materials and the two incident waves generates sum and difference frequencies as shown in (b).
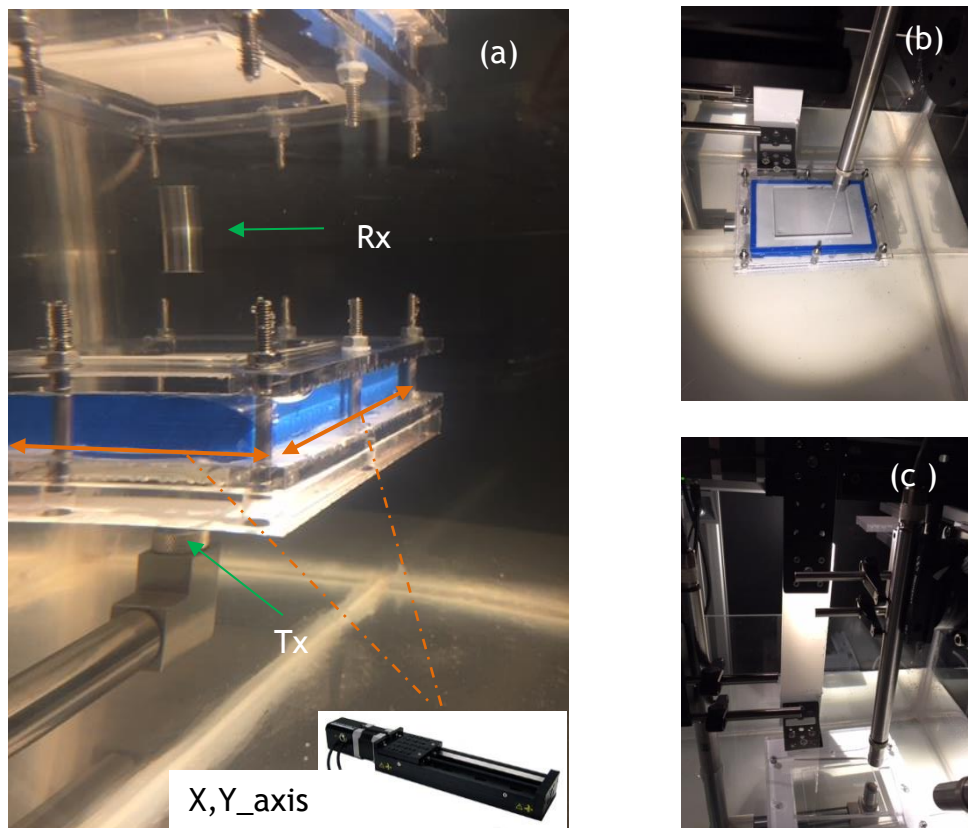
Figure 5-2: (a) The moving stage for supporting tissue phantom. Ultrasonic transmitter (Tx) is arranged on the opposite side of the receiver transducer (Rx) with a supporting stage in the middle of both transducers. The motorized linear actuators are used for driving in the Y_axis and X_ axis. The stage and transducers are immersed in the water tank. (b) The top view of moving stage. (c) The stage without specimen.

5.2.2 Tissue phantom and particle size preparation

A tissue phantom is a device used to mimic tissue properties. The relevant acoustic properties of mimicking phantom are the speed of sound (c), acoustic impedance (z), and acoustic attenuation (α), chosen to be similar to soft tissues. Examples of those properties were explained in Section 3.4. In this study we use NIPAM, which has the following advantages: 1) easy fabrication at room temperature, 2) it is a transparent material making it easy to avoid inducing an air bubble in the gel, and 3) the acoustic properties are the same as soft tissue (Sun *et al.*, 2015; Shieh *et al.*, 2014).

A phantom of 5×4×3 cm dimensions was designed with and without particles dispersed in the middle of the gel. We use four sizes (40 μm, 70 μm, 100 μm, 150 μm) of aluminium-coated solid barium titanate glass microspheres (BTGMS-Al-4.2, Cospheric) in the phantom. The particles were suspended in deionised water containing 0.1% Tween® 20. Tween® 20 is a nonionic detergent widely used in biochemical experiment. For this study, we used them to prevent the beads from sticking together and/or binding to the substrate surface. The beads in the phantom in this study mimics the pressure ulcer or lesion and

deflect the ultrasonic wave. Important examples of acoustic properties of some typical soft tissue are shown in Table 2.3. The NIPAM was prepared at room temperature in an acrylic mold covered on two sides by clear plastic sheets for transparency. In order to avoid leaks, the acrylic mold and covering sheets were sealed with silicon glue.

5.2.3 Experiment procedure

The collinear ultrasonic wave mixing was carried out by exciting the transmitter transducer with two fixed frequencies (f_1 = 4.5 MHz and f_2 = 6.75MHz). The two fixed frequencies with 20 cycle pulse from the function generator were sent to an RF amplifier in order to drive the transmitter. The driving frequencies f_1 and f_2 led to the generation of sideband frequencies at the sum and difference resonances of 11.25 MHz and 2.25MHz because of non-linear effects in the transducer and devices. In this experiment, the summed frequency was used for detection from the received signal because it has a stronger signal amplitude than the difference signal (see in Figure 5-7). First, the mixing signal was sent to samples with and without particles by using the receiver transducer arranged in the through transmission mode, and then the non-linarites of the sample modulate the mixing signal. In order to extract the non-linear information from the received signal, the raw signal combined by the two fundamental frequencies (see Figure 5-8) was filtered with a Kaiser window filter providing narrowband filtering and easy-to-change filtering parameters. After the filtering processes, only non-linear wave mixing at the summed frequency is present in the peak-to-peak amplitude. The energy from non-linear wave signals can be calculated using the peak-to-peak amplitude (Demčenko, Koissin and Korneev, 2014), and the variation of the energy amplitude relates to the non-linearity of the sample.

In order to evaluate the deflection from the sample, a C-scanning mode was performed at 0.25 mm steps in x and y-directions. The system set up described in section 5.2.1 was executed on the specimen with and without particles by C-scanning image. Not only the particle reflection was investigated by the gel, but the comparison of the linear and collinear ultrasonic measurement also was evaluated by using the same system setup.

5.3 Experimental results and discussion

5.3.1 NIPAM phantom properties investigation

The properties of the phantom were validated on a NIPAN phantom with dimensions 50×40×30 mm. The properties validated were the velocity, attenuation, and density of the NIPAN phantom. First, the velocity of sound in the phantom was measured
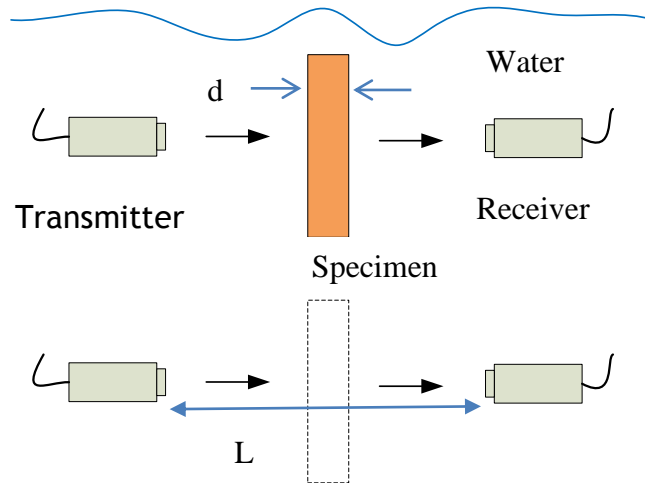
Figure 5-3: The phase velocities measurement system. Ultrasonic through transmission mode is applied to a specimen with *d* thickness and the distance between both transducers is *L* .

using through transmission methods for evaluation of the velocity of a longitudinal wave in the phantom as shown in Figure 5-3. This system of measurement is based on a phase-spectrum method. The velocity can be measured from the phase velocity data of the received ultrasonic signal at a frequency 5 MHz. An ultrasonic pulse was transmitted with and without the phantom to allow the determination of the phase velocity in the NIPAM phantom. The pulse spectra were caculated using the Fourier transform method, then the spectra were compared with and without the specimen inserted. The spectra was used to calculate the phase based on the Equation (2.8) described in Chapter 2. The calculation results were then ploted (see Figure 5-4). Then, the attenuation coefficients were measured using the same experimental setup. The attenuation coefficient was obtained from the different amplitude spectra of the transmitted pulse with and without specimens. The mehod to evaluate the phase velocity and attenuation coefficient is described by He and Zheng (2001).

Figure 5-4 illustrates the velocity of an ultrasonic wave in NIPAM gel when a 5 V (Peak-Peak) ultrasonic pulse was directly applied to a transmitter, then the propagated signal from the phantom is measured by the receiver based on the system measurement shown in Figure 5-3. A slight increase of phase velocity was observed in a water tank at room temperature (21 °C) assuming a water velocity of 1482.3 m/s (Zell *et al.*, 2007). An ultrasonic pulse propagated through the water as show in Figure 5-4 (a) in blue line while the red dash was the ultrasonic pulse propagating through a NIPAM specimen. Both pulse were used to determind the phase velocity of a pulse in a NIPAM specimen by using Equation (2.8). After calculation, the Figure 5-4 (b) shows the phase velocity curve when the ultrasonic pulse passes through the gel. From the graph, the phase velocity of sound in the NIPAM phantom was about 1547 m/s at a frequency of 5 MHz. These values are similar

to those of human muscle tissue as found in previous research (Culjat *et al.*, 2010), but higher by 0.5 %. However, comparison to other phantom materials shows this velocity is the same as in bovine serum albumin (BSA) and egg white (Shieh *et al.*, 2014). The NIPAM prepared in this experiment has densities in the range $1.057 - 1.12$ g/cm^3 as listed in Table 5-1. It could be used for mimicking muscle and possibly for representing breast tissue, which also may be beneficial for high intensity focused ultrasound (HIFU) for ablation.
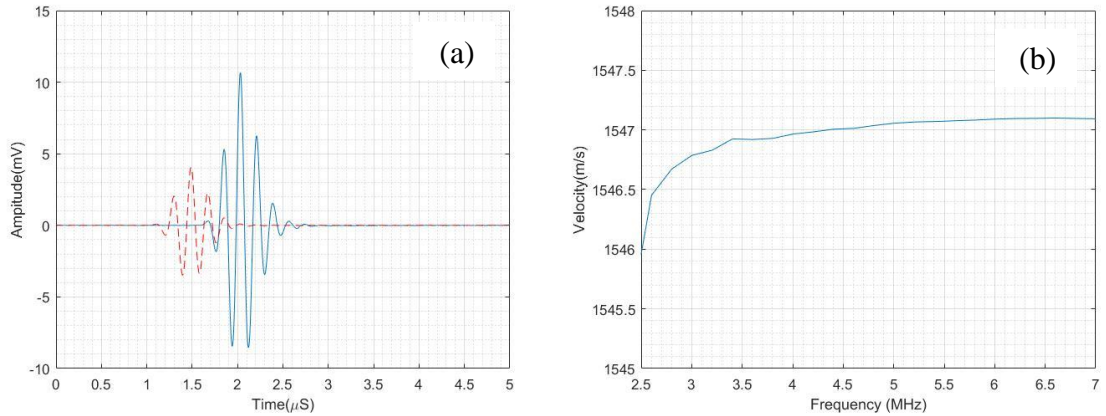
Figure 5-4: The phase velocity dependence on NIPAM when an ultrasonic pulse is dispersed the NIPAM phantom. The transmitted pulse propagates with specimen (red dot) and without specimen (blue line) and inserted show in (a). The mechanical property of the gel cause to change in the phase of the ultrasonic pulse, related to the velocity as calculated by Equation 2.8 (b).
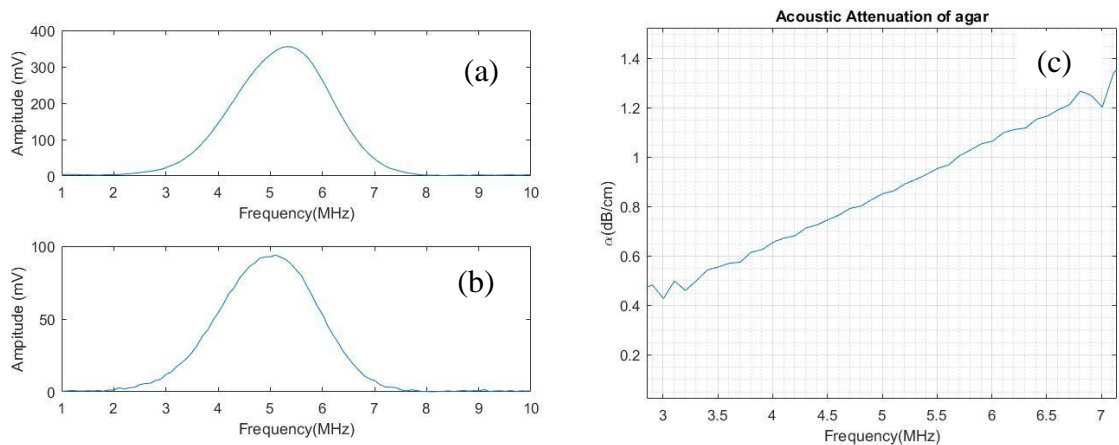
Figure 5-5: The amplitude spectrum for 5 MHz ultrasonic wave testing. The amplitude spectrum of an ultrasonic pulse when it travels through (a) the water media and then (b) when it is attenuated from propagation through the NIPAM phantom as well. The attenuated signal is used for calculation based on Equation 2.9 and 2.10, the result of which are shown in (c).

The attenuation coefficient of NIPAM was determined using the amplitude spectrum after Fourier transform of the signal, which consisted of through-phantom and reference signals. The intrinsic attenuation coefficient value at 5 MHz was about 0.8dB/cm as measured at 21 °C as shown in Figure 5-5. The result shows that their attenuation value is lower than the previous report about 1.9dB/cm at 5 MHz (Shieh *et al.*, 2014). They demonstrated the NIPAM to make tissue phantom for thermal ablation therapy by

ultrasound. The NIPAM phantom with a cloud point temperature have fabricated, the acoustic attenuation was about 0.54dB/cm MHz.

The phantom densities of many composite materials (see Section 3.4) can be determined based on Archimede's principle. Fifteen thousand millilitres of degassed water ($\rho_{wat} = 1000 \ kg/m^3$) were prepared in the eureka chamber at room temperature. Then, the phantom density was evaluated by finding the weight and volume of the sample floated in the chamber. Table 5-1 shows the summary of results for the velocity, attenuation and density values of the phantom. In order to simulate a defect in the phantom, different sizes of particles were arranged in the phantom during the phantom preparation processes. The particles are distributed in the middle of a 50×40×30 mm dimension mold (Figure 5-6).

The fabricated phantom described above is a reusable hydrogel phantom which was designed for the deflection of ultrasonic signal using dispersed particles that represent defects.

Table 5-1: The density, velocity of NIPAM phantoms used for this experiment are summarised. Particle are embedded in the phantom and detected by signal deflection.

Phantom	Density (g/cm³)	Velocity (m/s)	Beads (µm)
Ph01	1.120	1547	-
Ph02	1.067	1512	3000
Ph03	1.057	1515	100
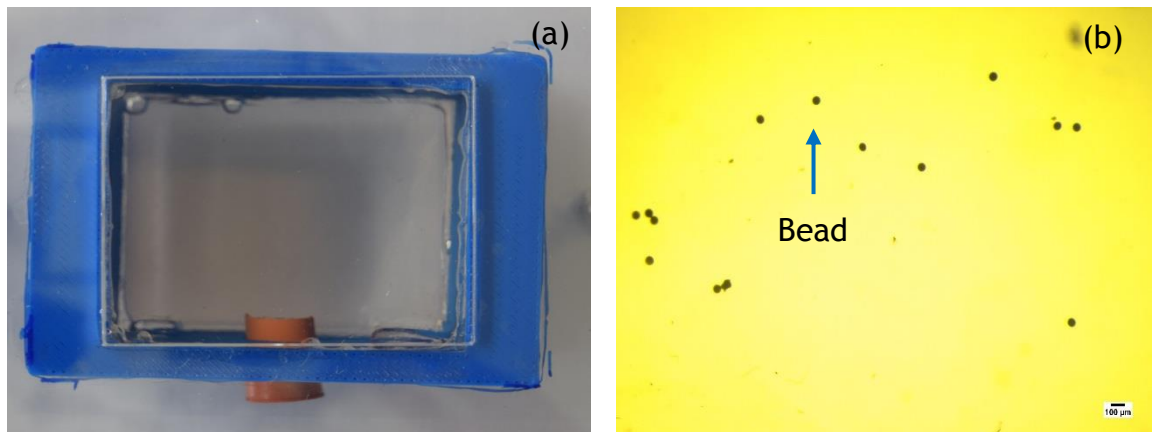
Figure 5-6: (a) The NIPAM tissue phantom in a 50×40×30 mm dimension mold. (b) The dispersed particles in the NIPAM gel can be seen when 10x magnification is used and generate reflected signals when they interact with the wave mixing signal.

This type of phantom is based on NIPAM, and some chemicals which make the phantom transparent; one can observe the particles in the gel. In addition, phantom transparency allows the identification and removal of bubbles in the gel.

5.3.2 Response in frequency and time domain

In these experiments, two driving frequencies were used for exciting an ultrasonic transducer with a fixed frequency. The driving frequencies ω_1, ω_2 were fixed at 4.5 MHz
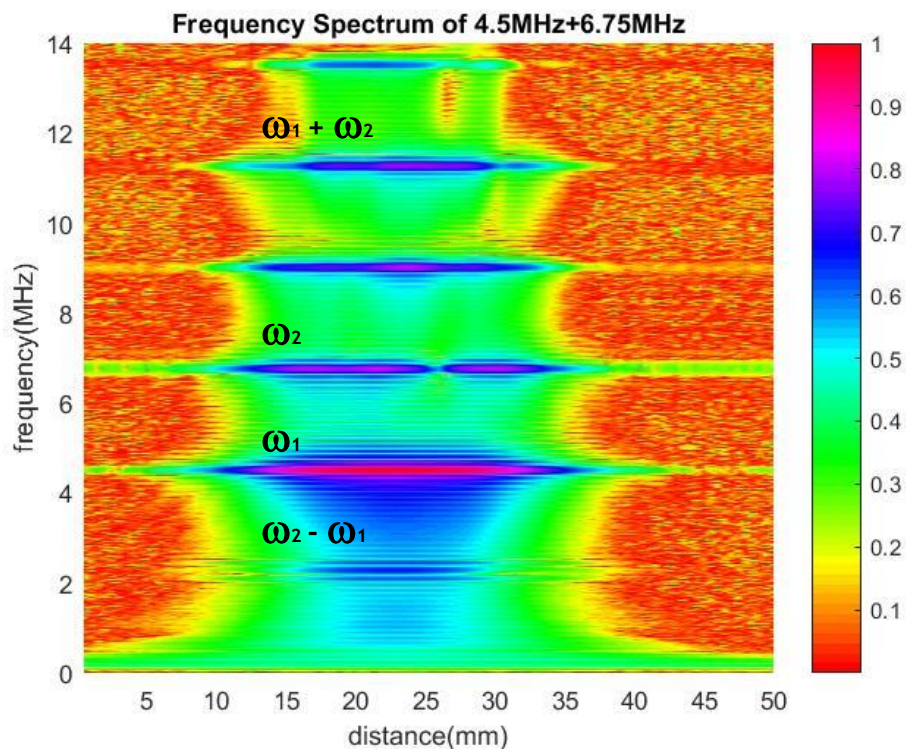
Figure 5-7: The frequency spectrum of two fixed driving frequencies (ω_1, ω_2) can generate sidebands of sum $(\omega_1 + \omega_2)$ and difference $(\omega_2 - \omega_1)$ frequency. The sum frequency is used for this experiment.

and 6.75MHz, respectively. The amplitude of frequency spectrum with sidebands at the sum and difference frequency were detected by the receiver transduce and are shown in Figure 5-7. The sum of collinear frequencies is11.25 MHz.

The combination of the raw signal is shown in Figure 5-8 in the time domain. The interaction begins with two fundamental frequencies generated together by a function generator, then amplified and passed through the same transducer. According to the nonlinearity of the equipment, such as the amplifier and transducer, the nonlinearity of the system might affect the mixing frequencies in the same way as the material nonlinearity.

The two different fundamental frequencies of the ultrasonic wave reinforce the amplitude when they mix. Figure 5-8 (a) shows that two frequencies with a different phase

are combined at the transducer. When ten cycles of both frequencies have interacted, the combined response of each cycle is added, leading to an increase in the peak amplitude. However, the changing amplitude is dependent on the phase difference of the two waves. The consequence of the combination is the generation of a sideband frequency as show in
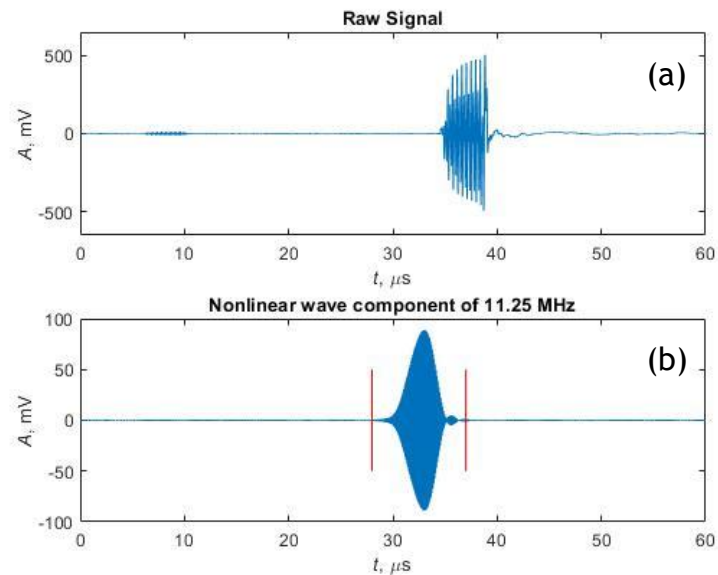
Figure 5-8: Collinear ultrasonic wave mixing signal with the raw signal as picked up by the receiver transducer. When two different fundamental frequencies are combined, the mixed signal is shown in (a). In order to remove unwanted sideband frequencies, the combined signal was filtered by a bandpass filter, resulting in the signal shown in (b).

frequency spectrum (Figure 5-7). The receiver picks up the combination frequencies as the raw signal show in Figure 5-8(a). The combination consists of the summed fundamental frequency $(\omega_1 + \omega_2)$ and the difference fundamental frequency $(\omega_2 - \omega_1)$. In this study, the summed frequency is used because it is stronger than the difference frequency. The summed frequency (11.25 MHz) was analysed after filtering the raw signal with a bandpass filter (Figure 5-8 (b)).

5.3.3 Distance-amplitude correlation of particles

The location of the particles significantly affects the amplitude of the received signal when the radiating beam from transmitter interacted with the particles. The amplitude of the wave scattered off of the particles varies with distance along z-axis. In a typical far-field distribution the field intensity drops by 6 dB every twice the distance from the transducer due to beam spread alone. With particles and phantom present, additional attenuation caused further changes in the amplitude. Not only does the depth of the beam from the transducer have an effect on the received signal amplitude, but so does the particle size, which affects the scattering and causes changes in the amplitude. So in this experiment, the amplitude

(peak-to-peak) received from the reference phantom was measured versus depth of the transducer. In addition, particle size was varied in order to determine the effect on the received signal amplitude.

Figure 5-9 shows that the depth of the ultrasonic beam from the transducer affects the received signal when the collinear wave mixing signal was applied to the NIPAM phantom with particles. The 4.5 MHz and 6.75MHz ultrasonic waves with 10 cycle burst were mixed at the same transducer. In order to have the far-field position of the ultrasonic beam interacted with the particle strongly, the position of Tx transducer was about 22 mm based on the far-field distribution curve shown in Figure 5-9(b). The ultrasonic field propagates from the transmitter at 6.75MHz as shown in Figure 5-10. Along the z-axis, as a function of distance from the transmitter, we find a distribution of peaks. The location of the transmitter was chosen so that the scattering off of the particle occurs at a peak in the far field distribution.
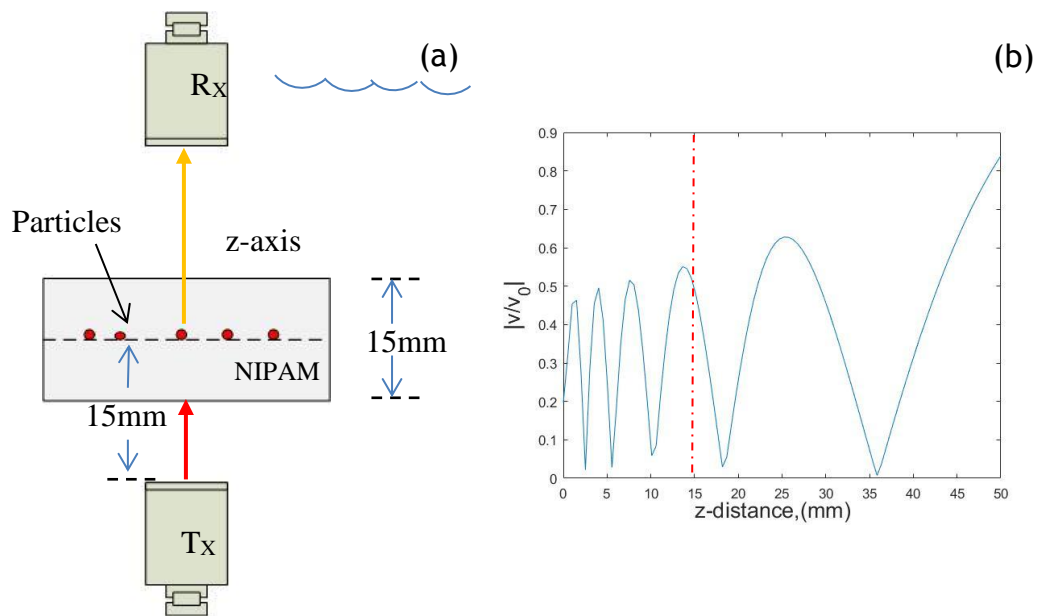
Figure 5-9: (a) The schematic diagram shows the arrangement for the through-transmission method used for determining the effect of the distance and particle size. The transmitter location depends on the pressure distribution curve. Tx is located at a high-pressure peak with a fixed distance of 15 mm from the surface of the phantom. Panel (b) shows the magnitude of the on-axis velocity of the 10 MHz, 9.524mm diameter transducer as a function of the depth in the water-NIPAM phantom gel.
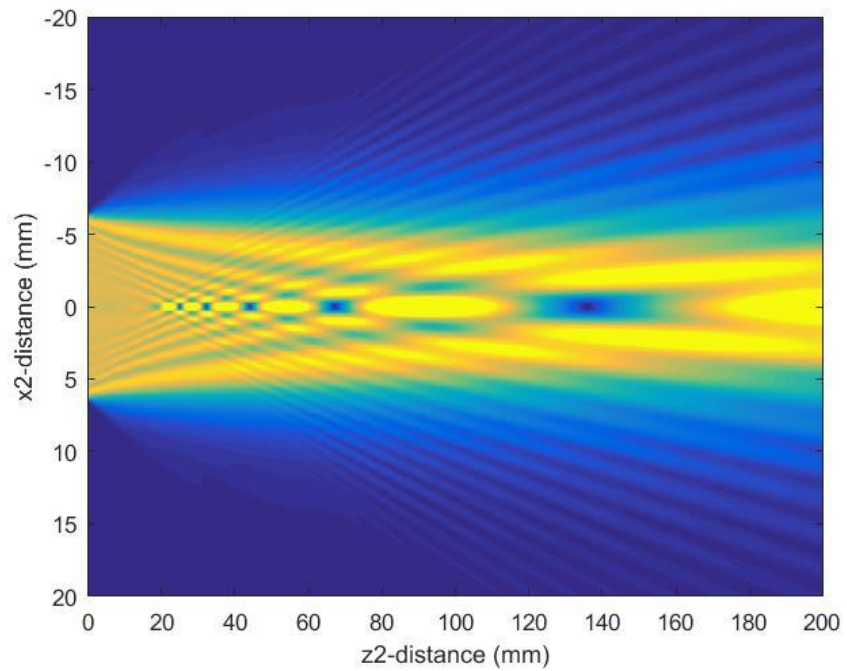
Figure 5-10: The 2D image of the near field distribution for a 10 MHz, 9.524mm diameter planar piston transducer generating into water.
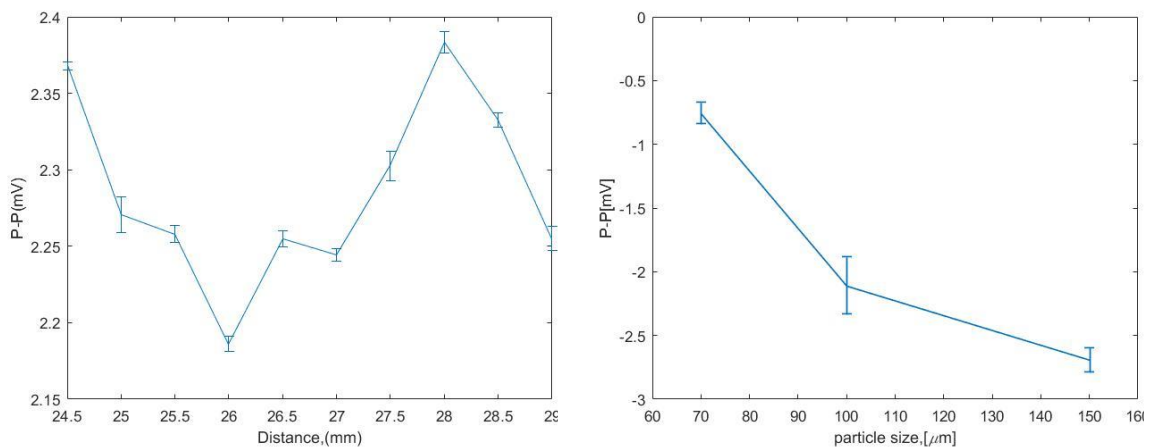
Figure 5-11: The effect of distance of a particle and particle size on the received signal amplitude after scattering off of the particle.

5.3.4 The deflection of particles

The deflection from beads distributed in NIPAM gel is investigated by a collinear signal. Ten cycles of two ultrasonic frequencies are applied to the phantom and the scattered wave is measured by x-y axis scanning. The experimental setup is shown in the schematic diagram of Figure 5-9(a), with more detail given in Section 5.2.1. In order to avoid impedance effects, the measurement was carried out in a water tank with a moving stage to

support the phantom mold. Four phantom specimens were created, each with different sizes of aluminum-coated solid barium titanate glass microspheres (BTGMS-Al-4.2, 30 -150 µm, Cospheric) in the gel. The particles are located in the middle of the phantom, whose thickness is 15 mm. The C-scan image is performed to detect a defect particle. The ultrasonic C-scan produces a two-dimension image because the ultrasonic transducer is moved along the X -Y axes over the specimen being inspected. The display shows the peak of signal response within a given time interval as a function of transducer position. The scanning step is performed with 60×60 steps and a resolution of 0.25 mm/step. The data acquisition automatically picks up each step and stores the measurement in the memory for later processing.

Figure 5-12 shows a C-scan image using a collinear ultrasonic signal when the initial signal was reflected from the particles. It is clearly seen that when the collinear wave produced by mixing interacts with particles, the result is a generated reflected signal of magnitude around 1.8 - 2.6 mV peak-peak (the blue dot). The polarity of the reflected signal was negative when the wave strikes a particle because of the increased attenuation due to the higher density of the microspheres as compared to the gel. When the material densities were high, there was increased reflection of the ultrasonic signal and therefore less transmission. This results in the received signal having a negative polarity, as shown in Figure 5-13. When the reflected signal was studied closely, and it was noted that there was a base signal level that corresponded to transmission through gel only. The transmitted signal decreases from this base signal level to a lower point when there scattering off a particle. That would be the result induced by the nonlinearity of the particles.
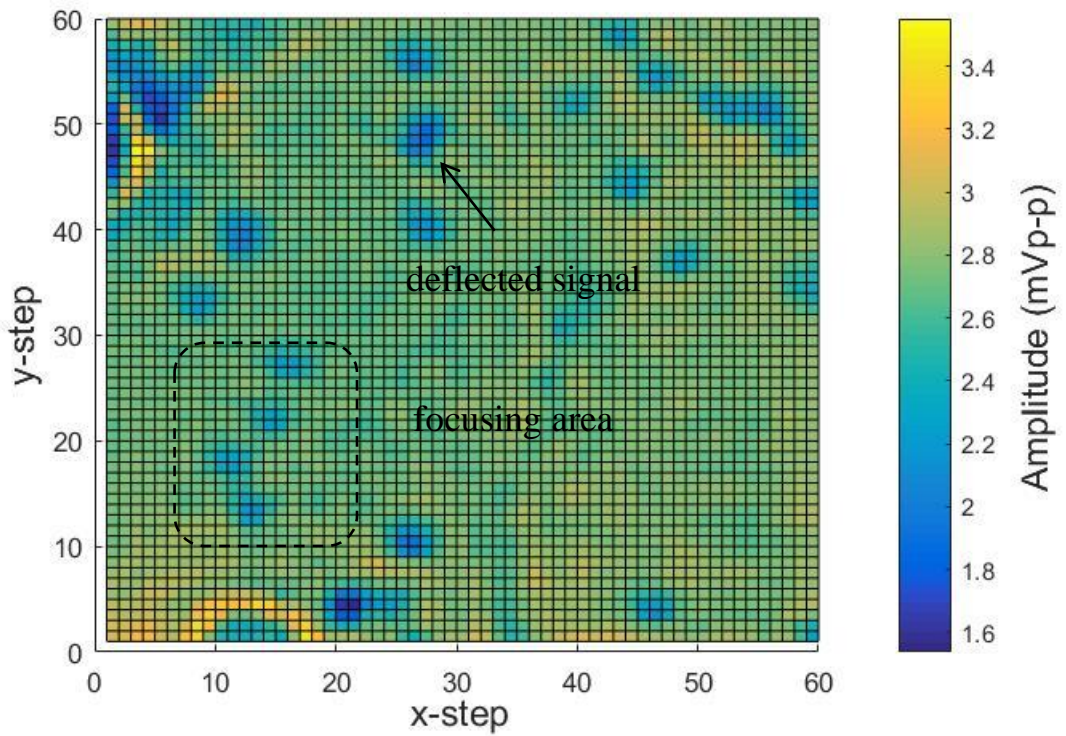
Figure 5-12: The nonlinear ultrasonic wave mixing method, C-scan, is performed on a NIPAM phantom with 150 μm particles distributed throughout the gel. The C-scan image is performed in the X_Y axes with 60 x 60 steps and 0.25mm resolution for each step. The blue circles show the scattering of the nonlinear wave of the particle.
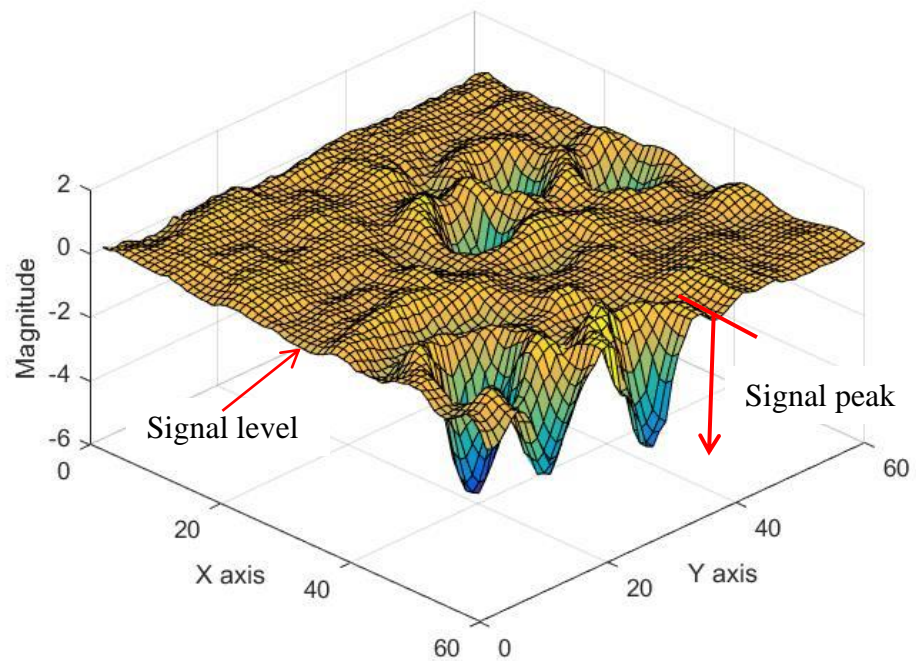
Figure 5-13: For the focusing area defined in(Figure 5-12), we plot the nonlinear wave signal that results from scattering off the particles. Scattering points result in a negative peak when compared to the base signal level.

Figure 5-13 shows a C-scan image of the focusing area defined in the pre-scan image (from Figure 5-12). The pre-scanning image has a resolution of 0.25mm/step. the C-scanning was repeated experiment by adjusting the scanning step to a resolution of 0.1mm/step with 60 by 60 steps and the same the setup in all other respects. The image from the particle phantom shows higher resolution (Figure 5-13) than the previous scan. However, the scan covers a smaller area, 6 mm^2, compared to 15mm^2 with the scan using a resolution of 0.25mm/step (Figure 5-14).
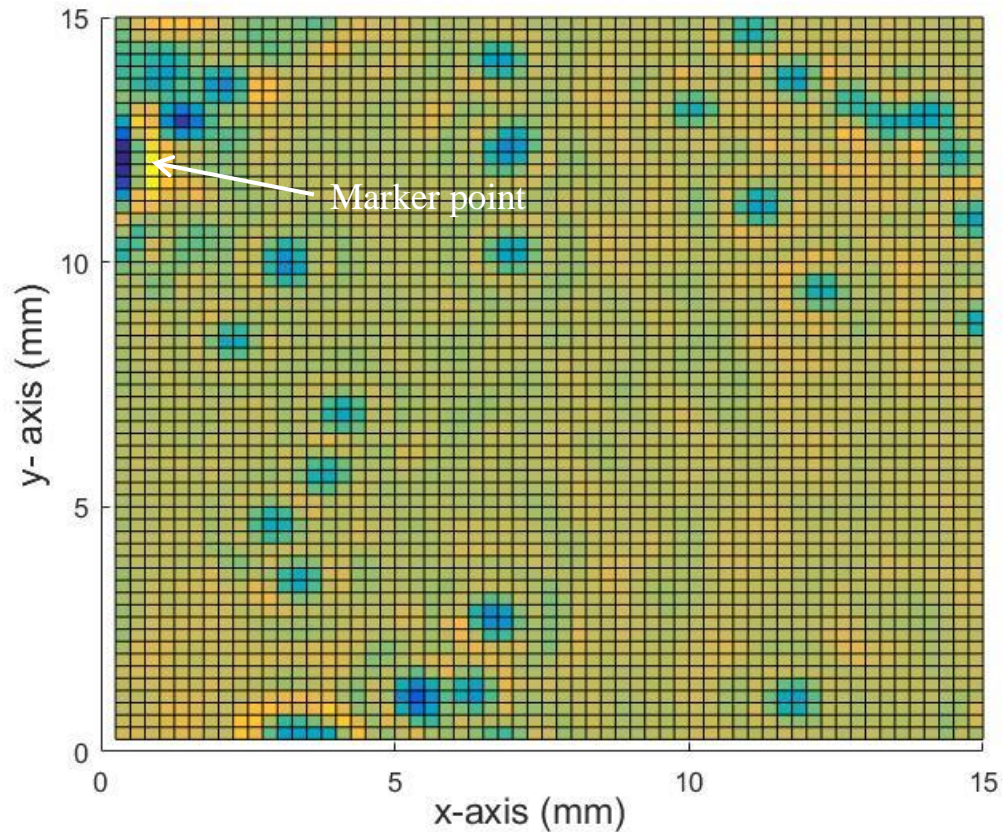
Figure 5-14: The nonlinear wave mixing scanning image shows the reflected result from the 150 μm particle size with resolution of 0.25mm/step. The marker point provides a reference for the scanning the phantom.

The effect of particle size was investigated with different size particles distributed in the phantom. To find smallest particle size which nonlinear wave mixing can detect, the measurement was carried out on 150μm, 100μm and 70 μm particle sizes dispersed in NIPAM gel phantom. There are two resolution scanning steps: 0.25 mm/step and 0.1mm/step.

Figure 5-15 (a) shows C-scanning with a step size of 0.25mm of the nonlinear wave mixing signal reflected off of 100 μm sized particles in the middle level of the phantom mold (see Figure 5-9 (a)). The results clearly indicate the presence of the particles (dark blue areas). The visible decease in nonlinear wave mixing energy when the initial wave interacts

with the particles shows that the nonlinear wave mixing method has enough sensitivity to image 100 μm size particles. Moreover, the nonlinear wave mixing signal strongly reflected when we re-scanned using 0.1mm step resolution (Figure 5-15 (b)). Figure 5-16 shows the nonlinear wave mixing signal C-scan image for 70 μm particles in the phantom. As in the previous experiment, the reflected signal from the particle is represented by dark blue areas (lower amplitude) in the nonlinear wave mixing scan. However, the image quality has a low resolution resulting in difficulteis to differentiate the particles.
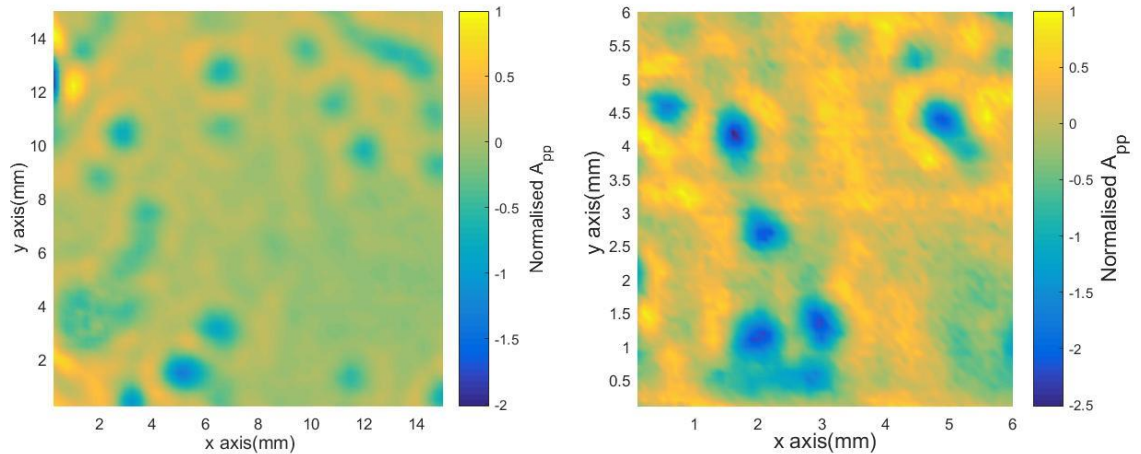
Figure 5-15: Nonlinear ultrasonic C-scan image of the NIPAM phantom with distributed 100 μm particles: the pre-scanning results were performed with a resolution step size of 0.25mm/step (a), and then the focusing area was located for repeating the C-scan (b) with 0.1mm/stem resolution. The scanning area was 15 square millimeters for 0.25 mm/step whereas it was 6 square millimeters for the 0.1 mm step resolution.
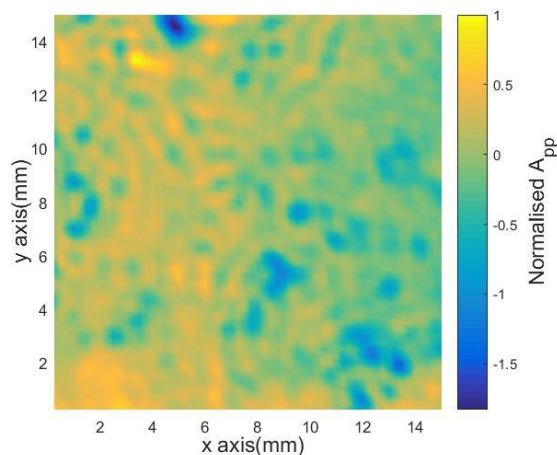
Figure 5-16: Nonlinear ultrasonic C-scan image of the NIPAM phantom with distributed 70 μm particles: the pre-scanning results were performed with a resolution of 0.25mm/step. The scanning area was 15 square millimeters.

5.3.5 Comparison of linear and nonlinear ultrasonic technique

One of the objectives of this study is to compare the linear and nonlinear ultrasonic measurement methods for wave deflection off of small particles. The comparison is carried out on the same tissue phantom with particles. The result of this experiment benefits from the strength of the nonlinear ultrasonic method for the detection of the deflected signal from minuscule particles and also its ability to evaluate nonlinearity in a tissue phantom.

The experimental setup was described in Section 5.2.1 with a 15mm thick tissue phantom diffused by 150 μm particles. The collinear wave imaging was performed using C–scanning at 0.25 mm steps in the x and y directions in a water tank at room temperature with a supported specimen. This setup also was used for linear through ultrasonic transmission mode with 6 MHz frequency, 10 cycle bursts and the nonlinear method using the collinear technique with 4.5MHz and 6.75MHz.

The C-scan image for the deflected signal using the linear ultrasonic measurement technique is shown in Figure 5-17 (a). The non-linear wave mixing results are illustrated in Figure 5-17(b) with the same experimental setup. The reflected signal is represented by the peak-to-peak amplitude for the wave deflected from the particle, as shown by the blue spots as mentioned previously. As before, we observed a decrease in the signal due to scattering and also clearly saw that the linear signal at 6 MHz is rather weak when compared to the nonlinear technique at 4.5MHz + 6.75MHz. The intensity of the initial wave generated from linear ultrasonic signal is around 0.5 (normalized peak-peak amplitude (A_{pp})) whereas it is about 2 (normalized A_{pp}) for nonlinear wave mixing. The nonlinear wave mixing results generated a stronger signal with higher contrast indicating the location of the particles than the linear method. The contrast from the linear method gives low-quality of information to distinguish the locations of the dispersed particles. In addition, it is clear that the nonlinear wave mixing shows differentiation between the background level of the signal and the peak signal (Figure 5-17 (b)). These results are consistent with earlier research which suggests that the nonlinear wave mixing has higher sensitivity. These techniques are proposed for the quantitative characterization of a small defect (Li *et al.*, 2016). It appears that the high contrast image from the nonlinear wave mixing method is from the higher frequency that results from the summed frequency, which is possible due to the nonlinear effect in the mixing. This is similar to a numerical study of non-linear wave mixing which found after the wave interaction, the wavefront increases the width, interval, and peak-amplitude of the group pulse. These increases may be the cause of the increase in the image contrast (Sun, Li and Li, 2016). This result suggests that this behavior may be used to evaluate a minuscule defect in material with high sensitivity, with an ability to differentiate small particles.
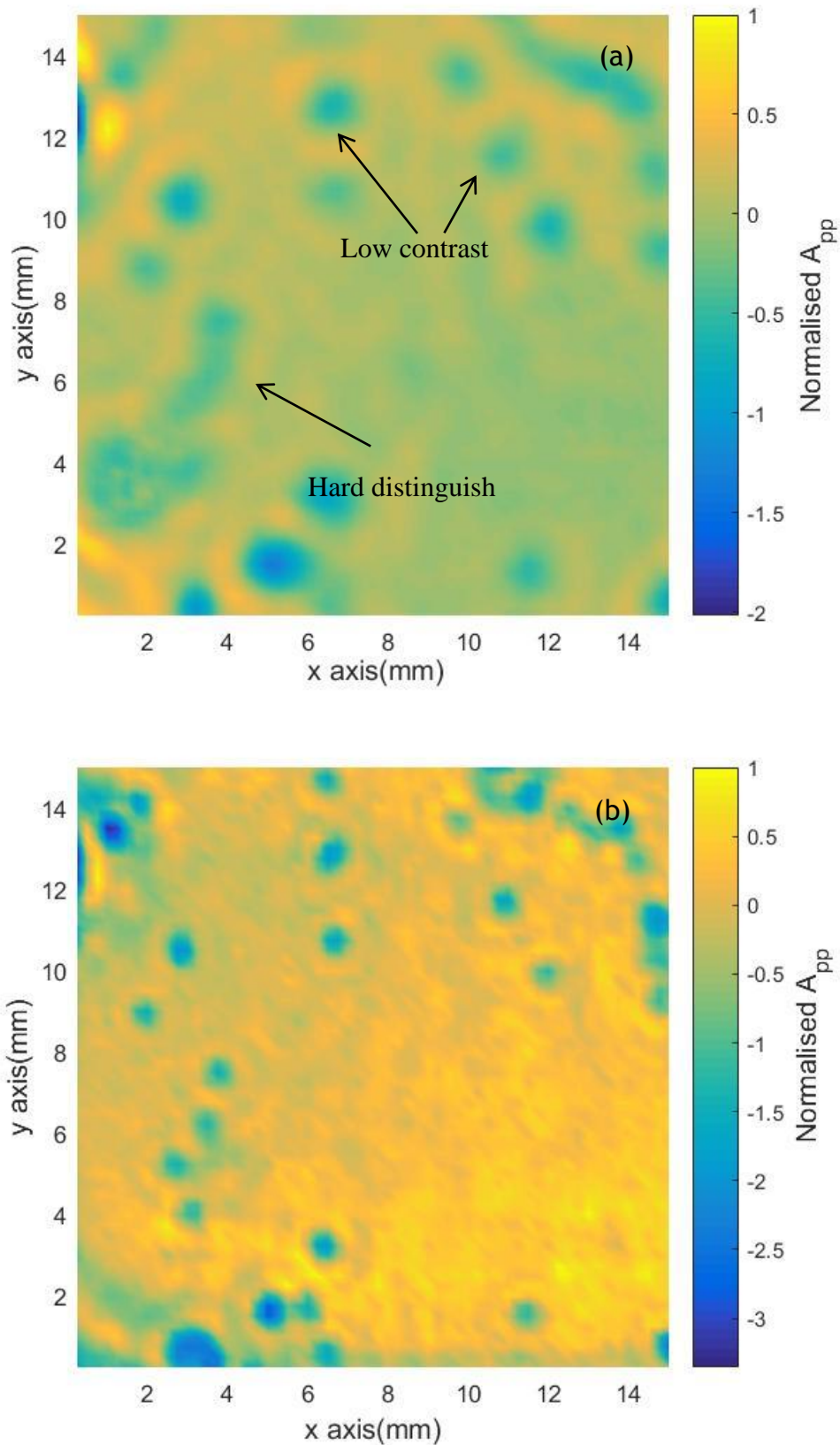
Figure 5-17: The C-scan image comparing between linear ultrasonic 6 MHz (a) and non-linear ultrasonic wave mixing (b) of two fundamental frequencies (4.5MHz and 6.75MHz). The experiment was performed on the same system measurement with phantom as well.
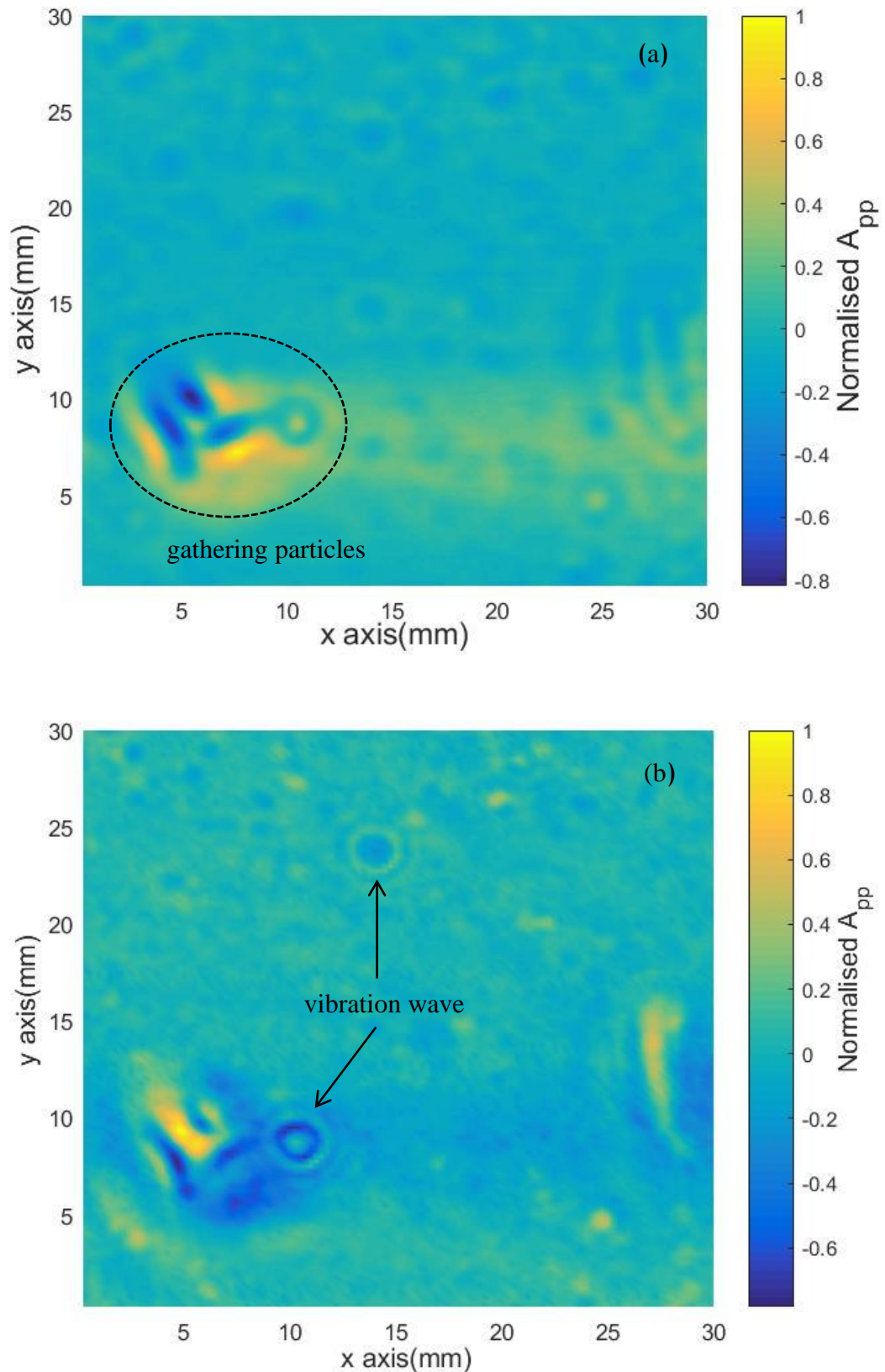
Figure 5-18: The C-scan image of linear and non-linear ultrasound comparisons.The C-scan image compared between linear ultrasonic 6 MHz (a) and non-linear ultrasonic wave mixing (b) of two fundamental frequencies (4.5MHz and 6.75MHz). The experiment was performed on the phantom with dispersed 70 μm particles. Some particles had not completed distribution due to the electrostatic force showing in the circle area. Both techniques were able to detect a vast congregated particle; however, the nonlinear wave mixing illustrated more contrast.

Figure 5-18 shows the C-scan image for a phantom with dispersed 70 μm particles. The scanning uses the same setup parameters as the previous experiment. However, for the dispersing particles in the phantom, the dispersion is incomplete in that some particles congregate together. The results of the C-scan image show that the nonlinear wave mixing result gives high contrast when compared to the linear method. The response of the particle congregation is shown in Figure 5-18 (a) and (b) however, the non-linear wave mixing gives significantly higher contrast in the reflected signal from the particle. The nonlinear wave mixing occurs at the summed frequency of 11.25 MHz in the measurement. In addition, some particle scattering produced a reflected ring surrounding the particle with an intensity of 0.2- 0.6 (normalized A_{pp}). This ring may be generated when nonlinear wave interacts with a particle which causes the vibration of the particle and then generates a resultant wave that propagates outward from the particle forming the ring. The oscillated wave would be from the nonlinearity of particles due to the particle behaves nonlinear hysteretic. The initial wave is distorted by their nonlinearity and then create associated harmonics, duplication of a wave of different frequencies and change in resonance frequencies(Van Den Abeele *et al.*, 2000; Van Den Abeele, Johnson and Sutin, 2000).

5.3.6 The response of the local defect area

A traditional ultrasonic method was used to detect a material defect based on an interaction between a linear wave and a defect area, as a result of amplitude and phase variation of the input signal. However, for the small defect, a high initial energy to activate the defect is required. This section describes an attempt to overcome this problem using the concept of a nonlinear ultrasonic resonant defect, which is associated with anharmonicity of the material. The principle properties of a nonlinear material are dependant on the stiffness of the nonlinear material and the strain which results from a local variation of the wave velocity and waveform distortion leading to higher harmonic generation (Van Den Abeele, Johnson and Sutin, 2000). The variation of the nonlinearity effects can be used to identify and localize the defect or the nonlinearity of the material. The oscillation driving the specimen with a defect particle generated a natural frequency (resonance) of the defect or damaged area called a local defect resonance.

In this experiment, the collinear wave mixing nonlinear signal was used for local excitation of particles representing the defect in the gel. The receiver transducer measures the higher harmonic response of the defect at the resonance frequency. The experiments were carried out with 100 μm particles dispersed in the gel phantom at driving frequencies of 4.5 MHz and 6.75 MHz with 10 cycle bursts.
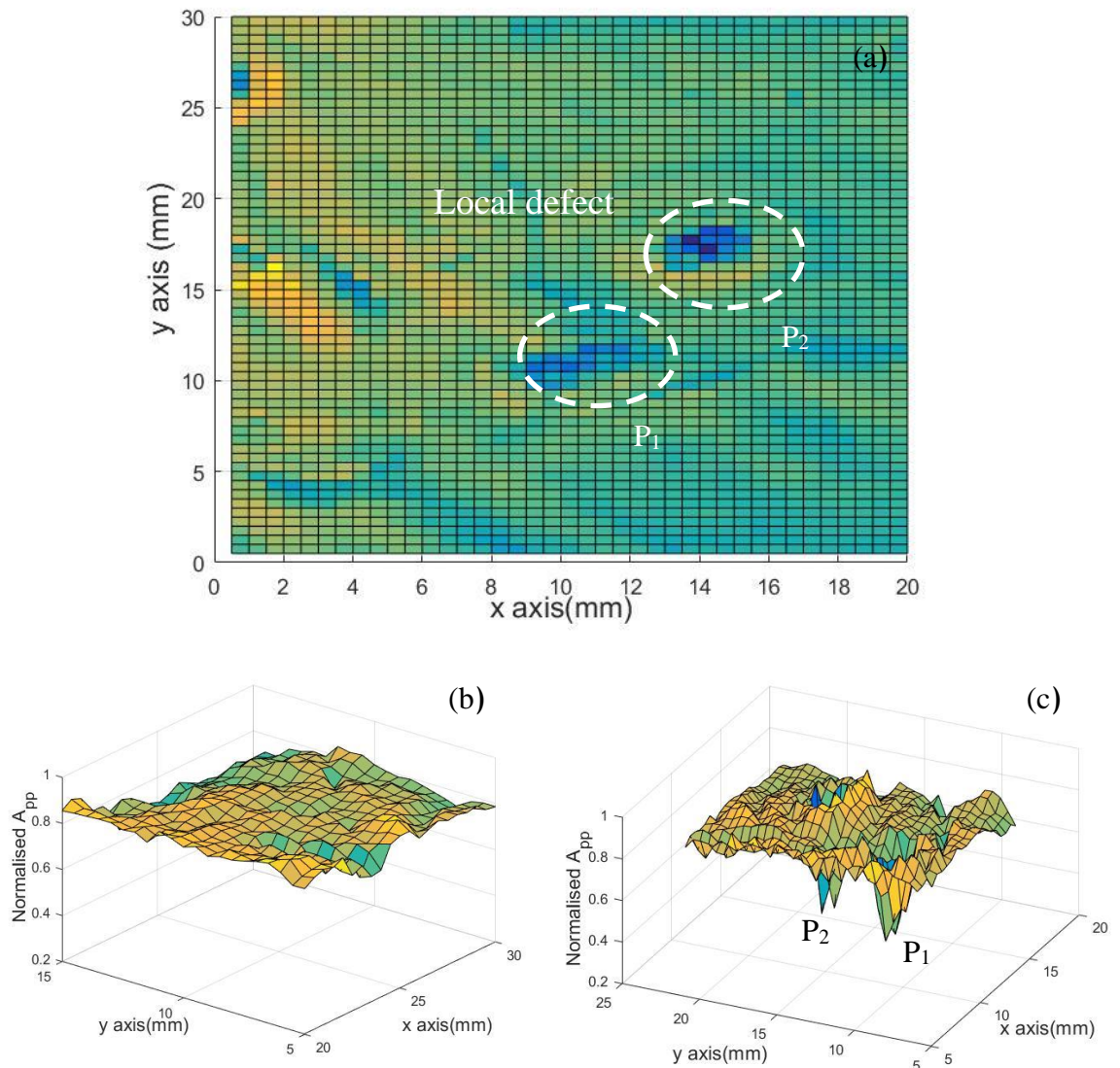
Figure 5-19: 2D images of local response to the collinear wave mixing.

The response pattern to the collinear wave mixing signal is shown in Figure 5-19 (a). It was noted that the driving frequency intensely affects the energy amplitude of the summed frequency for interaction with the local defect point (a particle). The amplitude at the local defects show significant reflection with lower amplitude (blue color) at the position P1 and P2 as indicated in the x-y coordinate system. Figure 5-19 (b) shows the tendencies of collinear wave mixing response for the normal area (no defect) when performing C- scanning image. It is seen that the level-plane of amplitude (Energy) varies around 0.8 (normalized A_{pp}) at the normal level plane. The summed frequency wave responds to the local defect as illustrated in Figure 5-19(c). The local response efficiently generates a signal with negative peak at 0.4 (normalized A_{pp}), which is out of the normal level plane. Obviously, the amplitude of the response signal is significantly different when compared to the normal level plane indicated by P1 and P2 location.

Figure 5-20 shows the vibration of the particle at a local defect. The collinear wave exciting signal not only generates the local deflected signal but also causes the vibration at the local area. When we consider closely the defect area, we found that the vibrations at the local area are from vibration of the particle. It was noted that the wavefront propagated along a horizontal plane. The response of the vibrated wave was likely homogeneous over the deflected area. The wave origin appears in the middle of the defect and propagates outward. The origin of the defect was the location of the particle, which can be identified by looking the amplitude of the reflected wave. The variation of the magnitude of the reflected wave over the local defect was in the range 0.8 -0.4 mVpp as shown in Figure 5-20(b). It indicates that the normal level of magnitude varies in the range 0.8 -0.9 mVpp and rapidly decreased to 0.3 mVpp 14 mm along the x axis. This is the location of the particle and the origin of the vibration.

The vibrations can be understood by considering the interaction of the particle with the standing wave as described by the theory of acoustic radiation forces on particles. The ultrasonic wave creates a standing wave in the gel in the direction of the acoustic wave. If the particle is at a node of the standing wave, it was trapped and remains stationary. However, if the particle is not located at a node, it will vibrate and generate local movement (Yamakoshi and Noguchi, 1998; Knoop and Fritsching, 2012). Our experimental results agree with findings from the previous experiment (Section 5.3.5). The particle is assumed to undergo movement via the ultrasonic pressure field in the near field, at 15mm. The oscillation of a particle can be calculated as described by Wei *et al.*, (2014).
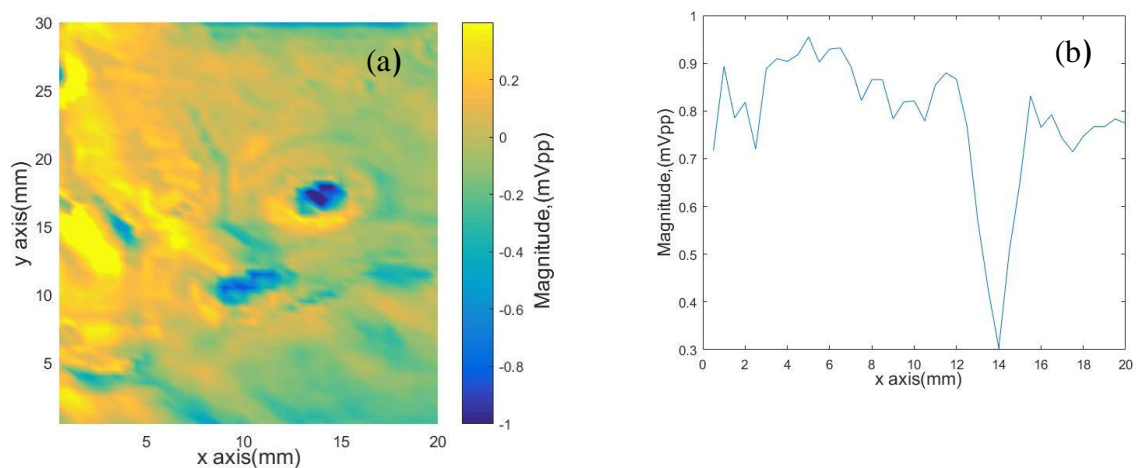
Figure 5-20: 2D-images of vibration mode for the local deflect area (P$_1$ and P$_2$) when zoomed in around the reflected area.

5.4 **Summary**

The collinear wave mixing ultrasound was successfully implemented for evaluating the particle deflection in a tissue phantom. The ultrasonic through-transmission mode was set up with an x-y axis moving stage for supporting the hydrogel phantom. Different driving frequencies of 4.5Mz and 6.75MHz were used to generate a summed frequency nonlinear wave mixing signal used to evaluate the deflected signal.

In order to generate the deflected signal, different microparticles (70μm, 100μm, 150μm) were distributed in the tissue phantom, which was made from NIPAM hydrogel. This kind of gel has many advantages for the proposed work, such as easy preparation, transparent material and acoustic properties similar to human muscle. The gel properties were verified before use.

The results clearly showed that the nonlinear wave signal can detect the different particles with higher sensitivity and resolution when compared to the linear ultrasound. The results of a C-scan from the nonlinear signal provide evidence that the high-resolution image of the deflected small particle can be measured by the nonlinear wave mixing technique. In addition, utilizing particles with size similar to ulcer, our results suggest it may be possible to detect a small size of pressure ulcer (70μm) deep in the tissue with nonlinear techniques.

Chapter 6   Nonlinear ultrasonic wave mixing for evaluating physical aging in polymers

Physical aging is the behaviour of polymers when they are exposed to high temperature. The aging mechanisms cause their properties to change. They become rigid, brittle, and dense. In this Chapter, non-linear ultrasonic wave mixing, a nondestructive technique, was used to evaluate the physical aging of polyvinylchloride (PVC). The system consists of two transmitters sending an ultrasonic signal to a specimen. The propagated signals from both transducers interact with each other in the material with specific angles. The result is a generated third wave highly sensitivities to material properties that can be applied for physical aging evaluation. This technique has the ability to detect the changing of material properties. It was found that the physical aging is more pronounced after rejuvenation and quenching processes and that the nonlinear wave mixing energy increased dramatically during annealing processes.

6.1 Introduction

Amorphous thermoplastic polymers such as polyvinylchloride (PVC) and polymethylmethacrylate (PMMA) are widely used in industrial applications including the medical device industry (Nouman *et al.*, 2017; Zemljič *et al.*, 2019; Girija, 2019), due to their competitive costs, simple processing, biocompatibility, and good mechanical properties. However when the polymers are exposed to temperature (up to 70 °C), they lose their properties and become rigid, brittle, and dense because the temperature causes a reduction in molecular weight (Jin, Li and Torkelson, 2017). This is a serious problem for these materials, affecting the material performance, especially for polymers. The prediction of their properties while aging, as they perform their functions, is important to prevent risk, especially in water and gas distribution networks (Gedde *et al.*, 1994). In addition, in order to control the quality of medical devices made from a polymer material, the guidance of polymer medical devices (ASTM D3045) has been issued to guarantee that their properties can be stored for an extended period without any decrease in performance and efficacy when their devices are used. This procedure is called the Simplified Protocol for Accelerated Aging which was based the Arrhenius model with an applied activative energy for driving the reaction (ASTM committee D20, 2003; Gillen and Celina, 2016).

Physical aging is not a new subject, and has been known and thoroughly studied. The aging of material has been studied in many research fields, especially polymer science. Most of the amorphous polymers demonstrate physical aging which would be affected by the density, stiffness, and brittleness of polymer (Kucera, Felton and McGinity, 2013). When an amorphous polymer is exposed to high temperature over that of the glass transition temperature, it results in a loss of strength and increased stiffness, leading to brittleness and breakage. The glass transition temperature (T_g) is essentially the melting point of the polymer when it changes form a solid to a rubbery stage and then when its temperature is cooled down to the beta transition temperature (T_β), the polymer returns to the glassy stage again.   This process, known as physical aging, leads to structural relaxation, which is a reorganisation of the material's structure after heating. This behaviour can be observed below T_g and significantly affects the polymers mechanical properties. This causes amorphous polymers to change their properties when annealed at a specific aging temperature below T_g and, as a consequence, leads to changes in the molecular mobility of polymers. This phenomenon can be characterised by thermodynamic quantities, local structure, free volume kinetics, and crystallization (Hutchinson, 1995; Cangialosi *et al.*, 2013). Struik (1977) reported the basic aspects of the physical aging phenomenon. The report described the concept of free volume when the polymers are quenched from the equilibrium to the non-equilibrium state, their volume clearly displays a decrease of specific volume as a function of time. This is a consequence of the decrease of the free volume of materials and leads to their loss of molecular mobility as a result of aging. Hutchinson (1995) published a review paper of physical aging of polymers which included numerous phenomenal aspects. Based on dilatometry and calorimetric methods, he summarised the physical aging behaviour in microstructural aspects and also clearly described the thermodynamic state of polymers. Cangialosi *et al.*, (2013) provided a critical review of physical aging in polymer and polymer nanocomposites. They explained the fundamentals of physical aging, summarised the methods to monitor physical aging, and also focus on two methods for evaluating the aging of glassy polymers and polymer nanocomposites. The aging induced changes in the dimensional and mechanical performance of materials involved in physical aging have been widely discussed in industrial literature.

Various techniques have been used to evaluate physical aging including differential scanning calorimetry, creep deformation, dilatometry and dynamic mechanical spectroscopy (Hutchinson, 1995). For example, the basic principle of differential scanning calorimetry is applying a constant heat rate with two chambers, the specimen and reference chambers. The chamber with specimen consumes more energy than other. This energy difference is called the specific heat which is evaluated as a function of temperature (Drzeżdżon *et al.*, 2019).

Creep deformation is based on the tensile test where a constant force is applied to the materials. Then, an increase in the stress-stain curve at the yield stress can be represented by physical aging (Fairhurst, Thommen and Rytka, 2019). Another dilatometry method has been used for aging measurement since the 1930s. The measurement involves the dimensional change of a specimen under the fixed temperature then observing the deviation of length with temperature (Hunkel, Surm and Steinbacher, 2018). However, many of the mentioned methods are destructive techniques of physical aging inspection and the detection method is limited. For example, calorimetry needs some specimens for heating and evaluating physical aging. In addition, the tensile test measured yield stress deformation has been found to vary with frequency (Demčenko, Akkerman, *et al.*, 2012). It should be noted that those techniques are not practical for evaluation in field inspections and also are suitable for physical aging investigation in the laboratory and they would be the non-destructive measurements.

Ultrasonic wave velocity and attenuation have been widely used for investigation of acoustic mechanical properties of the polymer (Perepechko and Golub, 1973; Pouet and Rasolofosaon, 1989; Koda *et al.*, 1993; Higazy *et al.*, 1994). In those studies, a longitudinal and transverse sound wave was used for evaluating the properties of polyvinyl chloride and other polymers in terms of sound velocity, attenuation, and dispersion of the ultrasonic wave and also the elastic modulus (Koda *et al.*, 1993). The characterisation of aging of a polymer via ultrasonic wave has been reported for the study and comparison of the tensile creep compliance with various kinds of dynamic measurement techniques such as a tensile non-resonance method (0.01 – 60Hz), audio frequency flexural resonance (100Hz – 4 kHz) and the ultrasonic wave propagation technique (1-5MHz) (Read *et al.*, 1992).

However, Demčenko *et al.*, (2012) showed that the classical tensile compliance test for PVC physical aging has loss their values at the wide range of aging time ($10^{-8} – 10^6$ s) at 23 °C. They also proposed that the non-linear ultrasonic technique has high sensitivity for material characterisation in terms of physical aging. A pipe of PVC was investigated for physical aging after the quenching process then linear and non-linear ultrasonic measurements were performed to detect the state of physical aging of PVC. Moreover, not only can nonlinear acoustic techniques be applied to measure physical aging processes of thermoplastics, but they can also be used for the monitoring of epoxy curing processes as well (Demčenko, Koissin and Korneev, 2014). The literature shows that if nonlinearity of PVC during aging occurs after quenching and annealing processes below Tg, then non-linear ultrasonic wave mixing is observed with annealing time dependence only. However, increasing the annealing temperature leads to accelerated physical aging. In addition, few studies have reported on the non-linear ultrasonic wave mixing for physical aging

acceleration in PVC with varying annealing temperature (Read *et al.*, 1992) (Demčenko, Akkerman, *et al.*, 2012).

According to histology of tissue studies of compressive pressure on rats, skin and muscle tissue cannot tolerate high mechanical loads. When the skin and tissue are loaded by 13.3 kPa for seven days on the tibialis areas (Mak, Zhang and Tam, 2010), the observed results showed that this pressure cause deep tissue ischemia then develop tissue damage and PUs. During the time for PU development, there are a lot of changes in tissue properties, beginning after six hours with tissue ischemia, after 48 hours with degeneration of muscle fibers because of increasing of nuclei, at 72 hours atrophic and hyperprophic muscle fibers are present, at 96 hours muscle fibers are replace by fibro-fatty tissue and become tissue necrotic, then at 168 hours muscle fibers become severely necrotic. This progressive development of PUs is time dependent during the loading on skin tissue and contributes to stages of PU development. In addition, the level of ischemic tissue causes not only an increase in the acoustic backscatter coefficient of tissue but also to an increase in the acoustic velocity (O'Donnell, Mimbs and Miller, 1981; O'Brien *et al.*, 1981). This would be a condition for monitoring each stage of PU development.

In this work, we studied non-linear ultrasonic wave mixing techniques used for material characterisation. The measurement system was set up in the laboratory with high precision and quality devices: transducers, oscilloscopes, power amplifiers, and computer (see Chapter 3). After understanding the non-linear wave mixing system, we applied it to the investigation of physical aging acceleration in polyvinyl chloride (PVC). This behavior of polymer is time dependent and analogous to the behaviour of polymer physical aging and ulcer development. Last but not least, the system could be used for characterising damage in materials and structures because of the system's sensitivity.
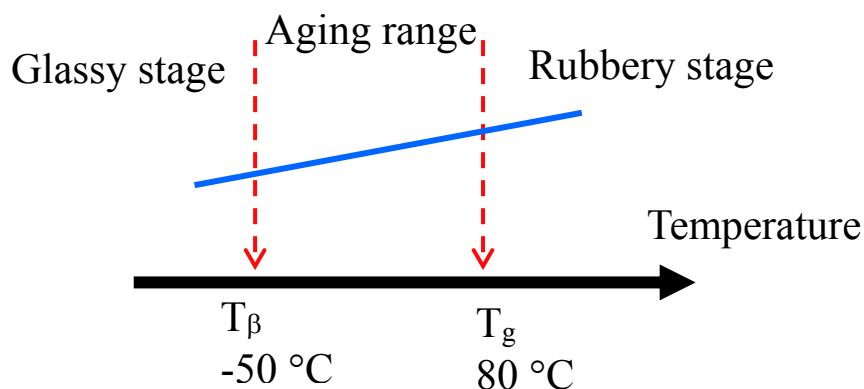
Figure 6-1 The aging phenomenon usually occurrs between glass transition temperature T_g and beta transition temperature T_β. When the temperature exceeds T_g, there is a change stages the solid to the rubbery stage. Cooling below T_g results in a transition to the solid stage with aging occurring.

6.2 Material and method

6.2.1 Experimental setup

The non-linear ultrasonic wave mixing for physical aging evaluation is shown in Figure 6-2. It consisted of two transmitters sending an ultrasonic signal to a specimen. The propagated signal from both transducers interacts with each other in the material with specific angles. The result of the interaction is a third generated wave which can be detected by the ultrasonic receiver. This wave has high sensitivity and can be used for the detection of non-linearity of material quality. In this experiment, this signal was applied to the evaluation of physical aging in polymers. In order to reach the wave mixing condition, the geometry configuration of the transducer was first setup depending on the wave interaction combination then according to the geometry configuration parameters leads to the experimental setup (see Chapter 3 for non-linear wave mixing experimental setup). The specimen was arranged in a horizontal position with parallel to transducers, in order to confirm the specimen balance, a level balance scale bubble tool was used for horizontal verification while the experimental setup.
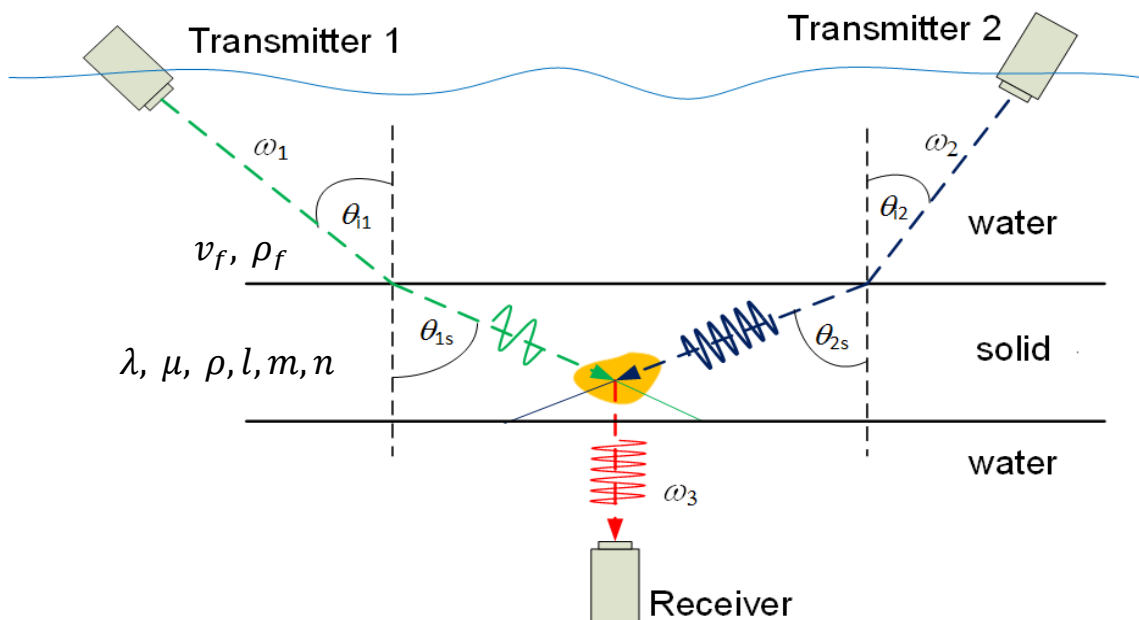
Figure 6-2 ; Non-linear ultrasonic wave mixing measurement system,
when two waves interact and meet the resonance condition, a mixing wave (ω_3) is generated. The reflected wave propagates at a specific angle which can be detected by the receiver transducer.

In order to avoid the acoustic impedance effect (Lee, Lahham and Martin, 1990), the measurement was performed under water, coupling in a glass chamber as shown in Figure 6-5. When the through-transmission mode was needed, the receiver was arranged on the bottom of the specimen. For working in this mode, the wave mixing signal was stronger than in the pulse-echo mode (a receiver picked up the reflected signal on top).

The hot plate with adjustable temperature was installed for controlling temperature of the water in the chamber with water circulation by a magnetic stirrer for temperature stabilization.

The inclination angles of transmitter 1 and transmitter 2 can be adjusted precisely by using rotation stages with 360° coarse and 5° fine. Both transducers were attached to the adapter tube and mounted on the rotation stage. The length of the tube is suitable for the arrangement of the geometry configuration.

The driving parameters for the pump wave sources were described in Section 3.2.3. The pumping frequencies of both transducers are chosen in relation to the interaction angle, scattered angle, and amplitude coefficients to produce an ultrasonic wave mixing signal as described in Section 3.2.1.

6.2.2 Experimental procedure

PVC sheets were prepared as specimens for the experiments. In order to fit in the glass chamber, the dimension of the PVC sheets are 80 x 100 x 9 mm. All PVC was supplied by Oroglas company with glass transition temperature Tg 80 °C, the beta transition temperature Tβ -50 C° (Struik, 1977). The PVC samples were heated to 10°C above Tg for 60 minutes to erase the thermomechanical history and the temperature was checked immediately. The temperature was measured to be 90°C by Fluke Ti85 Instrument. Next, heated specimens were quenched in an antifreeze liquid of temperature -34 C° for 20 minutes. The cooling temperature was maintained by an immersion cooler (JULABO FT402). After that, the quenched PVC sheets were placed into a water bath, where the nonlinear ultrasonic measurements were performed with a 30 s sampling rate. A magnetic stirrer was used to maintain a uniform temperature distribution in the water chamber. Data were collected for one hour at each of the following four annealing temperatures: 24°C, 26°C, 28°C, and 30°C.

6.3 Results and discussion

6.3.1 The simulation

In this section, a simulation was performed to predict how the waves interact and propagate in water and the PVC specimen interface. The two main parts in the simulation of the ultrasonic displacement are due to linear wave propagation and non-linear wave interactions. For each case, the system has a certain setup involving the frequency ratio of two initial waves, inclination angles, and specific material properties (see Chapter 3). The simulation was based on the distributed point source method (DPSM) developed for ultrasonic field radiation simulation of a fluid - solid interface using Green's function for the displacement calculation at the interface layer. The DPSM concept is that the front surface of a transducer has a small number of point sources dispersed surrounding the transducer area. These sources generate the ultrasonic field distributed through the two layers. The implementation details of the DPSM are clearly described by Banerjee, Kundu and Alnuaimi, (2007). By using this approach, the nonlinear elastic field can be calculated including both horizontal and vertical displacements. The following summarises the procedure for the simulation. First the geometry of two transducers was created using a grid as described in DPSM method. Then the point-source strengths were computed at the interfaces layer by using global matrices at two excitation frequencies. Finally, the nonlinear forces propagating to the solid were calculated along with the linear elastic fields (Demčenko *et al.*, 2019). The numerical results show the directions of linear and nonlinear wave reflections from the interface. The direction of the two ultrasonic waves from different sources propagate from the water medium and reflect on the boundary surface of the PVC specimen. We first consider the vertical displacement of the field (Figure 6-3). When a driving source TR_1 generates the ultrasonic wave, the displacement propagates to the interface boundary and was transmitted to the specimen as a shear wave (SV, blue line), which propagates along direction k_1, as defined in Section 2.4.1.
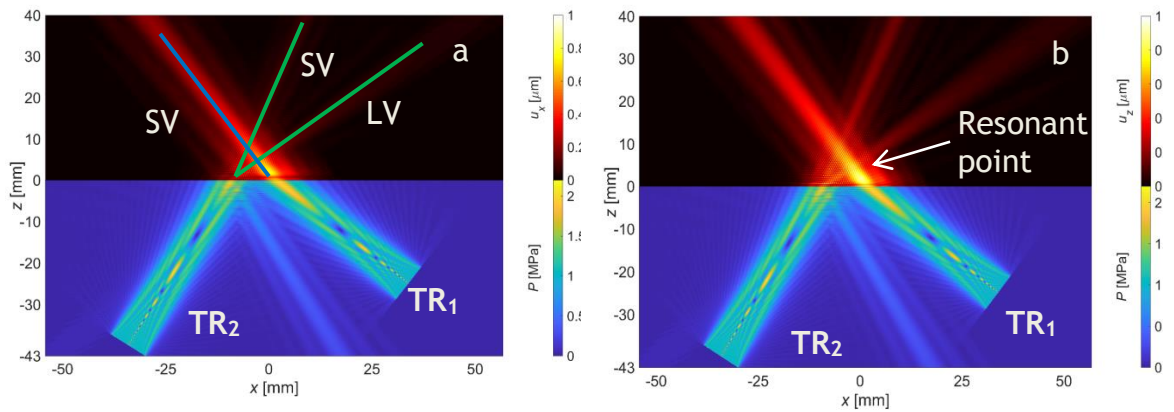
Figure 6-3: The horizontal and vertical displacement of the linear ultrasonic field. Panel (a) highlights the direction of linear ultrasonic wave propagation. Panel (b) shows the resonant point.

For source TR_2, the longitudinal (LV, green line) and shear wave (SV, green line) were generated after transmission through the boundary. For non-linear waves we ensured condition 7 of Table 2.1 was satisfied. Therefore, the shear wave and longitudinal wave produce a resonant longitudinal propagated wave (LV), along the direction of k_3. This resonance point can be clearly seen in Figure 6-4 (b). We note that the interaction point is located in the middle of the specimen (z is about 5 mm). This is an expected result that would be required for practical measurement.

We also consider the ultrasonic energy densities of the waves propagating from a source to the boundary. The numerical results show that the displacement value and pressure intensities are in the range $0.2 - 0.8$ μm and $0.5 - 2$ MPa, respectively.
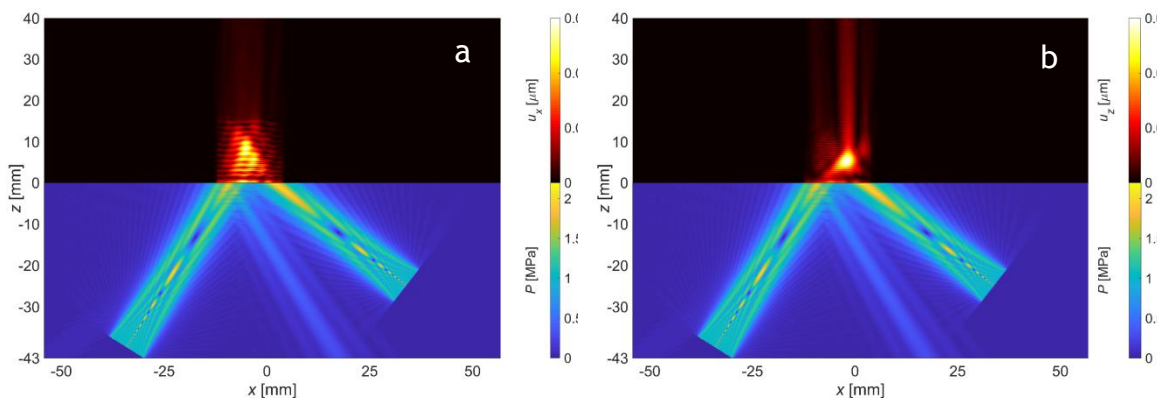
Figure 6-4: Interaction of non-linear ultrasonic waves. (a) The interference of two primary ultrasonic waves. (b) The resonant point of the non-linear interaction.

The linear and nonlinear ultrasonic wave propagation was evaluated to understand the direction and behavior from the horizontal and vertical viewpoints. When two primary ultrasonic waves with frequencies 2.5 MHz and 3.75 MHz meet with each other, the mixed wave at frequency 6.25 MHz was generated. Figure 6-4 (a) shows that when longitudinal and shear wavefronts combine, the wave interference can be observed clearly. The

interference region is limited to the region of overlap of the two waves. The area of interference shows a high intensity of displacement in the range of $0 - 0.01$ μm. After interference, and as a result of non-linear wave mixing, a third wave with frequency equal to the sum or difference of the two fundamental frequencies, propagates at 90° with weak intensity of 0.01 μm (see Figure 6-4(b)). Clearly, the simulation indicates that the non-linear wave of 6.25 MHz was created in the area for detecting physical aging and the generated non-linear wave can be received by a transducer. In addition, it can be seen that the non-linear wave mixing energy is attenuated by 2 dB from the linear interaction because of the interaction processes. The results also suggest that the transducer used to pick up the signal should have high sensitivity and the amplifier should provide a good signal to noise ratio.

6.3.2 Experimental results

6.3.2.1 Experimental system and received signal determination

The practical setup for non-linear ultrasonic wave mixing is shown in Figure 6-5 and consists of TRx1 and TRx2 (ultrasonic transmitters) with a central frequency of 5 MHz used for driving the ultrasonic signal. A 10 MHz broadband ultrasonic transducer was used for the receiver. The inclination angle of TRx1 and TRx2 are 52° and 32° respectively (see section 3.2.2). The angles combined with the geometry of the setup and the frequencies of the waves, result in a nonlinear ultrasonic signal. When the specimen was placed at the interaction point, the resultant wave was changed based on the properties of the specimen. The resultant wave then has information about the material and can be detected by the receiver. According to the geometry configuration and resonance condition parameters, the pumping frequencies f_1 and f_2 are fixed at 2.5 MHz and 3.75 MHz and when the measurement system satisfies the resonance condition, the resonance frequency was 6.25 MHz picked up by a 10 MHz transducer. The through-transmission mode with the receiver arranged (receiver on the bottom) under the specimen was chosen in order to avoid the loss of signal from the reflection. However, the pulse-echo mode can be also be used for measurement, depending on the arranged area, with advantages and disadvantages for both methods (Wrobel and Pawlak, 2007).
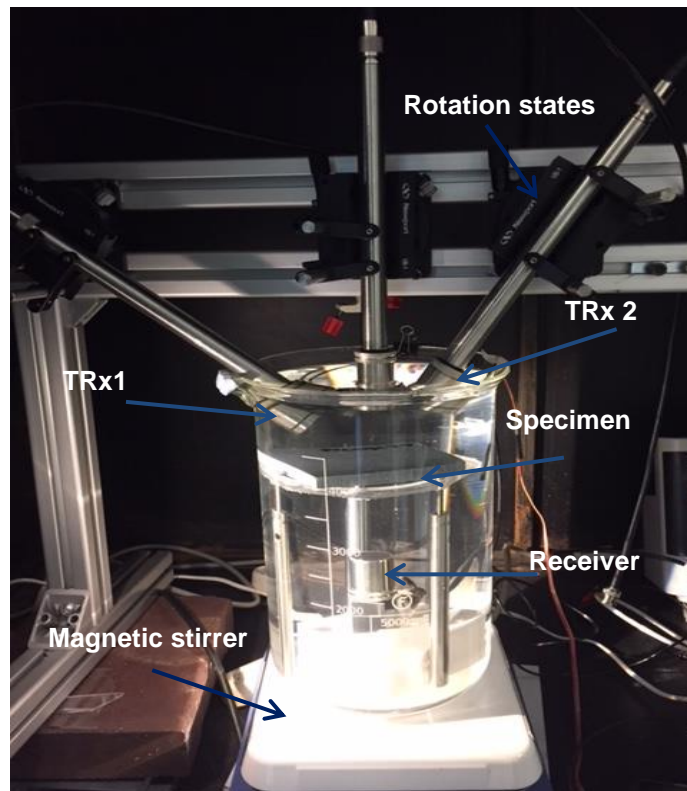
Figure 6-5: The non-linear ultrasonic wave mixing experimental setup is performed in a water chamber. The measurement system consists of the transmitting transducers (TRx1, TRx2) and receiver transducers at fixed incident angles. The aluminum frame is used for holding the rotation states attached to the adapter transducer tubes. In the chamber, a stand provides specimen support while the measurement is performed.

A magnetic stirrer stabilized water temperature in the chamber, however it took time to reach a constant temperature because of the heat transfer effect. Another important fact was the precision of temperature control while the non-linear ultrasonic wave mixing was measuring the physical aging. Fluctuations in water temperature in the chamber made the non-linear wave mixing signal unstable due to the high sensitivity of the system.
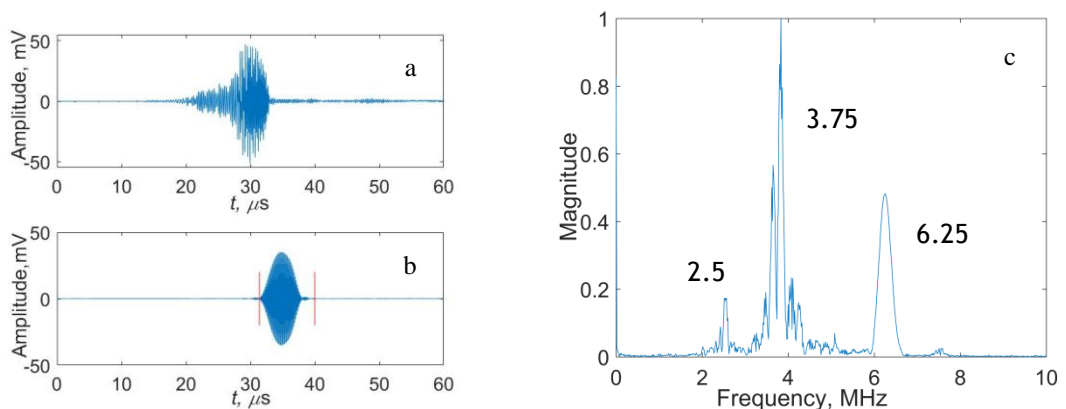
Figure 6-6: Received non-linear wave mixing signal when pumping frequencies are 2.5MHz(f_1) and 3.75 MHz(f_2). (a) The raw signal picked up from the receiver, (b) the non-linear wave mixing signal after filtering the raw signal, and (c) the frequency spectrum.

Figure 6-6 (a) shows the raw signal received from a transducer which is derived by fixed frequencies f_1 and f_2. The amplitude of sum-frequency 6.25MHz as shown in Figure 6-6 (b) generated by wave mixing was filtered with a Kaiser window filter providing narrowband filtering and easy-to-change filtering parameters. This non-linear wave mixing signal was applied for physical aging detection. The amplitude was more sensitive to changed material properties so that the non-linear wave mixing energy was calculated to represent the trend of the changed signal. The energy of the non-linear signal can be found in the frequency domain by $P(t) = \int_{t1}^{t2} X(t)^2 dt$, when $X(t)$ is the non-linear signal value in the time domain, t_1 and t_2 are a time period of action time (Changping *et al.*, 2004). In practice, the raw signal can be measured without signal filtering because the non-linear wave mixing signal was superimposed in the raw ultrasonic signal.

When the resonance condition of non-linear wave mixing was satisfied, the raw signal contains a non-linear wave mixing component. Then the raw signal is filtered and processed on the computer to study the properties related to physical aging.

6.3.2.2 Physical aging signal

For the physical aging measurement in a PVC sheet, the experimental procedure described in Section 4.2.2 was implemented. The experiment was carried out at four annealing temperature points of 24°C, 26°C, 28°C, 30°C. Figure 6-7 shows a normal graph of non-linear wave energy (E) during 24°C annealing. In the beginning, when a quenched specimen was placed in a water chamber, its temperature is lower than that of water.
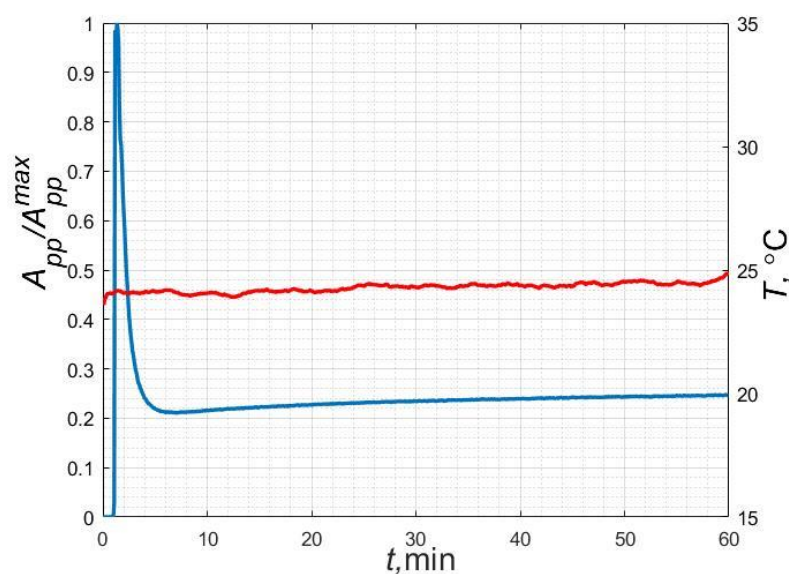
Figure 6-7: Non-linear wave energy when performing the physical aging process in one hour. The graph shows the normalised nonlinear wave energy during the physical aging process at   24 °C annealing. The wave energy was calculated from a peak-to-peak nonlinear wave component of 6.25 MHz.

This temperature difference leads to a rapid change in the properties of the specimen and results in the spike observed in the measured nonlinear ultrasonic wave energy. The specimen was inserted in the water and the signal began at the peak in the normalized energy. Then, we observed a trend of decreasing nonlinear ultrasonic wave energy simultaneous with a decrease in temperature difference between the specimen and water and associated decrease in heat exchange. Therefore, the energy of the nonlinear ultrasonic wave decreased, with this trend ending when the specimen temperature becomes equal to that of water. This temperature equilibrium is seen in Figure 6-7 when the energy of the nonlinear wave becomes lowest, which was observed after approximately 7 min for PVC, the same as reported by (Demčenko, Koissin and Korneev, 2014). Further, the nonlinear wave energy started to increase due to the physical aging in the PVC. While measuring the physical aging process during annealing, the water temperature in the chamber should be constant. Fluctuating water temperature induces fluctuations in the non-linear wave mixing signal as shown in Figure 6-8. The graph demonstrates steps in the wave mixing energy during physical aging. The reason for this behaviour is the effect of altered temperature on the molecular mobility of the material, causing the non-linear wave mixing signal to change accordingly.
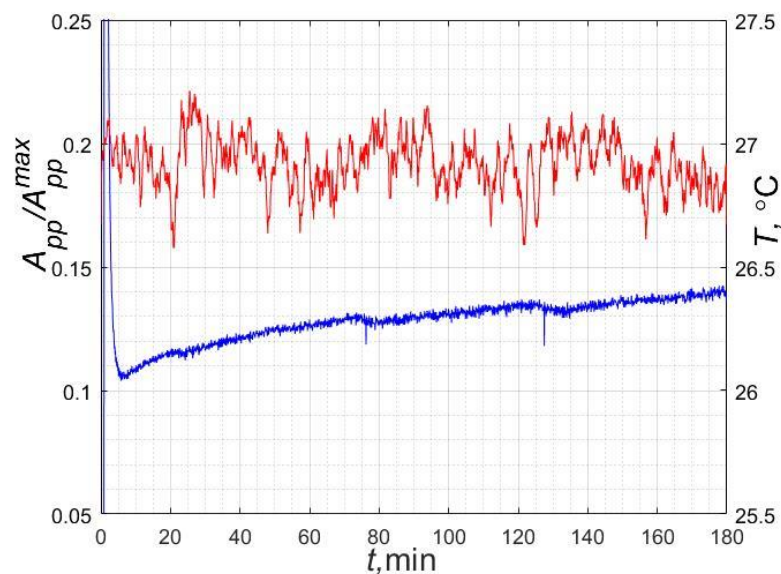
Figure 6-8: Fluctuating non-linear wave mixing energy for an annealing temperature of 27 °C.

When the thermodynamic state of a glass polymer is considered, a polymer molecule usually has a randomly coiled shape, internal energy (entropy) is very low. When the temperature is higher than T_g, the configuration seems to be a slightly extended chain and indeed looks like stretched state. Then the material would tend to return to the unstretched state and reduce the specific volume with time (Hutchinson, 1995). In the equilibrium state, the molecular

mobility is high. They are then quenched immediately into a cool liquid below T_g, producing an amorphous polymers would have in a nonequilibrium state with low molecular
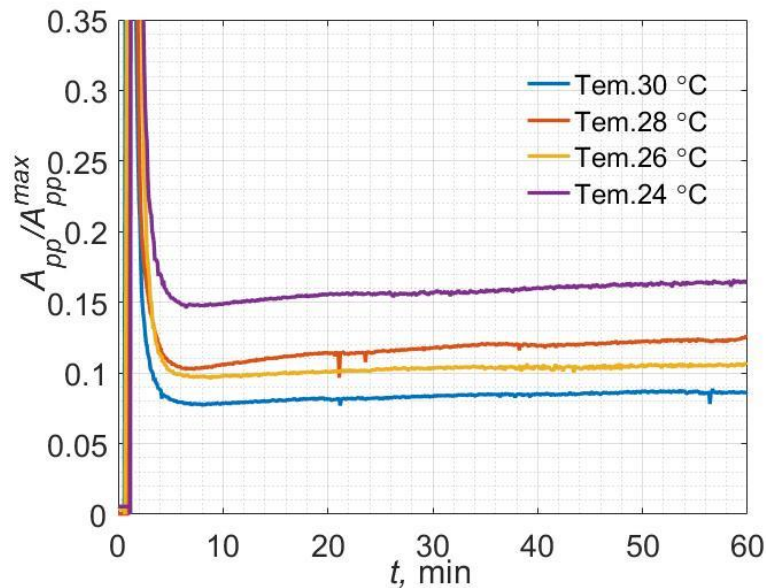
Figure 6-9: Effect of thermal annealing on non-linear wave mixing energy during the physical aging process at 60 minutes. The annealing temperatures were 24 °C, 26 °C, 28 °C, and 30 °C.

mobility. The mobility then gradually approaches equilibrium. This process is physical aging (Struik, 1977).

6.3.2.3 Effect of thermal treatment of PVC on non-linear wave mixing signal

The effect of the annealing temperature on PVC mechanical properties is shown in Figure 6-9 when the PVC specimen is cooled down from 100 °C to the annealing temperature (24 °C, 26 °C, 28 °C, and 30 °C). We observed different minima in the non-linear wave mixing energy after quenching. The result indicates that the trend of non-linear wave mixing started to increase slowly as a function of elapsed time. The lowest minimum occurs for the highest annealing temperature (30°C), where there is a maximum temperature gradient between water and the quenched specimen. The slope of all curves slowly increases, as can more easily be seen with a log time scale.

The behavior as presented in Figure 6-9 is linked to the volume relaxation concept described by Struik (1977). His studies showed that a quenched process was the result of the volume relaxation involved in the transition from equilibrium to the non-equilibrium glassy state. The effect of this is a decline of free volume present in the PVC and an associated change in the polymer modulus, the molecular mobility of material, and the polymer density (Cugini, 2015). Consequently, measurement of the modulus of the material demonstrates

how the material ages with time, and therefore leads to an understanding of the non-linear wave mixing signal behavior. Figure 6-9 shows that the lowest amplitude of non-linear wave mixing energy is 0.15 a.u at an annealing temperature of 24°C, whereas it is 0.08 a.u at 30°C. This implies that the higher annealing temperature causes more reduced free volume in PVC (the density increases) than the lower temperature. This is the reason for the shifted lowest point of non-linear wave mixing energy as a function of temperature.

The non-linear wave mixing signal amplitude is plotted a function of time. The aging was studied for about 60 minutes and the measurement was performed after the specimen was quenched. During physical aging, the non-linear wave mixing signal increased slowly with time. It was caused by the decreasing free volume when a polymer approaches equilibrium, which agreed with the previous work by Ricco and Smith (1990). They evaluated the physical aging of polycarbonate during stress relaxation with an applied a constant strain. Their results showed that μ (rate constant) was about 1.37 at 30°C and that it increased progressively with the temperature and became approximately 2.13 at 110°C.

6.3.2.4 Physical aging acceleration determination

The aging rate of PVC as show in Figure 6-10 for different annealing temperatures is difficult to see, given the scale of the plot. The measurement results are scaled by the maximum peak-to-peak amplitude to normalized results (A_{pp}/A_{pp}^{max}). The non-linear wave mixing curve from the physical aging processes with different annealing temperatures (see Section 6.3.2.3) has a shift following quenching of the specimen before the aging processes begin. The shift clearly moves vertically as a function of temperature. When the curves are shifted to a common reference point, they show different slopes which can be fitted by linear functions (see Figure 6-10). The slope represents the physical aging rate which slowly increases with annealing temperature. This behavior is due to an increase of the polymer densification and the stiffness because of the free volume decrease when a polymer returns to equilibrium state described by free volume theories proposed by Struik L.C.E., (1977). This behavior is similar his experiments on the strain tensile creep test of PVC. His results also indicated that the physical aging rate of PVC, a shifting creep compliance curve, can be described by a shift creep rate which has been evaluated at 40 °C annealing temperature as a function of elapsed time.

From Figure 6-10, it is clear that there is an increase of slope due to thermal annealing temperature leading to an increase in non-linear wave mixing energy. The results show that the modulus of slopes were about 147 ×10^{-6} to 383×10^{-6} in units of energy per time, and they gradually increased with the annealing temperature.
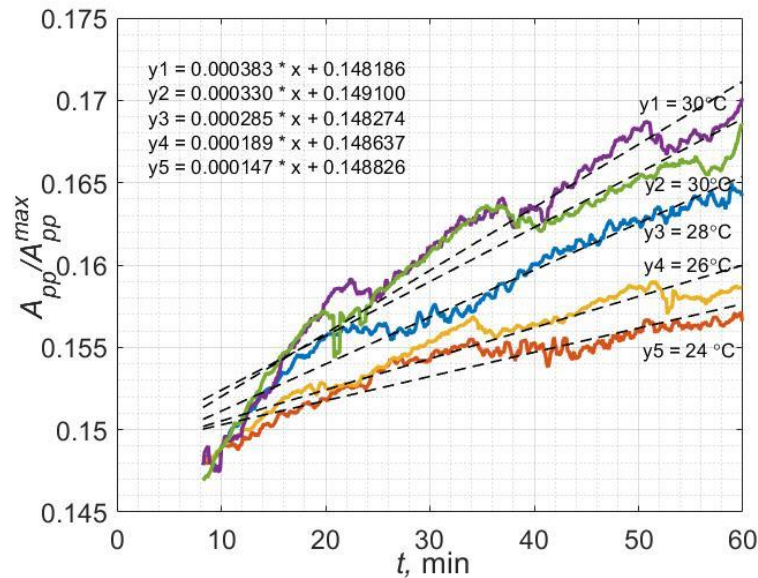
Figure 6-10: Normalised non-linear wave mixing energy curve fitted by a polyfit MATLAB function.

This rate may be detected by non-linear ultrasonic wave mixing techniques while the molecular mobility changes with time during the physical aging process (Kalfus, Detwiler and Lesser, 2012). The small slopes (see Figure 6-9) and their changes with annealing temperature resulted from changes in polymer mobility. As the mobility increased, the rate of molecular recovery to equilibrium increased which resulted in accelerated aging as a function of temperature (Ricco and Smith, 1990). In Figure 6-11: the aging rate was plotted on a log time scale as a function of temperature for all annealed temperature, as suggested by Struik. As seen in Figure 6-11 (a), the annealing temperature affects aging acceleration.
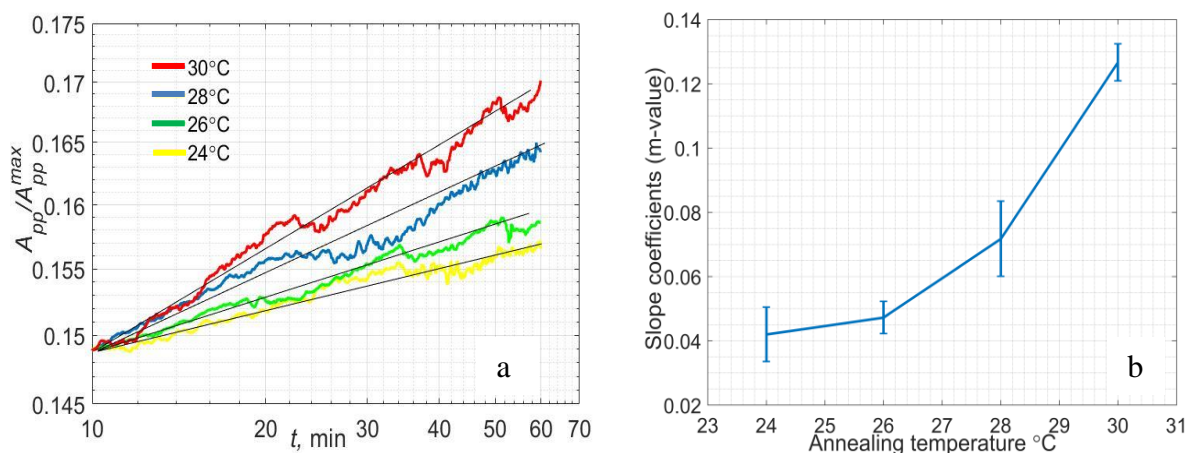
Figure 6-11: (a) the non-linear wave mixing intensity of PVC during physical aging processes as a function of logarithmic time with different annealing temperatures. (b) The annealing temperature dependence of aging slope coefficients as extracted from the aging slope.

When the annealing temperature of the water was increased, aging acceleration also increases. The rate of aging is directly related to molecular mobility and molecular mobility

is tied to the annealing temperature. After quenching, the PVC gradually approaches equilibrium at a fixed annealing temperature. This fixes the polymer mobility and therefore the aging rate. From Figure 6-11(b), it is clearly seen that when the annealing temperature increases this leads to an increase in the aging rate. The non-linear wave mixing slope coefficient was about 0.042 (in arbitrary units of amplitude per time) at annealed temperature of 24 °C, with an exponential increase with annealing temperature, reaching 0.126 (in arbitrary units of amplitude per time) at 30 °C.

6.3.2.5 The comparison of experiment and theoretical model

The accelerated physical aging in PVC sheets shown in Figure 6-11 displayed an exponential increase with increasing annealing temperature. In order to confirm the experimental result, a comparison with a model is needed. The Arrhenius model (commonly used in physics and science research) is introduced for the evaluation of physical aging and to provide a comparison of the results. The Arrhenius equation is used to describe the temperature dependence of the acceleration constant for an elementary chemical reaction (Petrou, Roulia and Tampouris, 2002).

$$k_a = exp\left(-\frac{E_a}{RT}\right)$$

(6.1)

where E_a is the Arrhenius activation energy, R is the gas constant (8.314 J×mol^{-1}×K^{-1}), k_a is the Arrhenius rate constant, and T is the absolute aging temperature in Kelvin. The activation energy is the energy required for the macroscopic reaction to occur and is the kinetic energy the molecules need to have to overcome bonding. In order to validate the experimental results with the Arrhenius model, the E_a value must be estimated by using the real value from the experimental results. Then values from the Arrhenius model can be calculated. The (k_a) constants were calculated by Equation (6.1) and then the initial activation energy is assumed to be 300 kJ/mol that is close to the value presented by (Bauwens-Crowet et $al.$, 1969). The calculation results are showed in Table 6-1. When the annealing temperature can perform by controlling the water temperature in the chamber, the annealed temperature is in lower range between 24°C to 30 °C with 2 °C for a step.

Table 6-1: The experimental results from the non-linear wave mixing technique and calculated constants from the Arrhenius model.

Annealing (°C)	24	26	28	30
Experiment (k_e)	0.042	0.0473	0.0718	0.1267
Arrhenius model (k_m)	12.56	21.59	36.88	62.46

The data from the table was used to determine the activation energy by minimizing the objective function.

$$\text{objective function } = \min \sum (k_e - k_m)^2 \tag{6.2}$$

After minimization by Equation (6.2), the result of minimum E_a was 377 kJ/mol. This value is consistent with the value of 318 kJ/mol found in the literature (Havriliak and Shortridge, 1989). So then, the estimated value of the activation energy, 377 kJ/mol, was substituted to Equation (6.1) for finding k_a as a function of temperature.

The comparative results from non-linear ultrasonic wave mixing and Arrhenius model are shown in Figure 6-12: showing the result calculated by the model are plotted and superimposed to the non-linear wave mixing curve (red line). When active energy of 300 kJ/mol was used for calculation (the assumed value), the model is rather unsatisfactory as shown in (a). The modeling curve showed a tendency to rise at the initial temperature where
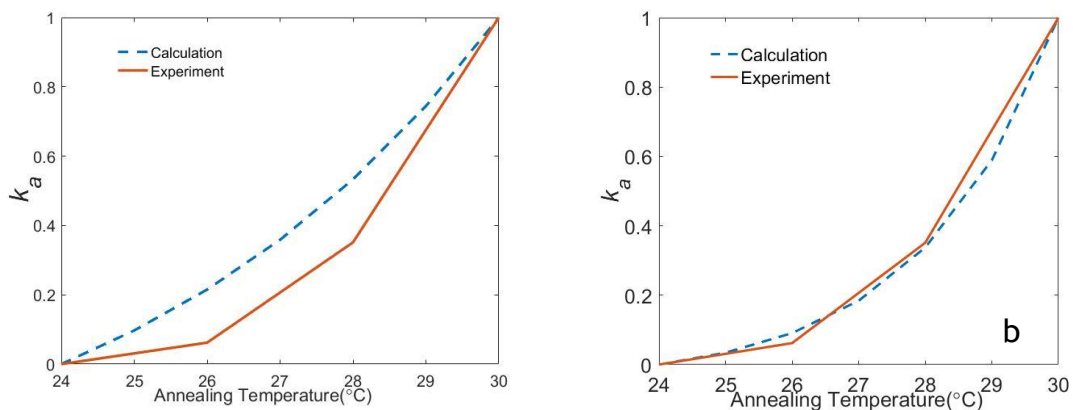
Figure 6-12: The comparison between the theoretical model and non-linear ultrasonic wave mixing data. (a) when activation energy E_a of 300 kJ/mol. (b) the activation energy of 377 kJ/mol.

the experiment data start slowly increases at 26 °C. However, both curves increase with increasing annealing temperature.The calculated result shows very good agreement with experimental data as shown in (b), using an activation energy of 377 kJ/mol. The modeling results are similar to the experimental data, with only a minor difference at annealing temperatures around 29 °C.

Havriliak and Shortridge (1989) evaluated the effect of the k-constant value when the tensile stress experiment was performed on PVC specimen and the yield stress was measured. The results of their experiments showed that an activation energy of 76 kcal/mol (318 kJ/mol) is consistent with the observed yield stress for annealing temperatures from -40 °C to 25 °C.

The results of our experimental study are in good agreement with the Arrhenius model as shown in Figure 6-12(b), and indicate an activation energy of 377kJ/mol, nearly equal to the energy of 318 kJ/mol as cited in (Havriliak and Shortridge, 1989). It should be noted that for higher annealing temperatures, the activation energy can be lower. Havriliak and Shortridge, (1989) found that the activation energy of kinetic aging of uPVC at an annealing temperature of at 65 °C was 115kJ/mol.

6.4 Summary

The non-collinear ultrasonic wave mixing based technique using ultrasonic transducers was implemented for physical aging investigation of polyvinylchloride. This behaviour can be observed below the glass transition temperature and significantly affects the polymer's mechanical properties. The system of measurement consists of two transmitters sending an ultrasonic signal to a specimen. The propagated signal from both transducers interacted with each other in the material with specific angles. The result of the interaction was a generated third wave which is used for physical aging detection (receiver). This system was used to evaluate physical aging for a specimen sheet of PVC. First, a specimen was heated in an oven above the glass transition temperature T_g for 60 min and immediately quenched in antifreeze liquid (at -34 °C). The heating step erased the thermo-history of the polymer. The quenched specimen was then placed into a water bath, where two sources, at 2.5 and 3.75 MHz, generated initial waves. The response of the nonlinear sum-frequency interaction was captured with a 30 s sampling rate at 6.25 MHz. The system shows that the nonlinear ultrasonic technique is suitable to detect the physical aging of amorphous polymers at the annealing temperature. When the polymer structure underwent structural relaxation, the nonlinear wave mixing energy gradually increased due to the non-equilibrium state and then continually developed due to physical aging. In addition, the gradient of the nonlinear wave mixing energy increased exponentially with annealing temperatures, showing the potential for high sensitivity. In order to confirm the experimental result, the Arrhenius model was used for comparing with the experimental value of physical aging and the comparison showed that the calculated result is in very good agreement with experiment data as show in Figure 6-12 (b). In summary, this method can be beneficially applied for the evaluation of physical aging due to its high sensitivity to changes in the structural relaxation in polymers and agrees with the physical aging theory.

In addition, the experimental results suggest that this method can detect changing material properties with time dependence, such polymer aging. The behaviors of polymer aging and pressure ulcer formation are the progressive processes with time dependence. In

addition, previous studies have shown that ultrasonic characterization of wound tissue revealed an increase in the velocity of sound as a function of wound age (O'Brien *et al.*, 1981). The behavior of polymer aging and the wound of ulcers are roughly analogous. With further development, nonlinear wave mixing may prove to be an efficient tool to detect pressure ulcer formation.

Chapter 7   Conclusion and Future Prospects

In this chapter, all findings are summarised, potential applications which could be explored in the future, and end with conclusions.

7.1 Summary and conclusion

Nonlinear ultrasonic wave mixing can perform ultrasonic non-destructive testing which has been used for the investigation and characterisation of defects and micro-cracks in material structures. Because of its high sensitivity, nonlinear ultrasonic wave mixing is more powerful than conventional ultrasonic techniques. The characteristic of the system involves the evaluation of additional frequency components occurring when an ultrasonic wave propagates and then interacts with a material's defect. This interaction results in the generation of the frequency components called harmonic frequencies, used for defect identification. These harmonics are the sum and difference frequencies characteristic of nonlinear wave mixing. In contrast, conventional linear methods observe the amplitude and phase of the signal limited to the same excited frequency for measurement in the transmission and reflection signals. There are two categories of wave mixing when considering the incident direction of the transmitted ultrasonic waves: collinear and non-collinear wave mixing. Both types of nonlinear wave mixing have been implemented in this study for the characterisation of materials.

This thesis has successfully applied the concept of nonlinear wave mixing measurement for the detection of a small particle in a hydrogel phantom and the physical investigation of the aging of amorphous thermoplastic polymers. The system consists of three broadband ultrasonic transducers arranged at specific angles in order to achieve a particular interaction mode for the non-collinear wave mixing method, while collinear wave mixing is performed with one transmitter and a receiver transducer (see Chapter 2 and Chapter 3).

In Chapter 4, the second-order nonlinear wave interaction equations were discussed as was their implementation in the MATLAB program for simulation. The numerical results (see Section 6.3.1) show the ten interactions of nonlinear wave mixing. All the simulation cases were carried out including third order material properties representing PVC and agar. Each of the ten cases simulated were shown to have a specific characteristic. Amplitude coefficients (w), the interaction angle (α), and the scattering angle (ψ) , are the parameters of the wave interaction simulation which relate to the frequency ratio (d). These results are

beneficial for the determination of the resonance condition of the two wave interactions in the material. Longitudinal and shear waves are the fundamental waves for the various combinations. The results of case#1 and case#2 (Figure 4-1,2) show that the interaction and scattering angles were zero. Only amplitudes appear for the two collinear waves $L(\omega_1)$ and $L(\omega_2)$ which are mixed. The amplitude coefficients for the simulation of the two collinear waves are related to the third order constants $2m + l$. In non-collinear wave interaction case#3 and case#4, the scattering amplitude is related to m. For case#9 and case#10, the combination of shear horizontal waves depends on the constants m and n. In addition, two of the interaction cases were chosen for specific analysis. The mixing $SV(\omega_1) + L(\omega_2)$ was selected for the analysis of wave interaction for the cases of physical aging, whereas the mixing $L(\omega_1) + L(\omega_2)$ was chosen for the hydrogel material. Both interaction cases are proportional to third order constants that describe the material; however, they depend on different combinations. For example, the interaction $L(\omega_1) + L(\omega_2) \to L(\omega_1 + \omega_2)$ is proportional to $2m + l$ while the other combination is related to the third order constants μ , λ , m such that $SV(\omega_1) + L(\omega_2) \to L(\omega_1 + \omega_2)$ as shown in section 2.3.

In Chapter 6, longitudinal and shear waves were generated in order to achieve the nonlinear interaction case $SV(\omega_1) + L(\omega_2) \to L(\omega_1 + \omega_2)$. In addition, the numerical simulation was conducted to understand how the two waves interact. The simulation details and parameter set up were described in Section 4.3. The visual simulation results indicate clearly where the waves propagated and interacted in the specimen. Not only was the direction of wave travel displayed but the point at which the two waves combined was located. The simulation results were beneficial to have before the experiment was performed as the results illustrate the optimal geometry and configuration of the experimental set up. From the simulation results including the analytical wave interaction, the geometric configuration of the experimental set up was determined and described in Section 3.2. Nonlinear ultrasonic wave mixing was performed in a water chamber to avoid an impedance effect with water circulation system. The result of the interaction of the two incident waves was the generation of a third wave which was then used for the detection of the physical aging of the polymer. The system showed a high correlation between the nonlinear energy as measured by the receiver transducer and the aging processes that occurs after quenching at a fixed annealing temperature. When the polymer structure underwent structural relaxation, the nonlinear wave mixing energy gradually increased due to non-equilibrium effects and then continually developed due to physical aging. In addition, the gradient of the nonlinear wave mixing energy increased exponentially with annealing temperatures, showing the potential for high sensitivity. In order to confirm the experimental result, the

Arrhenius model was used for comparison with the experimental results for physical aging. This comparison showed that the calculated result agrees very well with this experimental data (see Section 4.3.2.5).

The application of nonlinear ultrasonic wave mixing was illustrated in Chapter 5 to investigate the deflection of a small particle distributed in a hydrogel phantom. Collinear wave mixing, a nonlinear wave mixing technique, was implemented by using a moving X_Y stage with the ability to execute a C-scan image. Different driving frequencies of 4.5Mz and 6.75MHz were used to generate a summed frequency used for the evaluation of nonlinearity of the phantom. In order to simulate the deflected signal, different microparticles (70μm, 100μm, 150μm) were distributed in the tissue phantom, which was made from NIPAM hydrogel. This kind of gel has many advantages for this work, such as simple preparation, transparency of the material and acoustic properties similar to those of human muscle. These properties of the gel were verified using the phase velocity and attenuation method. From the C-scan of the collinear wave mixing it can be clearly seen that the nonlinear wave signal can detect the small particles by deflection. The advantage of the nonlinear wave mixing method was demonstrated by direct comparison with results from the linear ultrasound technique, revealing higher sensitivities and better resolution than the linear pulse echo ultrasound method. The results of a C-scan of the nonlinear signal provide evidence that the high-resolution image of the deflected small particle can be measured by the collinear wave mixing technique. In addition, the vibration of the particles in the hydrogel phantom was detected by the collinear wave mixing technique with zoomed-in C-scan image.

7.2   Future prospects

Future applications of the nonlinear wave mixing technique may be applied to a pressure ulcer mimicking phantom designed to simulate the early stages of pressure ulcer growth. The tissue phantom designed for particle detection, as described in Section 5.2.2, can be changed to mimic a deep tissue injury phantom. This phantom might have three areas which can represent: a bone, a region representing a developing pressure ulcer, and the neighbouring healthy tissue.

7.2.1 Deep tissue injury phantom

The tissue phantom used in Chapter 5 to study the deflection of small particles only represents the nonlinearity of the material from various sizes of particles. However, it does not address how the injury develops. In the case of deep pressure ulcers, the tissue injury

develops in the deep muscle layer under bony prominences which results in a continued compression of the tissue. The development process of the deep injury under the surface provides important information on local tissue properties. To observe the deep tissue injury, the phantom might be set up as shown in Figure 7-1. The phantom should have the correct mechanical properties to represent three regions: bone, ulcer and healthy tissue. For instance, the Young's modulus of bone, ulcer and tissue are 10 GPa, 90 kPa and 50 kPa respectively (Deprez *et al.*, 2011). Additionally, the compressed force on the bone area is a main factor in the development of a deep pressure ulcer. Therefore, this compression should be implemented in the phantom to adequately mimic the deep-surface pressure ulcer behaviour.
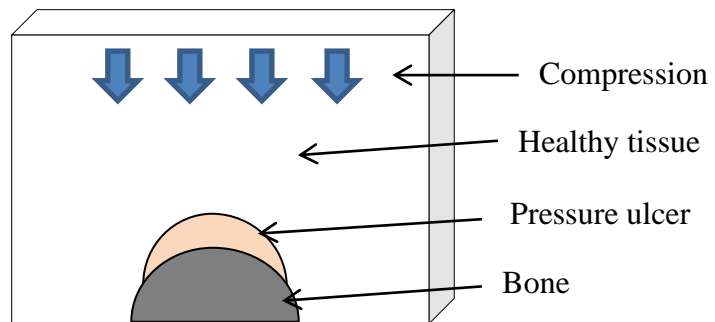
Figure 7-1: A schematic diagram of the deep tissue injury phantom, which would simulate the deep tissue injury and allow study of the development of the deep tissue injury.

7.2.2 Collinear wave mixing with a burst delay time

The implemented collinear wave mixing technique described in Section 5.2 has a fixed intersection of the two waves. It does not allow the interaction position to be adjusted along the length of specimen, as both driving waves were mixed in the same transmitter transducer to generate the nonlinear wave mixing combination. The use of two transducers located on opposite sides of the specimen would permit this (see Figure 7-2). Transducer #1 is both a transmitter and a receiver. In order to separate the high voltage driving signal from power amplifier and the echo signal from receiver, the preamplifier should have the ability to block the high voltage from the power amplifier so that the input state of preamplifier might be a high voltage protection circuit (Choi *et al.*, 2014). This system can allow the intersection of wave mixing to occur at different locations throughout the specimen. This would permit scanning the whole specimen with the nonlinear wave mixing signal.
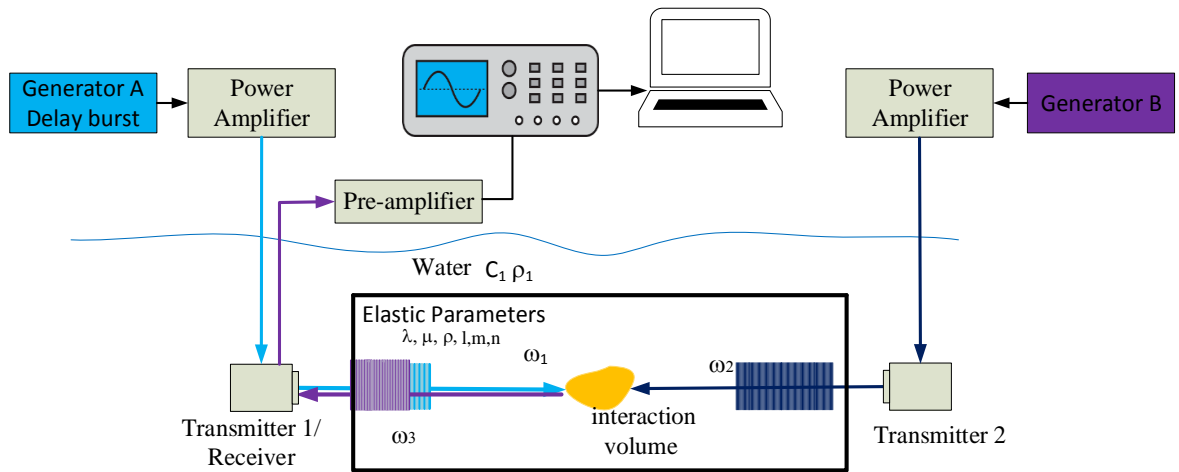
Figure 7-2: The schematic diagram of collinear wave mixing with adjustable delay burst time. The excited transducers are located on opposite sides, but one of them is also used to receive the echo signal and then pass through the preamplifier. The position where the two waves (ω_1 and ω_2) interact can be changed by adjusting the delay time for stimulating transmitter1.

7.2.3 High intensity focusing ultrasound for physical aging

For the physical aging, the specimen used for evaluation must be heated in order to allow the annealing processes. The specimen is generally incubated at a temperature above T_g, before the measurement. Moving the specimen between an oven and the measurement place is not convenient. It would be better to avoid the need to move the specimen from the measurement location. The measurement system should be able to perform both heating and detecting the physical aging by focusing the heat to a specific point in a specimen and then continuously evaluating the physical aging.

High intensity focused ultrasound (HIFU) involves focused ultrasound in which energy is focused into a small area for heating and abolishing the target. The intensity of ultrasound is related to the heat admission resulting from absorbed ultrasonic energy in the medium along the propagation distance. The heat sources can be calculated by using the nonlinear parabolic Khokhlov-Zabolotskaya-Kuznetsov (KZK) equation which has been described in (Fan *et al.*, 2017; Canney *et al.*, 2010). Therefore, the temperature in the material can be estimated in the heating processes. In this, HIFU can remotely penetrate to heat the material, focused on the local area. The HIFU with physical aging measurement system is shown in Figure 7-3. The system combines the non-linear wave mixing technique with HIFU for heating the polymer specimen. The wave mixing setup was described in Chapter 3, with the addition of a receiver and HIFU generator in a single transducer. The measurement processes start with HIFU induction of heat in a specimen to evoke the aging processes, then the non-linear wave mixing measurement is performed.
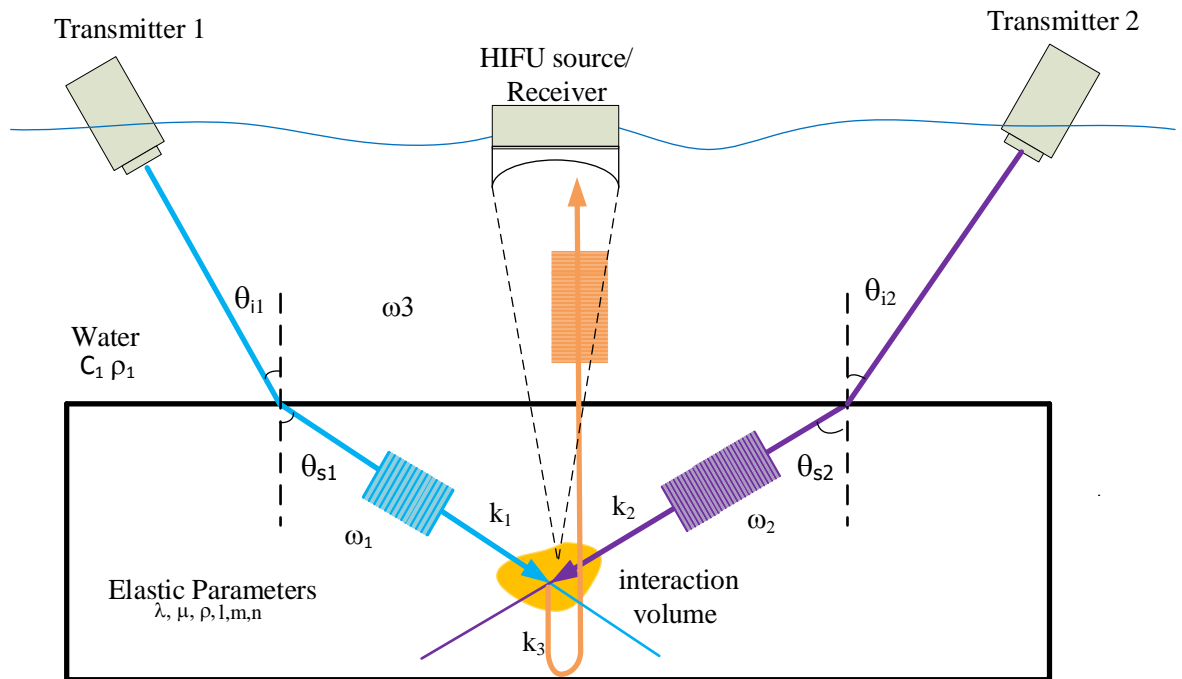
Figure 7-3: HIFU for thermal annealing temperature for physical aging measurement. The transducer 1 and 2 perform non-linear wave mixing whereas another transducer functions as both receiver and heat generator.

The high intensity focused ultrasound usually uses ultrasonic frequency more than 200 kHz with intensity between 1000-10000 W/cm^2, to ensure sufficient thermal effect (Fei *et al.*, 2018)(Liu *et al.*, 2013). When the ultrasonic wave propagates through viscoelastic polymer materials, they absorb ultrasonic energy via the particles in the polymer, inducing the heating effect (Price, White and Clifton, 1995). This mechanism results from cavitation, the fast increase and collapse of the particles of polymer, resulting not only in a generated shock wave but also producing shearing oscillation in the polymer structure. Those mechanisms cause vibration of the polymer chain in a restricted area, resulting in the generation of heat. Fei *et al.*,(2018) demonstrated the use of HIFU to increase the temperature of an amorphous polyethylene terephthalate (PET) specimen. They show that 2W of HIFU at 1.1 MHz with a diameter of 64.0mm and focal length of 62.6 mm can induce the temperature of PET increase to the Tg of PET (at 87.9 °C). This knowledge would be useful for applying physical aging measurement, especially for localized annealing processes.

References

Van Den Abeele, K. E. A., Carmeliet, J., Ten Cate, J. A. and Johnson, P. A. (2000) 'Nonlinear elastic wave spectroscopy (NEWS) techniques to discern material damage, Part II: Single-mode nonlinear resonance acoustic spectroscopy', *Research in Nondestructive Evaluation*, 12(1), pp. 31–42.

Van Den Abeele, K. E. A., Johnson, P. A. and Sutin, A. (2000) 'Nonlinear elastic wave spectroscopy (NEWS) techniques to discern material damage, Part I: Nonlinear wave modulation spectroscopy (NWMS)', *Research in Nondestructive Evaluation*, 12(1), pp. 17–30.

Ben Amar, M. (2018) 'Nonlinear visco-elasticity of soft tissues under cyclic deformations', *International Journal of Non-Linear Mechanics*, 106, pp. 238–244. doi: https://doi.org/10.1016/j.ijnonlinmec.2018.07.002.

ASTM committee D20 (2003) 'Standard practice for heat aging of of plastics without load', *ASTM International*.

Banerjee, S., Kundu, T. and Alnuaimi, N. A. (2007) 'DPSM technique for ultrasonic field modelling near fluid–solid interface', *Ultrasonics*, 46(3), pp. 235–250. doi: http://dx.doi.org/10.1016/j.ultras.2007.02.003.

Bauwens-Crowet, C., Bauwens, J. C. and Homès, G. (1969) 'Tensile yield-stress behavior of glassy polymers', *Journal of Polymer Science Part A-2: Polymer Physics*. John Wiley & Sons, Ltd, 7(4), pp. 735–742. doi: 10.1002/pol.1969.160070411.

Bennett, G., Dealey, C. and Posnett, J. (2004) 'The cost of pressure ulcers in the UK', *Age and Ageing*, 33(3), pp. 230–235. doi: 10.1093/ageing/afh086.

Beyer, R. T. (1960) 'Parameter of nonlinearity in fluids', *The Journal of the Acoustical Society of America*. Acoustical Society of America, 32(6), pp. 719–721. doi: 10.1121/1.1908195.

Bjørnø, L. (1986) 'Characterization of biological media by means of their non-linearity', *Ultrasonics*, 24(5), pp. 254–259. doi: https://doi.org/10.1016/0041-624X(86)90102-2.

Bjørnø, L. (2010) 'Introduction to nonlinear acoustics', *Physics Procedia*, 3(1), pp. 5–16. doi: https://doi.org/10.1016/j.phpro.2010.01.003.

Cangialosi, D., Boucher, V. M. and Alegría, A. (2013) 'Physical aging in polymers and polymer nanocomposites: recent results and open questions', *Soft Matter*. The Royal Society of Chemistry, 9(36), pp. 8619–8630. doi: 10.1039/C3SM51077H.

Canney, M. S., Khokhlova, V. A., Bessonova, O. V, Bailey, M. R. and Crum, L. A. (2010) 'Shock-induced heating and millisecond boiling in gels and tissue due to high intensity focused ultrasound', *Ultrasound in medicine & biology*. 2009/12/16, 36(2), pp. 250–267. doi: 10.1016/j.ultrasmedbio.2009.09.010.

Cao, Y., Li, G.-Y., Zhang, X. and Liu, Y.-L. (2017) 'Tissue-mimicking materials for elastography phantoms: A review', *Extreme Mechanics Letters*, 17(Supplement C), pp. 62–70. doi: https://doi.org/10.1016/j.eml.2017.09.009.

Catheline, S., Gennisson, J.-L. and Fink, M. (2003) 'Measurement of elastic nonlinearity of soft solid with transient elastography', *The Journal of the Acoustical Society of America*. Acoustical Society of America, 114(6), pp. 3087–3091. doi: 10.1121/1.1610457.

Chan, K. M., Mushahwar, V. K., Ho, C. and Dukelow, S. p. (2015) 'Insights from prevention of deep pressure ulcers', in Kilgore, K. (ed.) *Implantable Neuroprostheses for Restoring Function*. 1st Editio. 26th February 2015, pp. 267–280.

Changping, Z., Minglei, S., Shichuan, H., *et al.* (2004) 'Sound intensity measurement in focal region of HIFU transducer adopting narrow-pulse method', in *2004 IEEE International Conference on Industrial Technology, 2004. IEEE ICIT '04.*, pp. 1374-1377 Vol. 3. doi: 10.1109/ICIT.2004.1490761.

Choi, H., Kim, M. G., Cummins, T. M., Hwang, J. Y. and Shung, K. K. (2014) 'Power MOSFET–Diode–Based limiter for high-frequency ultrasound systems', *Ultrasonic Imaging*. SAGE Publications Inc, 36(4), pp. 317–330. doi: 10.1177/0161734614524180.

Choi, M. J., Guntur, S. R., Lee, K. I. L., Paeng, D. G. and Coleman, A. (2013) 'A tissue mimicking polyacrylamide hydrogel phantom for visualizing thermal lesions generated by high intensity focused ultrasound', *Ultrasound in Medicine & Biology*, 39(3), pp. 439–448. doi: https://doi.org/10.1016/j.ultrasmedbio.2012.10.002.

Cortela, G., Benech, N., Pereira, W. C. A. and Negreira, C. (2015) 'Characterization of acoustical properties of a phantom for soft tissues (PVCP and Graphite Powder) in the range 20 - 45°C', *Physics Procedia*, 70, pp. 179–182. doi: https://doi.org/10.1016/j.phpro.2015.08.107.

Courtney, C. R. P., Drinkwater, B. W., Neild, S. A. and Wilcox, P. D. (2008) 'Factors affecting the ultrasonic intermodulation crack detection technique using bispectral analysis', *NDT & E International*. Elsevier, 41(3), pp. 223–234. doi: 10.1016/J.NDTEINT.2007.09.004.

Courtney, C. R. P., Neild, S. A., Wilcox, P. D. and Drinkwater, B. W. (2010) 'Application of the bispectrum for detection of small nonlinearities excited sinusoidally', *Journal of Sound and Vibration*. Academic Press, 329(20), pp. 4279–4293. doi: 10.1016/J.JSV.2010.04.031.

Croxford, A. J., Wilcox, P. D., Drinkwater, B. W. and Nagy, P. B. (2009) 'The use of non-collinear mixing for nonlinear ultrasonic detection of plasticity and fatigue', *J. Acoust. Soc. Am.*, 126, p. EL117.

Cugini, A. (2015) *Aspects of Physical Aging and Solid State Processing of Polymeric Glasses*. University of Massachusetts - Amherst. Available at: https://scholarworks.umass.edu/dissertations_2/425.

Culjat, M. O., Goldenberg, D., Tewari, P. and Singh, R. S. (2010) 'A Review of tissue

substitutes for ultrasound imaging', *Ultrasound in Medicine & Biology*, 36(6), pp. 861–873. doi: https://doi.org/10.1016/j.ultrasmedbio.2010.02.012.

Demčenko, A., Ravanan, M., Visser, H. A., Loendersloot, R. and Akkerman, R. (2012) 'Investigation of PVC physical ageing in field test specimens using ultrasonic and dielectric measurements', in *2012 IEEE International Ultrasonics Symposium*, pp. 1909–1912. doi: 10.1109/ULTSYM.2012.0479.

Demčenko, A., Akkerman, R., Nagy, P. B. and Loendersloot, R. (2012) 'Non-collinear wave mixing for non-linear ultrasonic detection of physical ageing in PVC', *NDT & E Int.*, 49, p. 34.

Demčenko, A., Mazilu, M., Reboud, J. and Cooper, J. M. (2019) 'Green-function Method for Nonlinear Interactions of Elastic Waves', in *2019 IEEE International Ultrasonics Symposium (IUS)*, pp. 1859–1861. doi: 10.1109/ULTSYM.2019.8926192.

Demčenko, A., Koissin, V. and Korneev, V. A. (2014) 'Noncollinear wave mixing for measurement of dynamic processes in polymers: Physical ageing in thermoplastics and epoxy cure', *Ultrasonics*, 54(2), pp. 684–693. doi: http://dx.doi.org/10.1016/j.ultras.2013.09.011.

Deprez, J.-F., Brusseau, E., Fromageau, J., Cloutier, G. and Basset, O. (2011) 'On the potential of ultrasound elastography for pressure ulcer early detection', *Medical Physics*, 38(4), pp. 1943–1950. doi: doi:http://dx.doi.org/10.1118/1.3560421.

Destrade, M., Gilchrist, M. D. and Saccomandi, G. (2010) 'Third- and fourth-order constants of incompressible soft solids and the acousto-elastic effect', *The Journal of the Acoustical Society of America*. Acoustical Society of America, 127(5), pp. 2759–2763. doi: 10.1121/1.3372624.

Donskoy, D., Sutin, A. and Ekimov, A. (2001) 'Nonlinear acoustic interaction on contact interfaces and its use for nondes tructive testing', *NDT & E International*, 34(4), pp. 231–238. doi: https://doi.org/10.1016/S0963-8695(00)00063-3.

Drzeżdżon, J., Jacewicz, D., Sielicka, A. and Chmurzyński, L. (2019) 'Characterization of polymers based on differential scanning calorimetry based techniques', *TrAC Trends in Analytical Chemistry*, 110, pp. 51–56. doi: https://doi.org/10.1016/j.trac.2018.10.037.

Duffour, P., Morbidini, M. and Cawley, P. (2006) 'A study of the vibro-acoustic modulation technique for the detection of cracks in metals', *The Journal of the Acoustical Society of America*. Acoustical Society of America, 119(3), pp. 1463–1475. doi: 10.1121/1.2161429.

Dunn, F. (1986) 'The ultrasonic nonlinearity parameter of biological media and its dependence on tissue structure', *Ultrasound in Medicine & Biology*, 12(9), pp. 701–702. doi: https://doi.org/10.1016/0301-5629(86)90286-3.

Ediguer, F. E., A. Brizzotti Andrade, M., Tokio Higuti, R., C. Adamowski, J. and Buiochi, F. (2006) 'Acoustic trasnsmission with mode conversion phenomenon', *ABMC Sympsium Series in Mechatronics*, 2, pp. 113–120.

Egle, D. M. and Bray, D. E. (1976) 'Measurement of acoustoelastic and third-order elastic constants for rail steel', *The Journal of the Acoustical Society of America*. Acoustical Society of America, 60(3), pp. 741–744. doi: 10.1121/1.381146.

Erkamp, R. Q., Skovoroda, A. R., Emelianov, S. Y. and O'Donnell, M. (2004) 'Measuring the nonlinear elastic properties of tissue-like phantoms', *IEEE Transactions on Ultrasonics, Ferroelectrics, and Frequency Control*, 51(4), pp. 410–419. doi: 10.1109/TUFFC.2004.1295426.

Escobar-Ruiz, E., Ruiz, A., Hassan, W., *et al.* (2014) 'Non-linear ultrasonic NDE of titanium diffusion bonds', *Journal of Nondestructive Evaluation*, 33(2), pp. 187–195. doi: 10.1007/s10921-013-0217-5.

Fairhurst, A., Thommen, M. and Rytka, C. (2019) 'Comparison of short and long term creep testing in high performance polymers', *Polymer Testing*, 78, p. 105979. doi: https://doi.org/10.1016/j.polymertesting.2019.105979.

Fan, T., Chen, T., Zhang, W., Hu, J., Zhang, Y. and Zhang, D. (2017) 'Acoustic characterization of high intensity focused ultrasound field generated from a transmitter with large aperture', *AIP Conference Proceedings*. American Institute of Physics, 1821(1), p. 180002. doi: 10.1063/1.4977665.

Fatemi, M. and Greenleaf, J. F. (1998) 'Ultrasound-stimulated vibro-acoustic spectrography', *Science*, 280(5360), pp. 82 LP – 85. doi: 10.1126/science.280.5360.82.

Fei, G., Pu, X., Zhuang, T., Liu, B., Wang, Z. and Xia, H. (2018) 'High-intensity focused ultrasound selective annealing induced patterned and gradient crystallization behavior of polymer', *Ultrasonics Sonochemistry*, 40, pp. 442–452. doi: https://doi.org/10.1016/j.ultsonch.2017.07.036.

Ferguson-Pell, M. (2005) *Imaging tissues for pressure ulcer prevention*, *Pressure Ulcer Research: Current and Future Perspectives*. doi: 10.1007/3-540-28804-X_17.

Fonseca, M., Zeqiri, B., Beard, P. C. and Cox, B. T. (2016) 'Characterisation of a phantom for multiwavelength quantitative photoacoustic imaging', *Physics in Medicine and Biology*. IOP Publishing, 61(13), pp. 4950–4973. doi: 10.1088/0031-9155/61/13/4950.

Franco, E. E., Brizzotti Andrade, M. A., Tokio Higuti, R., Adamowski, J. C. and Buiochi, F. (2006) 'Acoustic transmission with mode conversion phenomenon', in *ABCM Symposium Series in Mechatronics*, pp. 113–120. Available at: http://www.abcm.org.br/symposium-series/SSM_Vol2/antigos/Section_II_Industrial_Instrumentation/SSM2_I_15.pdf.

Fredriksson, I., Larsson, M. and Strömberg, T. (2009) 'Measurement depth and volume in laser Doppler flowmetry', *Microvascular Research*, 78(1), pp. 4–13. doi: https://doi.org/10.1016/j.mvr.2009.02.008.

Fromageau, J., Gennisson, J., Schmitt, C., Maurice, R. L., Mongrain, R. and Cloutier, G. (2007) 'Estimation of polyvinyl alcohol cryogel mechanical properties with four ultrasound elastography methods and comparison with gold standard testings', *IEEE*

Transactions on Ultrasonics, Ferroelectrics, and Frequency Control, 54(3), pp. 498–509. doi: 10.1109/TUFFC.2007.273.

Gedde, U. W., Viebke, J., Leijström, H. and Ifwarson, M. (1994) 'Long-term properties of hot-water polyolefin pipes—a review', *Polymer Engineering & Science*. John Wiley & Sons, Ltd, 34(24), pp. 1773–1787. doi: 10.1002/pen.760342402.

Gefen, A., Gefen, N., Linder-Ganz, E. and Margulies, S. S. (2005) 'In vivo muscle stiffening under bone compression promotes deep pressure sores.', *Journal of biomechanical engineering*. United States, 127(3), pp. 512–524.

Gillen, K. T. and Celina, M. (2016) 'Predicting polymer degradation and mechanical property changes for combined aging enviroments', in *American Chemical Society*, pp. 1–41.

Girija, A. R. (2019) 'Medical applications of polymer/functionalized nanoparticle systems', in Pielichowski, K. and Majka, T. (eds) *Micro and Nano Technologies*. Elsevier, pp. 381–404. doi: https://doi.org/10.1016/B978-0-12-814064-2.00012-3.

Glozman, T. and Azhari, H. (2010) 'A Method for characterization of tissue elastic properties combining ultrasonic computed tomography with elastography', *Journal of Ultrasound in Medicine*, 29(3), pp. 387–398. Available at: http://www.jultrasoundmed.org/content/29/3/387.abstract.

Goldman, R. J. M. D. and Salcido, R. M. D. (2002) 'More than one way to measure a wound: an overview of tools and techniques', *Advances in Skin & Wound Care September/October*, 15(5), pp. 236–243. Available at: http://ovidsp.ovid.com/ovidweb.cgi?T=JS&CSC=Y&NEWS=N&PAGE=fulltext&D=ovftf&AN=00129334-200209000-00011.

Guntur, S. R. and Choi, M. J. (2014) 'An improved tissue-mimicking polyacrylamide hydrogel phantom for visualizing thermal lesions with high-intensity focused ultrasound', *Ultrasound in Medicine & Biology*, 40(11), pp. 2680–2691. doi: https://doi.org/10.1016/j.ultrasmedbio.2014.06.010.

Hadj Henni, A., Schmitt, C., Trop, I. and Cloutier, G. (2012) 'Shear wave induced resonance elastography of spherical masses with polarized torsional waves', *Applied Physics Letters*. American Institute of Physics, 100(13), p. 133702. doi: 10.1063/1.3696300.

Havriliak, J. S. and Shortridge, T. J. (1989) 'Effect of K-Value on the tensile yield properties on poly', *Journal of Applied Polymer Science*, 37, pp. 2827–2836.

He, P. (1998) 'Acoustic parameter estimation based on attenuation and dispersion measurements', in *Proceedings of the 20th Annual International Conference of the IEEE Engineering in Medicine and Biology Society. Vol.20 Biomedical Engineering Towards the Year 2000 and Beyond (Cat. No.98CH36286)*, pp. 775–778 vol.2. doi: 10.1109/IEMBS.1998.745543.

He, P. (2000) 'Measurement of acoustic dispersion using both transmitted and reflected

pulses', *The Journal of the Acoustical Society of America*. Acoustical Society of America, 107(2), pp. 801–807. doi: 10.1121/1.428263.

He, P. and Zheng, J. (2001) 'Acoustic dispersion and attenuation measurement using both transmitted and reflected pulses', *Ultrasonics*, 39(1), pp. 27–32. doi: https://doi.org/10.1016/S0041-624X(00)00037-8.

Higazy, A. A., Kassem, M. E., Kandeil, A. Y. and Zahran, R. R. (1994) 'Ultrasonic characterization, hardness and dielectric properties of γ-irradiated poly vinyl chloride', *Materials Letters*, 20(3–4), pp. 237–244. doi: 10.1016/0167-577X(94)90093-0.

Holt, R. G. and Roy, R. A. (2001) 'Measurements of bubble-enhanced heating from focused, mhz-frequency ultrasound in a tissue-mimicking material', *Ultrasound in Medicine & Biology*, 27(10), pp. 1399–1412. doi: https://doi.org/10.1016/S0301-5629(01)00438-0.

Huang, D., Huang, Y., Xiao, Y., *et al.* (2019) 'Viscoelasticity in natural tissues and engineered scaffolds for tissue reconstruction', *Acta Biomaterialia*. doi: https://doi.org/10.1016/j.actbio.2019.08.013.

Hunkel, M., Surm, H. and Steinbacher, M. (2018) 'Dilatometry', in Vyazovkin, S., Koga, N., and Schick, C. (eds) *Recent Advances, Techniques and Applications*. Elsevier Science B.V., pp. 103–129. doi: https://doi.org/10.1016/B978-0-444-64062-8.00019-X.

Hutchinson, J. M. (1995) 'Physical aging of polymers', *Progress in Polymer Science*, 20(4), pp. 703–760. doi: https://doi.org/10.1016/0079-6700(94)00001-I.

Jan, Y. K., Brienza, D. M., Boninger, M. L. and Brenes, G. (2011) 'Comparison of skin perfusion response with alternating and constant pressures in people with spinal cord injury', *Spinal Cord*. International Spinal Cord Society, 49(1), pp. 136–141. Available at: http://dx.doi.org/10.1038/sc.2010.58.

Jiang, Y., Li, G.-Y., Qian, L.-X., *et al.* (2015) 'Characterization of the nonlinear elastic properties of soft tissues using the supersonic shear imaging (SSI) technique: Inverse method, ex vivo and in vivo experiments', *Medical Image Analysis*, 20(1), pp. 97–111. doi: https://doi.org/10.1016/j.media.2014.10.010.

Jiao, J., Lv, H., He, C. and Bin Wu (2017) 'Fatigue crack evaluation using the non-collinear wave mixing technique', *Smart Materials and Structures*, 26(6), p. 65005. Available at: http://stacks.iop.org/0964-1726/26/i=6/a=065005.

Jin, K., Li, L. and Torkelson, J. M. (2017) 'Bulk physical aging behavior of cross-linked polystyrene compared to its linear precursor: Effects of cross-linking and aging temperature', *Polymer*, 115, pp. 197–203. doi: https://doi.org/10.1016/j.polymer.2017.03.045.

Jingpin, J., Junjun, S., Guanghai, L., Bin, W. and Cunfu, H. (2015) 'Evaluation of the intergranular corrosion in austenitic stainless steel using collinear wave mixing method', *NDT & E International*, 69, pp. 1–8. doi: https://doi.org/10.1016/j.ndteint.2014.09.001.

Jingpin Jiao, Junjun Sun, Nan Li, Guorong Song, Bin Wu and Cunfu He (2014) 'Micro-crack detection using a collinear wave mixing technique', *NDT & E International*, 62, pp. 122–129. doi: https://doi.org/10.1016/j.ndteint.2013.12.004.

Jorba, I., Beltrán, G., Falcones, B., *et al.* (2019) 'Nonlinear elasticity of the lung extracellular microenvironment is regulated by macroscale tissue strain', *Acta Biomaterialia*, 92, pp. 265–276. doi: https://doi.org/10.1016/j.actbio.2019.05.023.

Ju, T., Achenbach, J. D., Jacobs, L. J. and Qu, J. (2017) 'A non-collinear mixing technique to measure the acoustic nonlinearity parameter of an adhesive bond from one side of the sample', *AIP Conference Proceedings*. American Institute of Physics, 1806(1), p. 20011. doi: 10.1063/1.4974552.

Kalfus, J., Detwiler, A. and Lesser, A. J. (2012) 'Probing segmental dynamics of polymer glasses during tensile deformation with dielectric spectroscopy', *Macromolecules*. American Chemical Society, 45(11), pp. 4839–4847. doi: 10.1021/ma202708j.

Kallel, F., Ophir, J., Magee, K. and Krouskop, T. (1998) 'Elastographic Imaging of Low-Contrast Elastic Modulus Distributions in Tissue', *Ultrasound in Medicine and Biology*. Elsevier, 24(3), pp. 409–425. doi: 10.1016/S0301-5629(97)00287-1.

Kmiecik, B., Skotny, A. and Detyna, J. (2017) 'Structure and mechanical properties of soft tissues during selected pathological processes general medicine : Open Access', 5(1), pp. 1–5. doi: 10.4172/2327-5146.1000285.

Knoop, C. and Fritsching, U. (2012) 'Gas/particle interaction in ultrasound agitated gas flow', *Procedia Engineering*, 42, pp. 770–781. doi: https://doi.org/10.1016/j.proeng.2012.07.469.

Koda, S., Yamashita, K., Matsumoto, K. and Nomura, H. (1993) 'Characterization of Polyvinylchloride by means of sound velocity and longitudinal modulus measurements', *Japanese Journal of Applied Physics*. Japan Society of Applied Physics, 32(Part 1, No. 5B), pp. 2234–2237. doi: 10.1143/jjap.32.2234.

Konofagou, E. E. and Hynynen, K. (2003) 'Localized harmonic motion imaging: theory, simulations and experiments', *Ultrasound in Medicine & Biology*, 29(10), pp. 1405–1413. doi: https://doi.org/10.1016/S0301-5629(03)00953-0.

Konofagou, E. E. and Vappou, C. M. and J. (2012) 'Harmonic motion imaging (HMI) for tumor imaging and treatment monitoring', *Current Medical Imaging Reviews*, pp. 16–26. doi: http://dx.doi.org/10.2174/157340512799220616.

Konofagou, E. and Ophir, J. (1998) 'A new elastographic method for estimation and imaging of lateral displacements, lateral strains, corrected axial strains and poisson’s ratios in tissues', *Ultrasound in Medicine and Biology*. Elsevier, 24(8), pp. 1183–1199. doi: 10.1016/S0301-5629(98)00109-4.

Koo, T. K., Cohen, J. H. and Zheng, Y. (2011) 'A mechano-acoustic indentor system for in vivo measurement of nonlinear elastic properties of soft tissue', *Journal of Manipulative and Physiological Therapeutics*, 34(9), pp. 584–593. doi:

https://doi.org/10.1016/j.jmpt.2011.05.009.

Korneev, V. A. and Demčenko, A. (2014) 'Possible second-order nonlinear interactions of plane waves in an elastic solid', *The Journal of the Acoustical Society of America*, 135(2).

Korneev, V. A., Nihei, K. T. and Myer, L. R. (1998) *Nonlinear interaction of plane elastic waves*. California. doi: 10.2172/290877.

Kostek, S., Sinha, B. K. and Norris, A. N. (1993) 'Third-order elastic constants for an inviscid fluid', *The Journal of the Acoustical Society of America*. Acoustical Society of America, 94(5), pp. 3014–3017. doi: 10.1121/1.407336.

Krouskop, T., Wheeler, T., Kallel, F., Garra, B. and Hall, T. (1998) 'The elastic moduli of breast and prostate tissues under compression', *Ultrasonic imaging*, 20, pp. 260–274. doi: 10.1177/016173469802000403.

Kucera, S. A., Felton, L. A. and McGinity, J. W. (2013) 'Physical aging in pharmaceutical polymers and the effect on solid oral dosage form stability', *International Journal of Pharmaceutics*, 457(2), pp. 428–436. doi: https://doi.org/10.1016/j.ijpharm.2013.01.069.

Law, W. K., Frizzell, L. A. and Dunn, F. (1985) 'Determination of the nonlinearity parameter B/A of biological media', *Ultrasound in Medicine & Biology*, 11(2), pp. 307–318. doi: https://doi.org/10.1016/0301-5629(85)90130-9.

Lee, C. C., Lahham, M. and Martin, B. G. (1990) 'Experimental verification of the Kramers-Kronig relationship for acoustic waves', *IEEE Transactions on Ultrasonics, Ferroelectrics, and Frequency Control*, 37(4), pp. 286–294. doi: 10.1109/58.56489.

Lerner, R. M., Huang, S. R. and Parker, K. J. (1990) '"Sonoelasticity" images derived from ultrasound signals in mechanically vibrated tissues', *Ultrasound in Medicine & Biology*, 16(3), pp. 231–239. doi: http://dx.doi.org/10.1016/0301-5629(90)90002-T.

Li, N., Sun, J., Jiao, J., Wu, B. and He, C. (2016) 'Quantitative evaluation of micro-cracks using nonlinear ultrasonic modulation method', *NDT & E International*, 79, pp. 63–72. doi: https://doi.org/10.1016/j.ndteint.2015.12.003.

Liao, F., Burns, S. and Jan, Y.-K. (2013) 'Skin blood flow dynamics and its role in pressure ulcers', *Journal of Tissue Viability*, 22(2), pp. 25–36. doi: http://dx.doi.org/10.1016/j.jtv.2013.03.001.

Lienhard, J. H. (2010) 'Heat transfer', *Journal of Heat Transfer*, 82(1), p. 198. doi: 10.1115/1.3246887.

Liu, B., Xia, H., Fei, G., Li, G. and Fan, W. (2013) 'High-Intensity Focused Ultrasound-Induced Thermal Effect for Solid Polymer Materials', *Macromolecular Chemistry and Physics*. John Wiley & Sons, Ltd, 214(22), pp. 2519–2527. doi: 10.1002/macp.201300320.

Liu, M., Tang, G., Jacobs, L. J. and Qu, J. (2012) 'Measuring acoustic nonlinearity parameter using collinear wave mixing', *Journal of Applied Physics*. American Institute of

Physics, 112(2), p. 24908. doi: 10.1063/1.4739746.

Liu, X., Li, J., Gong, X., Zhu, Z. and Zhang, D. (2007) 'Theoretical and experimental study of the third-order nonlinearity parameter C/A for biological media', *Physica D: Nonlinear Phenomena*, 228(2), pp. 172–178. doi: https://doi.org/10.1016/j.physd.2007.03.007.

Luboz, V., Petrizelli, M., Bucki, M., Diot, B., Vuillerme, N. and Payan, Y. (2014) 'Biomechanical modeling to prevent ischial pressure ulcers', *Journal of Biomechanics*, 47(10), pp. 2231–2236. doi: http://dx.doi.org/10.1016/j.jbiomech.2014.05.004.

Madsen, E. L., Zagzebski, J. A., Banjavie, R. A. and Jutila, R. E. (2018) 'Tissue mimicking materials for ultrasound phantoms', *Medical Physics*. Wiley-Blackwell, 5(5), pp. 391–394. doi: 10.1118/1.594483.

Mak, A. F. T., Zhang, M. and Tam, E. W. C. (2010) 'Biomechanics of pressure ulcer in body tissues interacting with external forces during locomotion.', *Annual review of biomedical engineering*. United States, 12, pp. 29–53. doi: 10.1146/annurev-bioeng-070909-105223.

Manorama, A. A., Baek, S., Vorro, J., Sikorskii, A. and Bush, T. R. (2010) 'Blood perfusion and transcutaneous oxygen level characterizations in human skin with changes in normal and shear loads — Implications for pressure ulcer formation', *Clinical Biomechanics*, 25(8), pp. 823–828. doi: https://doi.org/10.1016/j.clinbiomech.2010.06.003.

Marston, P. L. (2006) 'Axial radiation force of a Bessel beam on a sphere and direction reversal of the force', *The Journal of the Acoustical Society of America*. Acoustical Society of America, 120(6), pp. 3518–3524. doi: 10.1121/1.2361185.

Marston, P. L. (2007) 'Acoustic beam scattering and excitation of sphere resonance: Bessel beam example', *The Journal of the Acoustical Society of America*. Acoustical Society of America, 122(1), pp. 247–252. doi: 10.1121/1.2735810.

Mihai, L. A. and Goriely, A. (2017) 'How to characterize a nonlinear elastic material? A review on nonlinear constitutive parameters in isotropic finite elasticity', *Proceedings. Mathematical, physical, and engineering sciences*. 2017/11/29. The Royal Society Publishing, 473(2207), p. 20170607. doi: 10.1098/rspa.2017.0607.

Mohabuth, M., Khanna, A., Hughes, J., Vidler, J., Kotousov, A. and Ng, C.-T. (2019) 'On the determination of the third-order elastic constants of homogeneous isotropic materials utilising Rayleigh waves', *Ultrasonics*, 96, pp. 96–103. doi: https://doi.org/10.1016/j.ultras.2019.02.006.

Murnaghan, F. D. (1937) 'Finite Deformations of an Elastic Solid', *American Journal of Mathematics*. Johns Hopkins University Press, 59(2), pp. 235–260. doi: 10.2307/2371405.

Nouman, M., Saunier, J., Jubeli, E. and Yagoubi, N. (2017) 'Additive blooming in polymer materials: Consequences in the pharmaceutical and medical field', *Polymer Degradation and Stability*, 143, pp. 239–252. doi: https://doi.org/10.1016/j.polymdegradstab.2017.07.021.

Novak, A., Bentahar, M., Tournat, V., El Guerjouma, R. and Simon, L. (2012) 'Nonlinear acoustic characterization of micro-damaged materials through higher harmonic resonance analysis', *NDT & E International*, 45(1), pp. 1–8. doi: https://doi.org/10.1016/j.ndteint.2011.09.006.

O'Brien, W. D., Olerud, J., Shung, K. K. and Reid, J. M. (1981) 'Quantitative acoustical assessment of wound maturation with acoustic microscopy', *The Journal of the Acoustical Society of America*. Acoustical Society of America, 69(2), pp. 575–579. doi: 10.1121/1.385432.

O'Donnell, M., Mimbs, J. W. and Miller, J. G. (1981) 'Relationship between collagen and ultrasonic backscatter in myocardial tissue', *The Journal of the Acoustical Society of America*. Acoustical Society of America, 69(2), pp. 580–588. doi: 10.1121/1.385433.

Oberai, A. A., Gokhale, N. H., Goenezen, S., *et al.* (2009) 'Linear and nonlinear elasticity imaging of soft tissuein vivo: demonstration of feasibility', *Physics in Medicine and Biology*. IOP Publishing, 54(5), pp. 1191–1207. doi: 10.1088/0031-9155/54/5/006.

Ophir, J., Céspedes, I., Ponnekanti, H., Yazdi, Y. and Li, X. (1991) 'Elastography: A quantitative method for imaging the elasticity of biological tissues', *Ultrasonic Imaging*, 13(2), pp. 111–134. doi: 10.1177/016173469101300201.

Orsted, H., Ohura, T. and Harding, K. (2010) 'Pressure,shear,friction and microclimate in context', *International review Pressure ulcer prevention*.

Parker, K. J., Doyley, M. M. and Rubens, D. J. (2010) 'Imaging the elastic properties of tissue: the 20 year perspective', *Physics in Medicine and Biology*. IOP Publishing, 56(1), pp. R1–R29. doi: 10.1088/0031-9155/56/1/r01.

Perepechko, I. I. and Golub, P. D. (1973) 'Viscoelastic parameters of certain polymers in the temperature interval 4.2–240°K', *Polymer Mechanics*, 9(4), pp. 534–538.

Petrou, A. L., Roulia, M. and Tampouris, K. (2002) 'The use of the arrhenius equation in the study of deterioration and of cooking of foods - some scientific and pedagogic aspects', *Chemistry Education Research and Practice*. The Royal Society of Chemistry, 3(1), pp. 87–97. doi: 10.1039/B1RP90042K.

Pouet, B. and Rasolofosaon, N. J. P. (1989) 'Ultrasonic intrinsic attenuation measurement using laser techniques', in *Proceedings., IEEE Ultrasonics Symposium,* pp. 545–549 vol.1. doi: 10.1109/ULTSYM.1989.67044.

Price, G. J., White, A. J. and Clifton, A. A. (1995) 'The effect of high-intensity ultrasound on solid polymers', *Polymer*, 36(26), pp. 4919–4925. doi: https://doi.org/10.1016/0032-3861(96)81616-8.

Rajagopal, S., Sadhoo, N. and Zeqiri, B. (2015) 'Reference characterisation of sound speed and attenuation of the IEC agar-based tissue-mimicking material up to a frequency of 60 MHz', *Ultrasound in Medicine & Biology*, 41(1), pp. 317–333. doi: https://doi.org/10.1016/j.ultrasmedbio.2014.04.018.

Read, B. E., Dean, G. D., Tomlins, P. E. and Lesniarek-Hamid, J. L. (1992) 'Physical ageing and creep in PVC', *Polymer*, 33(13), pp. 2689–2698. doi: https://doi.org/10.1016/0032-3861(92)90439-4.

Reger, S., Ranganathan, V., Orsted, H., Ohura, T. and Gefen, A. (2010) 'Shear and friction in context', *International review Pressure ulcer prevention*, pp. 11–18.

Ricco, T. and Smith, T. L. (1990) 'Rate of physical aging of polycarbonate at a constant tensile strain', *Journal of Polymer Science Part B: Polymer Physics*. John Wiley & Sons, Ltd, 28(4), pp. 513–520. doi: 10.1002/polb.1990.090280406.

Rogers, P. H. and Van Buren, A. L. (1974) 'An exact expression for the Lommel-diffraction correction integral', *The Journal of the Acoustical Society of America*. Acoustical Society of America, 55(4), pp. 724–728. doi: 10.1121/1.1914589.

Sachse, W. and Pao, Y. H. (1978) 'On the determination of phase and group velocities of dispersive waves in solids', *Journal of Applied Physics*, 49(8), pp. 4320–4327. doi: 10.1063/1.325484.

Sandrin, L., Tanter, M., Gennisson, J. L., Catheline, S. and Fink, M. (2002) 'Shear elasticity probe for soft tissues with 1-D transient elastography', *IEEE Transactions on Ultrasonics, Ferroelectrics, and Frequency Control*, 49(4), pp. 436–446. doi: 10.1109/58.996561.

Schäfer, G., Dobos, G., Lünnemann, L., Blume-Peytavi, U., Fischer, T. and Kottner, J. (2015) 'Using ultrasound elastography to monitor human soft tissue behaviour during prolonged loading: A clinical explorative study', *Journal of Tissue Viability*, 24(4), pp. 165–172. doi: http://dx.doi.org/10.1016/j.jtv.2015.06.001.

Schelkanova, I., Pandya, A., Muhaseen, A., Saiko, G. and Douplik, A. (2015) 'Early optical diagnosis of pressure ulcers', in *Woodhead Publishing Series in Biomaterials*. Woodhead Publishing, pp. 347–375. doi: http://dx.doi.org/10.1016/B978-0-85709-662-3.00013-0.

Shieh, J., Chen, S.-R., Chen, G.-S., *et al.* (2014) 'Acrylic acid controlled reusable temperature-sensitive hydrogel phantoms for thermal ablation therapy', *Applied Thermal Engineering*, 62(2), pp. 322–329. doi: https://doi.org/10.1016/j.applthermaleng.2013.09.021.

Sinkus, R., Bercoff, J., Tanter, M., *et al.* (2006) 'Nonlinear viscoelastic properties of tissue assessed by ultrasound', *IEEE Transactions on Utrasonics, Ferroelectrics, and Frequency Control*, 53(11), pp. 2009–2018. doi: 10.1109/TUFFC.2006.141.

Struik, L. C. E. (1977) 'Physical aging in plastics and other glassy materials', *Polymer Engineering and Science*, 17(3), pp. 165–173. doi: https://doi.org/10.1002/pen.760170305.

Sun, M.-K., Shieh, J., Lo, C.-W., *et al.* (2015) 'Reusable tissue-mimicking hydrogel phantoms for focused ultrasound ablation', *Ultrasonics Sonochemistry*, 23, pp. 399–405. doi: https://doi.org/10.1016/j.ultsonch.2014.10.008.

Sun, Z., Li, F. and Li, H. (2016) 'A numerical study of non-collinear wave mixing and generated resonant components', *Ultrasonics*, 71, pp. 245–255. doi: https://doi.org/10.1016/j.ultras.2016.06.019.

Swain, I. (2005) 'Pressure ulcer research: current and future perspectives', in Bader, D. L. et al. (eds). Berlin: Springer Berlin Heidelberg, pp. 51–71. doi: 10.1007/3-540-28804-X_5.

Swain, I. D. and Bader, D. L. (2002) 'The measurement of interface pressure and its role in soft tissue breakdown', *Journal of Tissue Viability*, 12(4), pp. 132–146. doi: http://dx.doi.org/10.1016/S0965-206X(02)80022-5.

Swisher, S. L., Lin, M. C., Liao, A., *et al.* (2015) 'Impedance sensing device enables early detection of pressure ulcers in vivo.', *Nature Communications*. Nature Publishing Group, 6, p. 6575. doi: 10.1038/ncomms7575.

Taylor, H. L. and Rollins, F. R. (1964) 'Ultrasonic study of three-phonon interaction I. Theoy', *A Journal of Experimental and Theoretical Physics*, 136(3A), pp. 591–596.

Thanseer, P., Metya, A. and Sagar, S. (2017) 'Development of a non-collinear nonlinear ultrasonic-based technique for the assessment of crack tip deformation', *Journal of Materials Engineering and Performance*, 26, pp. 1–8. doi: 10.1007/s11665-017-2722-7.

Tsuji, S., Ichioka, S., Sekiya, N. and Nakatsuka, T. (2005) 'Analysis of ischemia-reperfusion injury in a microcirculatory model of pressure ulcers', *Wound Repair and Regeneration*. Blackwell Science Inc, 13(2), pp. 209–215. doi: 10.1111/j.1067-1927.2005.130213.x.

Umemoto, T., Ueno, E., Matsumura, T., *et al.* (2014) 'Ex Vivo and In Vivo assessment of the non-linearity of elasticity properties of breast tissues for quantitative strain elastography', *Ultrasound in Medicine & Biology*, 40(8), pp. 1755–1768. doi: http://dx.doi.org/10.1016/j.ultrasmedbio.2014.02.005.

Urban, M. W., Alizad, A., Aquino, W. and Fatemi, J. F. G. and M. (2011) 'A review of vibro-acoustography and its applications in medicine', *Current Medical Imaging Reviews*, pp. 350–359. doi: http://dx.doi.org/10.2174/157340511798038648.

Washburn, N., Onishi, K. and Wang, J. H.-C. (2018) 'Ultrasound elastography and ultrasound tissue characterisation for tendon evaluation', *Journal of Orthopaedic Translation*, 15, pp. 9–20. doi: https://doi.org/10.1016/j.jot.2018.06.003.

Weaver, R. L. and Pao, Y. (1981) 'Dispersion relations for linear wave propagation in homogeneous and inhomogeneous media', *Journal of Mathematical Physics*. American Institute of Physics, 22(9), pp. 1909–1918. doi: 10.1063/1.525164.

Wei, M.-T., Latinovic, O., Hough, L. A., Chen, Y.-Q., Ou-Yang, H. D. and Chiou, A. (2014) 'Optical-tweezers-based microrheology of soft materials and living cells', in *Handbook of Photonics for Biomedical Engineering*, pp. 731–753.

Wellman, P., Howe R, H., Dalton, E. and Kern K, A. (1999) *Breast tissue stiffness in*

compression is correlated to histological diagnosis:Technical Report.

Wells, P. N. T. and Liang, H.-D. (2011) 'Medical ultrasound: imaging of soft tissue strain and elasticity', *Journal of the Royal Society Interface*. The Royal Society, 8(64), pp. 1521–1549. doi: 10.1098/rsif.2011.0054.

Witte, C., Kremer, C., Cooper, J. M. and Neale, S. L. (2013) 'Continuous cell lysis in microfluidics through acoustic and optoelectronic tweezers ', in *Proc.SPIE*. Available at: https://doi.org/10.1117/12.2004814.

Worden, K., Farrar, C. R., Haywood, J. and Todd, M. (2008) 'A review of nonlinear dynamics applications to structural health monitoring', *Structural Control and Health Monitoring*, 15(4), pp. 540–567. doi: 10.1002/stc.215.

Wrobel, G. and Pawlak, S. (2007) 'A comparison study of the pulse-echo and through-transmission ultrasonics in glass/epoxy composites', *Journal of Achievements in Materials and Manufacturing Engineering*, 22(2), pp. 51–54.

Yamakoshi, Y. and Noguchi, Y. (1998) 'Micro particle trapping by opposite phases ultrasonic travelling waves', *Ultrasonics*, 36(8), pp. 873–878. doi: https://doi.org/10.1016/S0041-624X(98)00013-4.

Yamashita, Y. and Kubota, M. (1995) 'Ultrasonic imaging of elasticity of soft tissue based on measurement of internal displacement and strain', in *Ultrasonics Symposium, 1995. Proceedings., 1995 IEEE*, pp. 1207–1211 vol.2. doi: 10.1109/ULTSYM.1995.495777.

Yamashita, Y. and Kubota, M. (1996) 'Tissue elasticity reconstruction based on ultrasonic strain measurements', in *Ultrasonics Symposium, 1996. Proceedings., 1996 IEEE*, pp. 1113–1116 vol.2. doi: 10.1109/ULTSYM.1996.584186.

Ye, Z. (1997) 'Acoustic dispersion and attenuation in many spherical scatterer systems and the Kramers–Kronig relations', *The Journal of the Acoustical Society of America*. Acoustical Society of America, 101(6), pp. 3299–3305. doi: 10.1121/1.418311.

Zaitsev, V., Nazarov, V., Gusev, V. and Castagnede, B. (2006) 'Novel nonlinear-modulation acoustic technique for crack detection', *NDT & E International*, 39(3), pp. 184–194. doi: https://doi.org/10.1016/j.ndteint.2005.07.007.

Zell, K., Sperl, J. I., Vogel, M. W., Niessner, R. and Haisch, C. (2007) 'Acoustical properties of selected tissue phantom materials for ultrasound imaging.', *Physics in Medicine and Biology*, 52(20), pp. N475-84. doi: 10.1088/0031-9155/52/20/N02.

Zemljič, L. F., Bračič, M., Ristić, T., Šauperl, O., Strnad, S. and Peršin, Z. (2019) 'Functionalization of polymer materials for medical applications using chitosan nanolayers', in Vasile, C. (ed.) *Micro and Nano Technologies*. Elsevier Inc, pp. 333–358. doi: https://doi.org/10.1016/B978-0-12-813932-5.00009-1.

Zhang, X., Osborn, T. and Kalra, S. (2016) 'A noninvasive ultrasound elastography technique for measuring surface waves on the lung', *Ultrasonics*, 71, pp. 183–188. doi:

http://dx.doi.org/10.1016/j.ultras.2016.06.012.

Zheng, Y., Maev, R. G. and Solodov, I. Y. (2000) 'Review / Sythèse nonlinear acoustic applications for material characterization: A review', *Canadian Journal of Physics*. NRC Research Press, 77(12), pp. 927–967. doi: 10.1139/p99-059.